MODELING AND OPTIMIZATION OF PECVD PROCESSES AND EQUIPMENT USED FOR MANUFACTURING THIN FILM PHOTOVOLTAIC DEVICES

A THESIS SUBMITTED TO
THE GRADUATE SCHOOL OF NATURAL AND APPLIED SCIENCES
OF
MIDDLE EAST TECHNICAL UNIVERSITY

BY

ENGİN ÖZKOL

IN PARTIAL FULFILLMENT OF THE REQUIREMENTS
FOR
THE DEGREE OF DOCTOR OF PHILOSOPHY
IN
CHEMICAL ENGINEERING

FEBRUARY 2015

Approval of the Thesis:

MODELING AND OPTIMIZATION OF PECVD PROCESSES AND EQUIPMENT USED FOR MANUFACTURING THIN FILM PHOTOVOLTAIC DEVICES

submitted by **ENGİN ÖZKOL** in partial fulfillment of the requirements for the degree of **Doctor of Philosophy in Chemical Engineering Department, Middle East Technical University** by,

Prof. Dr. Gülbin Dural Ünver
Dean, Graduate School of **Natural and Applied Sciences**

Prof. Dr. Halil Kalıpçılar
Head of Department, **Chemical Engineering**

Assoc. Prof. Dr. Serkan Kıncal
Supervisor, **Chemical Engineering Dept., METU**

Examining Committee Members:

Prof. Dr. İnci Eroğlu
Chemical Engineering Dept., METU

Assoc. Prof. Dr. Serkan Kıncal
Chemical Engineering Dept., METU

Prof. Dr. Raşit Turan
Physics Dept., METU

Assist. Prof. Dr. Erhan Bat
Chemical Engineering Dept., METU

Assist. Prof. Dr. Yılser Devrim
Energy Systems Engineering Dept., Atılım University

Date: *06.02.2015*

I hereby declare that all information in this document has been obtained and presented in accordance with academic rules and ethical conduct. I also declare that, as required by these rules and conduct, I have fully cited and referenced all material and results that are not original to this work.

Name, Lastname: Engin ÖZKOL

Signature :

ABSTRACT

MODELING AND OPTIMIZATION OF PECVD PROCESSES AND EQUIPMENT USED FOR MANUFACTURING THIN FILM PHOTOVOLTAIC DEVICES

Özkol, Engin
Ph.D., Department of Chemical Engineering
Supervisor : Assoc. Prof. Dr. Serkan Kıncal

February 2015, 185 pages

Plasma enhanced chemical vapor deposition (PECVD) is a common technique used in thin film based device fabrication. Operation conditions of a PECVD reactor need to be optimized in terms of deposition conditions as well as plasma cleaning procedures to deliver desired deposited material qualities. In addition, interactions with external support systems such as gas lines and cabinet, compressors and utility production units need to be understood and characterized. Modeling, whether based on fundamental principles or experimental data, is an essential tool in this optimization process, reducing the time required for experimentation.

In this work, a first principles based thermal model of the system is constructed, guiding the design of an improved PECVD chamber delivering better substrate temperature levels and uniformity. On the other hand, material optimization work is supported by the identification of empirical models based on designed experiments, since fundamental models for these interactions are too complicated to be modeled accurately. Individual thin film layers, involved in thin film photovoltaic devices, were optimized in terms of crystallinity, thickness, deposition rate as well as critical optical and electrical properties. The growth of hydrogenated silicon thin films in amorphous (a-Si:H), nano-crystalline, and micro-crystalline regions with intrinsic, n- and p- doping types were characterized and optimized. Amorphous silicon nitride (SiN_x) thin films with tunable silicon and nitrogen concentration, silver thin films with controlled thickness profile down to nm scale, aluminum doped zinc oxide (AZO) thin films with repeatable uniform conductivity were realized successfully. After completing the optimization of these individual layers, several thin film silicon based photovoltaic devices were fabricated. The different performances that are reported in this work include a p-i-n structured homojunction a-Si:H device, a heterojunction device and a heterojunction with intrinsic thin layer (HIT) structured device. The efficiency values of 2.9 % (initial) for a-Si:H p-i-n structure, 15.9 % for heterojunction solar device and 12.5 % for one sided HIT device were recorded.

Keywords: thin film silicon solar cells, p-i-n a-Si:H, HIT, PECVD, temperature distribution modeling

ÖZ

İNCE FİLM FOTOVOLTAİK AYGIT ÜRETİMİNDE KULLANILAN PLAZMA DESTEKLİ KİMYASAL BUHAR BİRİKTİRME (PECVD) SÜREÇLERİ VE EKİPMANININ MODELLEME VE OPTİMİZASYONU

Özkol, Engin
Ph.D., Kimya Mühendisliği Bölümü
Tez Yöneticisi : Doç. Dr. Serkan Kıncal

Şubat 2015, 185 sayfa

Plazma destekli kimyasal buhar biriktirme (PECVD), ince film tabanlı aygıt üretiminde yaygın olarak kullanılan tekniklerden biridir. Bir PECVD reaktörünün çalışma koşulları, film biriktirme koşullarına olduğu kadar plazma temizlik prosedürlerine ve üretilen malzeme kalitesine göre de optimize edilmelidir. Bunun yanısıra, gaz hatları ve odası, kompresörler ve diğer yardımcı üniteler gibi harici destek sistemlerinin PECVD ile etkileşimleri anlaşılmalı ve karakterize edilmelidir. Temel ilkelere ya da deneysel verilere dayalı modelleme, bu optimizasyon sürecinde zaman kazandırması açısından çok önemli bir araçtır.

Bu çalışmada, öncelikle kullanılmakta olan sistemin temel ilkelere dayalı ısısal modeli oluşturulmuş, ve bu model üzerinden daha iyi taban sıcaklık seviyeleri ve düzgün sıcaklık dağılımları hesaplanarak iyileştirilmiş bir PECVD tasarımı önerilmiştir. Diğer yandan, malzeme optimizasyonları için, temel ilkelere dayalı modelleme kesin bir şekilde anlaşılması zor olduğundan, deneysel tasarımlara dayalı ampirik modeller kullanılmıştır. İnce film fotovoltaik aygıtlarda kullanılan katmanlar, birbirinden ayrı olarak, kristanilite, kalınlık, büyütme hızı açısından olduğu kadar kritik optik ve elektriksel özellikler açısından da optimize edilmiştir. Hidrojenlendirilmiş katkısız, n- ve p- katkılı ince film silisyum katmanları amorf (a-Si:H), nano-kristal, ve mikro-kristal fazlarında karakterize ve optimize edilmiştir. Ayarlanabilir silisyum ve azot konsantrasyonlarında amorf silisyum nitrit (SiN_x) ince filmler; kalınlık profili nanometre ölçeğinde kontrol edilebilen gümüş ince filmler; tekrarlanabilir iletkenlik standartlarında aluminyum katkılı çinko oksit (AZO) ince filmler başarıyla üretilmiştir. Katmanların bireysel optimizasyonları tamamlandıktan sonra silisyum bazlı birçok ince film fotovoltaik aygıt üretilmiştir. Bu çalışmada sunulan değişik performanslar arasında p-i-n yapılı eş-eklemli a-Si:H, hetero-eklemli ve katkısız ince katmanlı hetero-eklemli (HIT) aygıtlar bulunmaktadır. a-Si:H p-i-n yapısında %2.9 (başlangıç), hetero-eklemli aygıtta %15.9, ve tek taraflı HIT yapısında %12.5 verim kaydedilmiştir.

Anahtar Kelimeler: ince film silisyum güneş gözeleri, p-i-n a-Si:H, HIT, PECVD, sıcaklık dağılımı modellemesi

To my family

ACKNOWLEDGMENTS

First of all I would like to thank my supervisor Dr. Serkan Kıncal for his encouragement, inspiration and guidance during my study. I am also honored to be his first PhD graduate.

I express my gratitude to my 'boss' Prof. Dr. Raşit Turan for providing me the opportunity to be a member of GÜNAM family. I am very grateful to him for his informative discussions and excellent guidance during my study.

Prof. Dr. Mehmet Parlak and Dr. Zaki M. Saleh are appreciated for their creative ideas and sharing their theoretical and experimental knowledge with me. Prof. Dr İnci Eroğlu is also appreciated for her creative criticism during my PhD study.

I would like to next thank to my 'Thin Film Group' members. Zeynep Demircioğlu was always there to restore my joy in life when I was depressed. She was always very kind and patient on me like a sister. I also would like to thank her for the help in formatting my thesis, which may be a burden for me without her help. Hisham Nasser became like a brother to me, and also shared his creative ideas both in academic and daily life. Dr. Tahir Çolakoğlu although joined the group lately, but he was one of my oldest basement friends. I am grateful to him for his presence since 2005. Lastly our ex-members Gizem Nogay and Burcu Barutçu, you are not and will not be forgotten.

I would like to thank my roommate Fırat Es not only for enduring me for years, but also his creative ideas, friendship and helping me with CATIA drawings in the thesis.

GÜNAM would be a monotonous research center without my dear friends and colleagues; Olgu Demircioğlu, Hande Çiftpınar, Dr. Mustafa Kulakçı (probably the most acknowledged man on the world), Mehmet Karaman, Yasin Ergunt, Dr. Serim İlday, Serra Altınoluk, Ergi Dönerçark, Salar Habibpur Sedani, Mete Günöven, Gülsen Baytemir, Makbule Terlemezoğlu, Özden Başar Balbaşı, Çiğdem Doğru, Merve Pınar Kabukcuoğlu, Burcu Altuntaş, Yusuf Kasap, Mona Zolfaghari Borra (it is not possible to forget her 'eyvaaay'), Dr. Mücahit Yılmaz, İsmail Kabaçelik, Deniz Cihan Gündüz, Hasan Hüseyin Güllü and his kind wife Seda Kayra Güllü, Arezoo Hosseini, Özge Bayraklı, Dr. Aydın Tankut, Mustafa Ünal, Dr. Emre Coşkun and Kurtuluş Abak. I am grateful to have them by my side during my study.

I am grateful to GÜNAM technicians; Yücel Eke, Nevzat Görmez, Tayfun Yıldız, Dursun Erdoğan for technical support and also administrative staff of GÜNAM; Harun Tanık, Tuncay Güngör and Buket Gökbakan.

I would like to thank Vaksis personnel for land me their hand whenever needed; Dr. Baybars Oral, Dr. Müzeyyen Oral, Mehmet Emre Kabadayı (whom I worked with for a year or more on GÜNER), Durmuş Sakcı, Emrah Aytaş, Murat Çalık, Mustafa Çelik, Gökhan Doğan, Özlem Eker and ex-technician Sadık Yenilmez.

It is not possible for me to forget my dear friends Turhan Atakan Gülyurdu, Özlem Dede Öztürk, Dr. Erinç Bahçegül, Aytuğ Anlayışlı, Dr. Umut Parmaksız, Emre Yılmaz, Can Bayraktar and Mustafa Aslan, who made my life fruitful and brilliant.

Last but not the least I would like to thank my family for their unconditional love, endless support and encouragement during my 'student' life. Special thanks reward goes to my dearest niece Lara Deniz who brought joy to our life since April 2014.

TABLE OF CONTENTS

CHAPTERS

APPENDICES

LIST OF TABLES

TABLES

LIST OF FIGURES

FIGURES

NOMENCLATURE

FF	Fill factor
I	Current
I_0	Saturation current
I_{SC}	Short circuit current
J	Current density
J_0	Saturation current density
J_{dark}	Dark current density
Jm	Maximum current density
J_{SC}	Short circuit current density
k_B	Boltzmann's constant
P	Power
P_m	Maximum power
P_R	Deposition pressure
P_S	The coming incident light power density
P_W	Plasma power
R	H_2/SiH_4 feed gas ratio
R_s	Series resistance
R_{sh}	Shunt (or parallel) resistance
q	Electrical charge
T	Temperature
V	Voltage
V_m	Maximum voltage
V_{OC}	Open circuit voltage
η	Efficiency

CHAPTER 1

INTRODUCTION

1.1 Photovoltaics (PV) basics

Photovoltaic energy conversion is a process which generates electrical energy from light. The visible photon energy is sufficient to excite the electrons to higher energy levels, where they are freer to move. In a photovoltaic device, there is some built-in asymmetry that pulls away the electrons before they can relax and feeds them to an external circuit, as illustrated in Figure 1.1. The extra energy of the exited electrons generates a potential difference. This potential drives the electrons through a load to do electrical work [1].

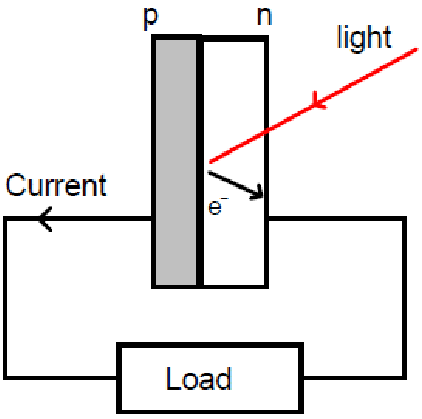

Fig. 1.1 The Photovoltaic Effect: photons in, electrons out

The conversion of light into electrical energy simply involves two steps; (1) generation of free electron and holes by absorbing photon energy, (2) separation of these two in order to have electricity[2].

When a semi-conductor is illuminated, free electrons are created if incoming photon energy is higher or equal to the band gap of the material. Band gap energy is the difference in energy levels between the lowest (conduction band) and highest (valance band). Thus, band gap is one of the most important semiconductor material property for PV applications.

As the second step, created electron hole pairs should be separated. An electric field is a must for this separation. In a solar cell, typical p-n or p-i-n type diodes creates this electric field. p-type corresponds to lower electron density (with respect to holes), n-type to the higher electron density. Intrinsic material corresponds to undoped material. The generation of this internal electric field is governed by built-in voltage, V_{bi}, which has a value of roughly 1 V for all forms of silicon solar cells [2]. In Figure 1.2, both p-n and p-i-n type diodes are shown as energy band diagrams.

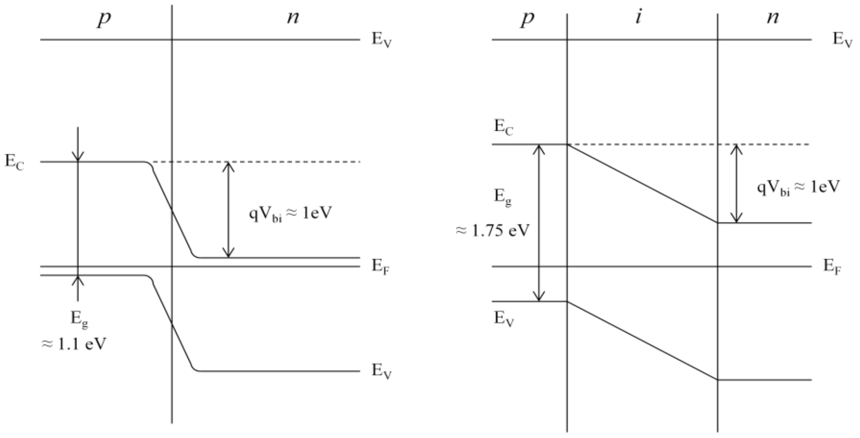

(a) (b)

Fig. 1.2 Band diagram for (a) c-Si pn-type diode, (b) a-Si pin-type diode. E_V is local vacuum energy level

1.2 Basic Definitions

The solar cell is the basic unit of the solar photovoltaics that conducts like a diode in the dark and generates photocurrent under illumination. The surface is treated to reflect as low visible light as possible. To make electrical contact, metal is imprinted on the surface.

The solar cell can be considered as an electric circuit. The voltage developed when the terminals are isolated is called open circuit voltage, V_{OC} and formulated as;

$$V_{OC} = \frac{kT}{q} ln\left(\frac{J_{SC}}{J_0} + 1\right) \qquad \text{Eqn (1.1)}$$

The current drawn when the terminals are connected together is the short circuit current, I_{SC}. Since the current is roughly proportional to the illuminated area, short circuit current density, J_{SC} is the useful quantity.

The reverse current generated by the developed potential difference between the terminals is called the dark current, J_{dark}, which is given as;

$$J_{dark}(V) = J_0(e^{\frac{qV}{k_BT}} - 1) \qquad \text{Eqn (1.2)}$$

Where;

k = 1.3807 x 10^{-23} [J/K] is the Boltzmann's constant, q = 1.6022 x 10^{-19} [C] is the electrical charge, T is the absolute temperature, J_0 is the reverse saturation current density of the diode.

Under illumination, photo-generated current density J_{ph} is formed opposite to the J_{dark}. So illuminated current density for an ideal diode is given as;

$$J_{illum} = J_{ph} - J_{dark} = J_{ph} - J_0(e^{\frac{qV}{k_BT}} - 1) \qquad \text{Eqn (1.3)}$$

However, real solar cells cannot act as ideal diodes. In a cell power is dissipated through the resistance of the contacts and leakage currents around the sides or pinholes in the layers. The series resistance (R_s) arises from contacts and material itself. The shunt resistance (R_{sh}) arises from the leakage currents around the edges of the cell, between contacts of different polarity and through the pinholes in the layers. Including these parasitic resistances, the diode equation becomes;

$$J_{illum} = J_{ph} - J_0\left(e^{\frac{q(V+JAR_s)}{k_BT}} - 1\right) - \frac{V + JAR_s}{AR_{sh}} \qquad \text{Eqn (1.4)}$$

where A is the illuminated area of the cell.

1.3 J-V Curve

The operating regime of the solar cell is 0 – V_{OC} as seen in Figure 1.3. The cell power density is given by;

$$P = JV \qquad \text{Eqn (1.5)}$$

P reaches a maximum at a V_m and J_m, which is known as the maximum power point. The fill factor describes the squareness of the J-V curve and formulated as;

$$FF = \frac{J_mV_m}{J_{SC}V_{OC}} \qquad \text{Eqn (1.6)}$$

The efficiency, η, of the cell is the power density delivered at the operating conditions divided by the coming incident light power density, P_s.

$$\eta = \frac{J_mV_m}{P_s} \qquad \text{Eqn (1.7)}$$

It can be expressed in terms of FF, V_{OC} and J_{SC} as;

$$\eta = \frac{J_{SC}V_{OC}FF}{P_s} \qquad \text{Eqn (1.8)}$$

These four quantities (FF, V_{OC}, J_{SC}, η) are the key performance characteristics of the cell.

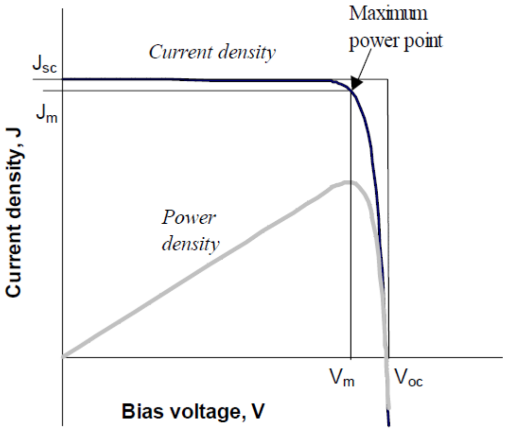

Fig. 1.3 J-V curve

1.4 Thin Film Photovoltaic Materials

Desired thin film materials should be low cost, non-toxic, robust, stable and have high absorption coefficients. Higher absorption reduces the cell thickness and so relaxes the requirement for long minority carrier diffusion lengths, allowing less pure polycrystalline or amorphous materials to be used [1].

1.5 Amorphous Silicon (a-Si) and a-Si Based Solar Cells

a-Si has advantages among the photovoltaic materials such as low cost, low deposition temperatures (<300ºC) and it can be deposited on various materials including glass, metal and plastics. When compared with crystal silicon (c-Si), a-Si is about 100 times efficient in absorbing light, but doping and charge transport is more difficult. Another important property of a-Si based solar panels is that the efficiency increases with the temperature. Therefore it is used as roofing material in desert and tropical climates [3].

The light induced degradation (LID), also known as Staebler-Wronski effect (SWE) is the major disadvantage of a-Si thin films in photovoltaic point of view. In a typical a-Si solar cell the efficiency is reduced up to 30% in the first six months (or after some 1000 hours of light exposure [2]) due to LID. The defect density in a-Si:H structure increases with light exposure to cause an increase in the recombination current and the internal electric field is strongly reduced. Thus efficiency of the cell is lowered. It is believed that light energy breaks Si-H bonds to increase the dangling bond density. Annealing at a few hundred degrees Centigrade allows the structure to relax, and resaturation of the dangling bonds. For this reason a-Si solar cells may perform better in high temperature climates [1].

There are two methods of reducing LID; (1) deposition at higher temperatures and (2) hydrogen dilution [2].

a-Si solar cell is based on p-i-n junction. Since the diffusion length is very low in doped a-Si, an undoped, intrinsic i-region must be deposited. a-Si is usually deposited by plasma decomposition of silane on glass substrates. While considering the stacking, the glass substrate is covered with transparent conductive oxide (TCO). Then a-Si, p-i-n junction is deposited. On top of the stack, back contact metal is deposited [1]. The stack is illustrated in Figure 1.4.

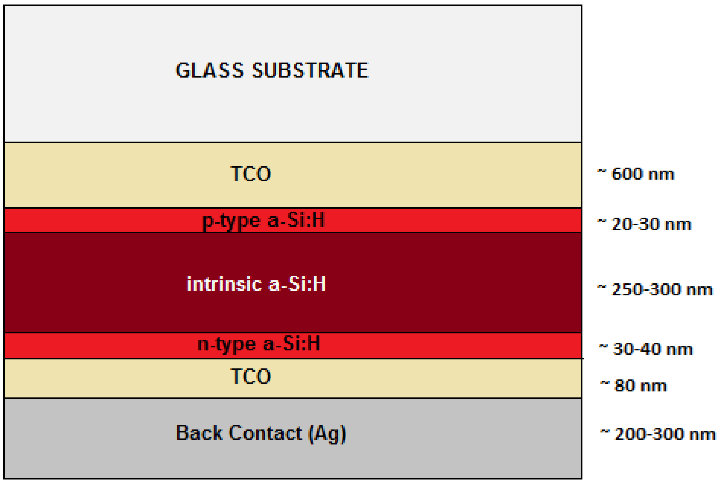

Fig. 1.4 Structure of p-i-n type solar cell

a-Si layers are also have an important role in heterojunction based solar devices, such as heterojunction with intrinsic thin layer (HIT) solar cells. HIT structure is illustrated in Figure 1.5. HIT solar cells do have very thin intrinsic a-Si layers on both sides of the silicon wafer for the passivation of the dangling bonds at the surfaces. This layer should increase V_{OC} (therefore efficiency) by reducing the number of the recombination centers. The opposite (to the wafer) doped a-Si layer forms the heterojunction. The same doped layer increases the electric field to increase the number of collected electrons. AZO layers act as anti reflection coating (ARC) and also increases the lateral conduction [4].

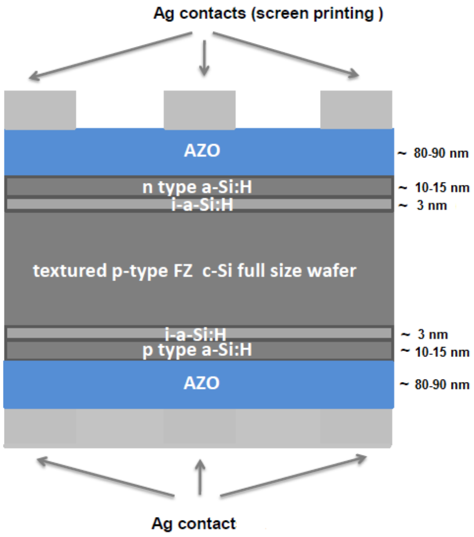

Fig. 1.5 Structure of HIT solar cell

1.6 From Cell to Module

A solar cell generates 0.5-1 V voltage and tens of mA/cm^2 current when charged by the sun. The voltage is so low for most of the applications. Therefore, these cells should be connected in series. In p-i-n structure, layers are deposited on large areas and the connection is done by laser scribing.

After depositing the TCO layer, P1 scribing is done for the electrically isolation of solar cells in the panel. 1064 nm wavelength (IR) is used for this scribing. Then absorber layer is deposited. P2 scribing is the scribing of the absorber layer, namely p-i-n structure, without damaging the TCO layer. 532 nm wavelength (green) is used for this scribing. Then back contact layer is deposited. To form series connection between the cells of the solar panel, lastly P3 scribing is utilized. After this last laser scribing, to avoid short contacts through the lateral sides edge isolation is done by laser. 532 nm wavelength (green) is used for this scribing. All of these steps are demonstrated in Figure 1.6.

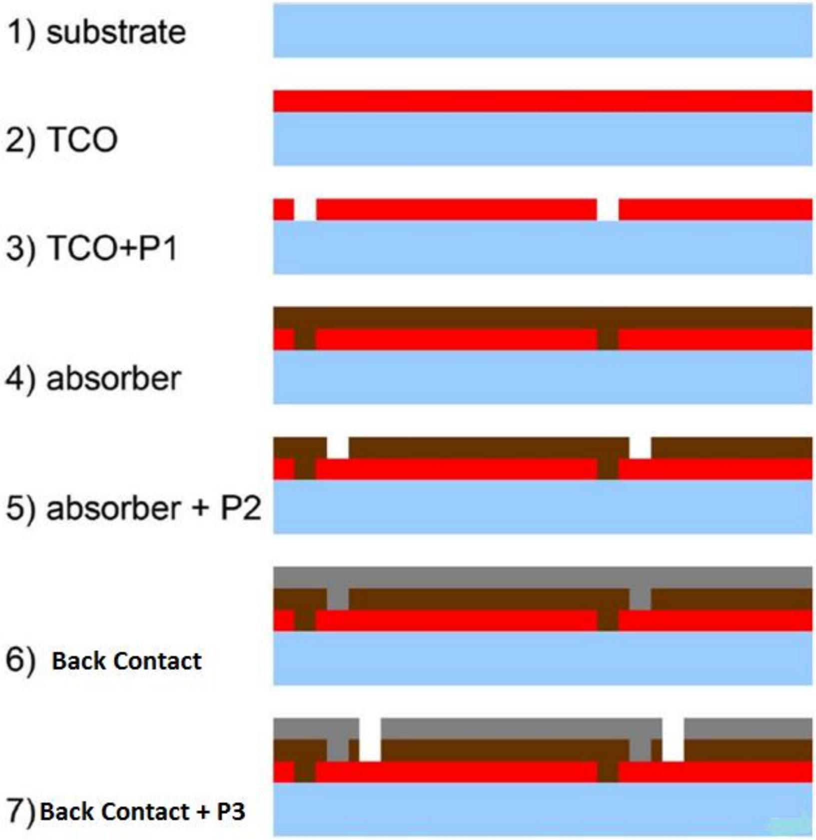

Fig. 1.6 Scribing Sequence

1.7 Deposition Reaction Mechanisms of a-Si from SiH_4

PECVD is an extremely complex process involving a multitude of interactions between the plasma, chemical reactions of the gases and their reaction products, as well as interactions with the surrounding surfaces, ultimately including the substrate to be coated [2].

The plasma contains electrons, ions, neutral atoms, free radicals and metastable species. Most of these species are chemically active. Both concentration gradients and electric field support mass transfer to the substrate surface. Thereby interactions of various species with the substrate is initiated. These processes are shown in below Figure 1.7.

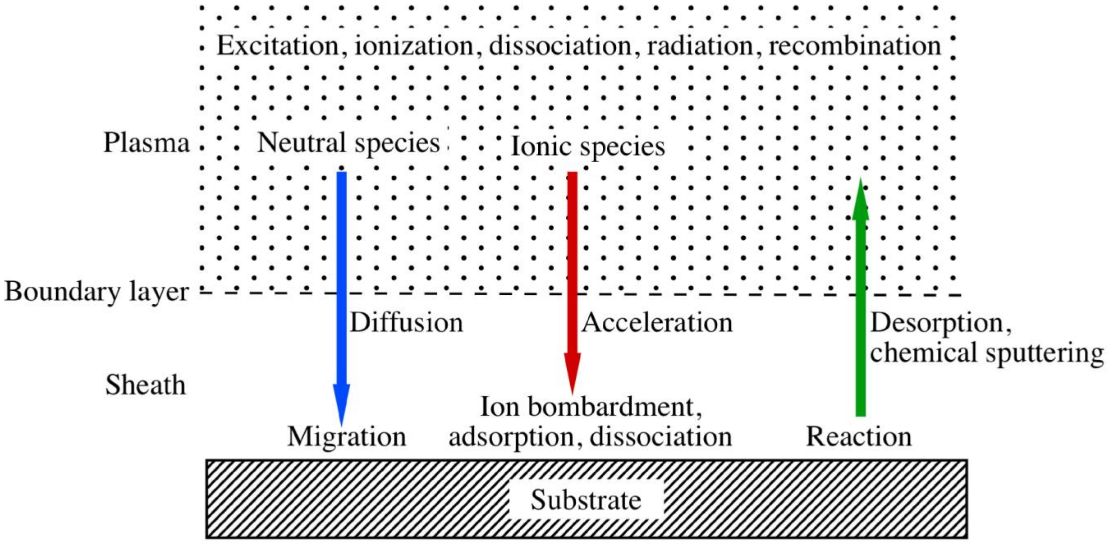

Fig. 1.7 Interactions and reactions during PECVD process

The dissociation, dissociative-ionization processes of silane is given in the following tables 1.1 and 1.2.

Table 1.1 Dissociation processes of SiH_4 [5]

Dissociation process	Dissociation energy (eV)
$SiH_4 + e \rightarrow SiH_3 + H + e$	3.9-4.1
$SiH_2 + H_2 + e$	2.1-2.4
$SiH_2 + 2H + e$	6.7
$SiH + H_2 + H + e$	5.5-5.9
$Si + 2H_2 + e$	4.2-4.4
$Si + H_2 + 2H + e$	8.7
$Si + 4H + e$	13.2

Table 1.2 Dissociative-ionization processes of SiH_4 [5]

Dissociative-ionization process	Appearance potential (eV)
$SiH_4 + e \rightarrow SiH_3^+ + H + 2e$	11.8-14.2
$SiH_2^+ + H_2 + 2e$	11.8-14.5
$SiH_2^+ + 2H + 2e$	16.2-18.6
$SiH^+ + H_2 + H + 2e$	11.5-16.1
$SiH^+ + 3H + 2e$	20.0-20.4
$Si^+ + 2H_2 + 2e$	11.7-14.8
$Si^+ + H_2 + 2H + 2e$	16.4-20.2
$Si^+ + 4H + 2e$	20.8-22.9

Table 1.3 Reaction rate constants for dissociative-ionization processes of SiH_4 ($x10^{11}$ cm^3/s) [5]

T_e (eV)*	SiH_3^+	SiH_2^+	SiH^+	Si^+
3	5.98	8.58	0.17	0.05
5	94.8	132.7	7.14	2.8
7	300	414.6	33.6	16.7

*$8.62x10^{-5}$ eV corresponds to 1K

In Table 1.3, it is seen that the reaction rate constants of SiH_3^+ and SiH_2^+ are so higher than the other radicals. Therefore, these radicals are more abundant and they will be the most accelerated molecules to the substrate.

The following reactions is considered to be particularly important in the plasma [5].

$$H + SiH_4 \leftrightarrow SiH_3 + H_2$$

$$2SiH_3 \leftrightarrow SiH_2 + SiH_4$$

$$SiH_2^+ + SiH_4 \leftrightarrow SiH_3^+ + SiH_3$$

CHAPTER 2

LITERATURE SURVEY

2.1 History of Solar Cells

Edmund Bequerel was the first scientist who reported photovoltaic effect in 1839. He observed that the illumination of silver coated platinum electrode immersed in electrolyte generates an electric current. In the late 1800's, first devices were constructed from selenium. In 1876, William Adams and Richard Day observed photocurrent in a selenium sample placed between heated platinum contacts. In 1894, Charles Fritts produced the first large area solar cell by pressing selenium between gold and another metal. After selenium, copper-copper oxide, lead sulphide, and thallium sulphide were investigated. During 1930's, Walter Schottky, Neville Mott and others developed the theory of metal-semiconductor barrier (also called Schottky barrier) layers [1].

However, the current and thus the power obtained from selenium like materials was too low that is not useable for devices. Indeed what excited the researchers was the photoconductivity. In the 1950's, silicon electronics was developed and p-n junction manufactory was discovered. This material has better photovoltaic behavior than Schottky barriers. In 1954, the first silicon solar cell of 6% efficiency was reported by Chapin, Fuller and Pearson. At the same year, a cadmium sulphide p-n junction solar cell with 6% efficiency was produced.

In 1970's, the energy crisis in western world led to a growth in producing cheaper and more efficient photovoltaic devices. Polycrystalline silicon, amorphous silicon, other 'thin film' materials and organic solar cells were developed in this period. Also, strategies for tandem and multiple band gap structures were designed [1].

2.2 Development of Thin Film Solar Cells

In 1976, Carlson and Wronski announced the first pin a-Si:H single junction solar cell deposited on glass substrate with an initial efficiency of 2.4%. [6] However, one year later, in 1977, Staebler and Wronski introduced light induced degradation (also known as SWE) concept [7]. Although, thin film a-Si:H has several advantages over c-Si solar cells such as low cost, high absorption, easy production, several substrate selection and less temperature dependent performance, the SWE is the most important disadvantage in photovoltaic point of view. Due to SWE initial efficiency of a-Si:H solar cells degrade up to 30% in first six months. In order to increase output voltage multi-junction solar cell concept was introduced in 1979 [8]. In 1980, a key step for industrial approach was introduced; monolithic series integration [9]. At the same year integrated type a-Si:H solar cells were commercialized as calculators and watches. In 1980's, research area was to develop a-Si:H based alloys. As a low absorbing layer (window layer), p-type a-SiC:H was introduced [10]. a-SiGe:H became an attractive low band gap material [11]. Surface texturing of glass substrates for optical enhancement was investigated [12]. Single junction a-Si:H modules of 5% efficieny, and laboratory cells of 11 to 12% initial efficiency were achieved in 1980's. In 1990's the main aim was to increase the stabilized efficiency to 10%'s. In order to reach this goal, several companies implemented a-SiGe:H alloy in tandem and triple junction cells. As another approach hydrogenated microcrystalline silicon was studied in this period as a new low absorbing layer in tandem structures and in 1994, a micromorph tandem solar cell of a-Si:H top cell, μc-Si:H bottom cell was introduced [13]. The early demonstrations showed stabilized efficiencies of 11-12% [14, 15].

2.3 Development of HIT Structure

The investigation of heterojunction structures started in mid 1960's [4]. In 1965, Grigorivici reported results on amorphous germanium on crystalline silicon heterojunctions [16]. The same group reported the first amorphous silicon on crystalline silicon (a-Si/c-Si) heterojunction in 1968. They deposited defective a-Si on both p-type and n-type silicon wafers at room temperature and annealed them at 290-500 °C. They concluded a-Si should be p-type for better retrification, so p-type a-Si / n-type c-Si has better photovoltaic properties [17]. Later, in 1972 Jayadevaiah reported the same behaviour by C-V characteristics [18]. In 1974, the first a-Si/c-Si heterojunction has been reported by Fuhs [19]. At the beginning of 1980's, a strong interest in a-Si/c-Si structures has emerged. Tandem structures such as n-type a-Si:H on p-type polycrystalline silicon with nip a-Si:H top cell or a-Si:H/ribbon c-Si as bottom cell with a pin a-Si:H junction on top has been realized. An initial efficiency of 11% has been reported by Nogazi in 1984 [20]. In 1992, Sanyo presented a new heterojunction type called "Heterojunction with Intrinsic Thin layer" or shortly the HIT solar cell [21]. The first publication reported 18.1% efficiency. In 2009, they reached 23% and the last solar efficiency tables stated the record as 25.6% for 143.7 cm^2 area in April, 2014 [22]. They reached 19.4% module efficiency and properties of the modules are tabulated in Table 2.1 and 2.2 [23].

Table 2.1 Latest cell and module efficiencies on market achieved by Panasonic

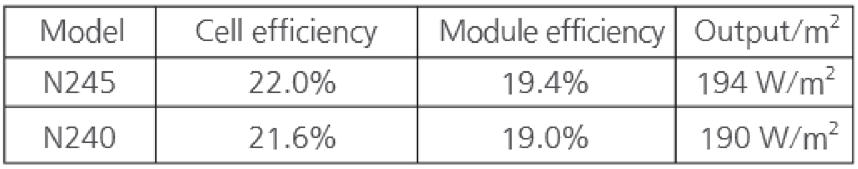

Model	Cell efficiency	Module efficiency	Output/m^2
N245	22.0%	19.4%	194 W/m^2
N240	21.6%	19.0%	190 W/m^2

Table 2.2 Properties of latest HIT modules by Panasonic

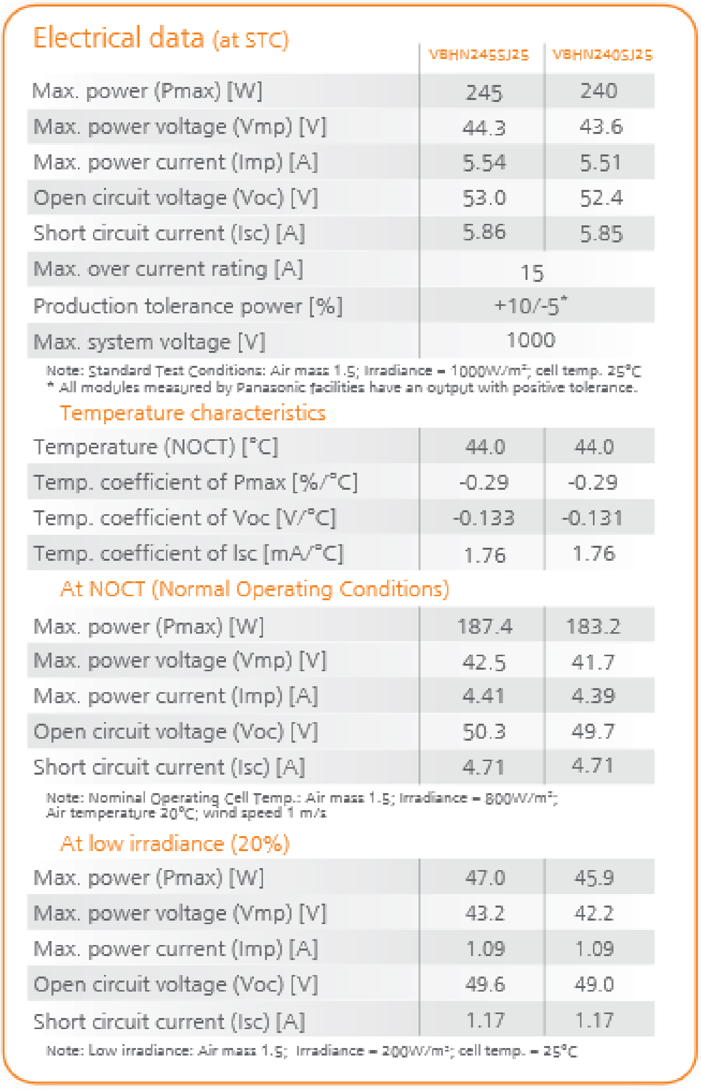

Electrical data (at STC)

	VBHN245SJ25	VBHN240SJ25
Max. power (Pmax) [W]	245	240
Max. power voltage (Vmp) [V]	44.3	43.6
Max. power current (Imp) [A]	5.54	5.51
Open circuit voltage (Voc) [V]	53.0	52.4
Short circuit current (Isc) [A]	5.86	5.85
Max. over current rating [A]	15	
Production tolerance power [%]	+10/-5*	
Max. system voltage [V]	1000	

Note: Standard Test Conditions: Air mass 1.5; Irradiance = 1000W/m²; cell temp. 25°C
* All modules measured by Panasonic facilities have an output with positive tolerance.

Temperature characteristics

	VBHN245SJ25	VBHN240SJ25
Temperature (NOCT) [°C]	44.0	44.0
Temp. coefficient of Pmax [%/°C]	-0.29	-0.29
Temp. coefficient of Voc [V/°C]	-0.133	-0.131
Temp. coefficient of Isc [mA/°C]	1.76	1.76

At NOCT (Normal Operating Conditions)

	VBHN245SJ25	VBHN240SJ25
Max. power (Pmax) [W]	187.4	183.2
Max. power voltage (Vmp) [V]	42.5	41.7
Max. power current (Imp) [A]	4.41	4.39
Open circuit voltage (Voc) [V]	50.3	49.7
Short circuit current (Isc) [A]	4.71	4.71

Note: Nominal Operating Cell Temp.: Air mass 1.5; Irradiance = 800W/m²;
Air temperature 20°C; wind speed 1 m/s

At low irradiance (20%)

	VBHN245SJ25	VBHN240SJ25
Max. power (Pmax) [W]	47.0	45.9
Max. power voltage (Vmp) [V]	43.2	42.2
Max. power current (Imp) [A]	1.09	1.09
Open circuit voltage (Voc) [V]	49.6	49.0
Short circuit current (Isc) [A]	1.17	1.17

Note: Low irradiance: Air mass 1.5; Irradiance = 200W/m²; cell temp. = 25°C

The development of photovoltaic materials has been tracked by National Renewable Energy Laboratory (NREL) since 1970's. The latest NREL efficiency chart [21] can be seen in Figure 2.1.

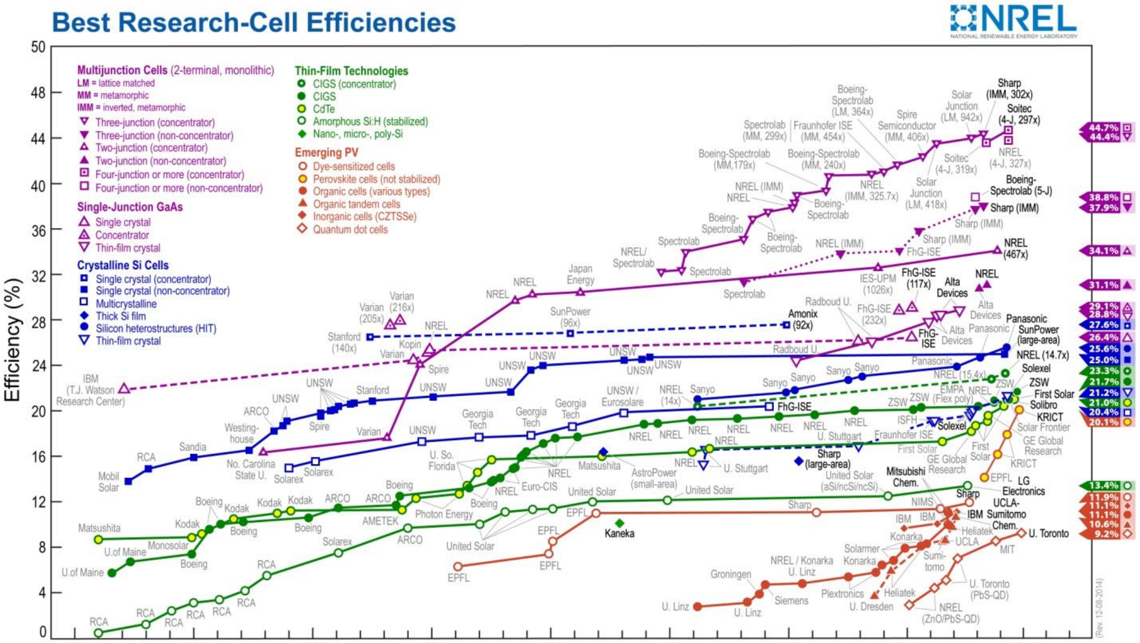

Fig. 2.1 NREL Efficiency Chart

CHAPTER 3

EXPERIMENTAL

3.1 GÜNAM Cleanrooms

A cleanroom is a controlled environment in which the concentration of particles is allowed to specified limits. These contaminants are generated by people, processes, facilities and equipments. They must be continually removed from the air. For this purpose high efficiency particulate air (HEPA) filters are used to eliminate particles from inlet air to the cleanroom and positive pressure is always maintained inside. The rooms are kept clean not only by filters, but also who enters the rooms should wear a laboratory coat, gloves, boots, a bouffant cap and if necessary masks.

A Class 10,000 cleanroom is designed to never allow more than 10,000 particles (0.5 microns or larger) per cubic foot of air. Class 1000 cleanroom are designed to limit particles to 1000. Process equipments are placed in Class 10,000 cleanroom and the chemical cleaning room is Class 1000.

3.2 GÜNER System

GÜNER (Güneş Enerjisi) is a cluster system especially designed for the complete stack deposition of the amorphous silicon (a-Si), nano-crystalline silicon (nc-Si) and micro-crystalline (μc-Si) thin film solar cells or panels produced by VakSis (Vakum Sistemleri) Company. It is located in GÜNAM 10,000 cleanroom. It consists of three capacitively coupled plasma (CCP) chambers, one inductively coupled plasma (ICP) chamber, one sputtering chamber with two different targets, a transfer chamber and a load lock chamber. The system can be seen in Figure 3.1 and schematically shown in Figure 3.2.

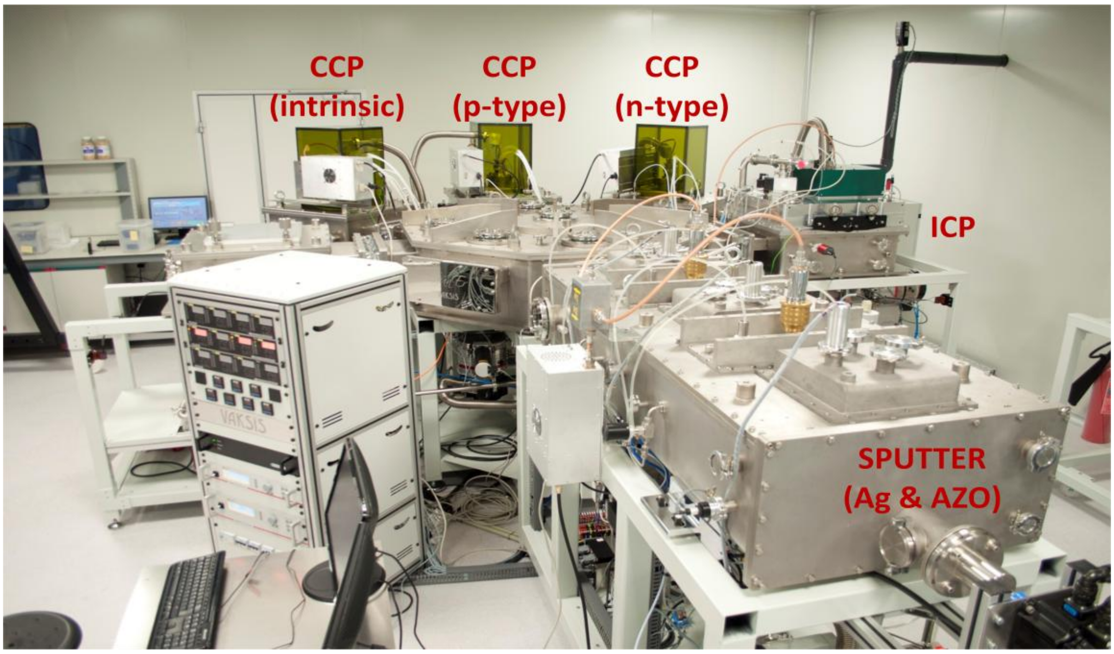

Fig 3.1 GÜNER System

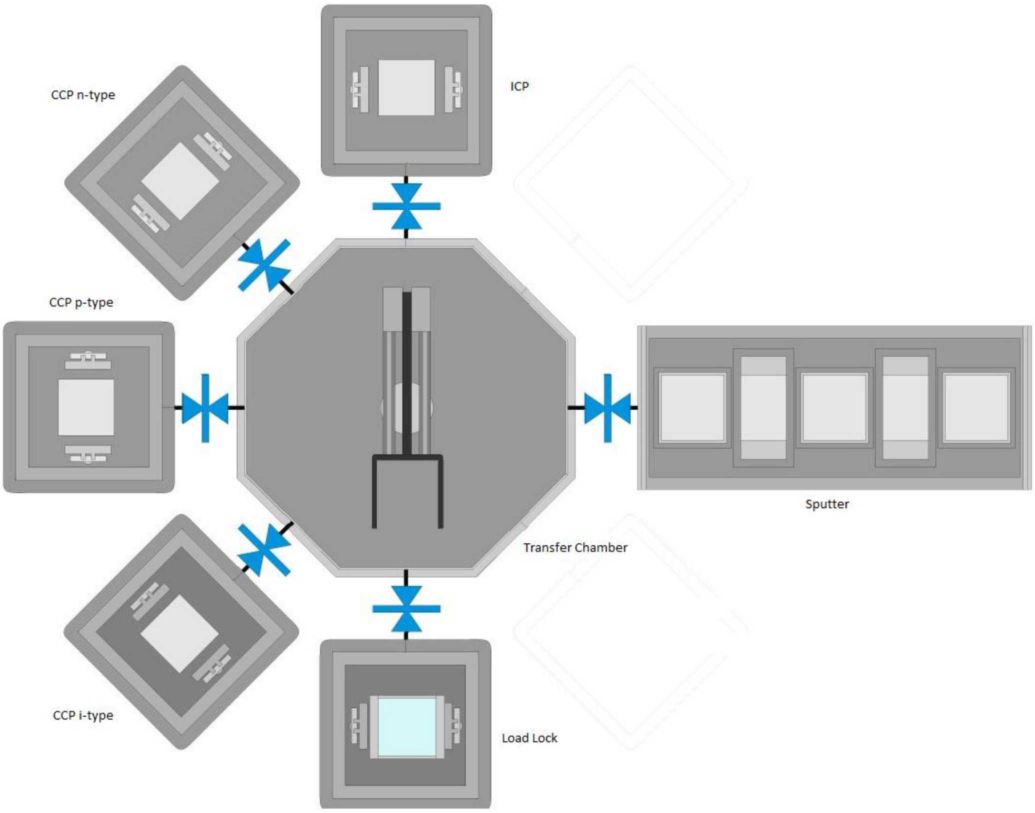

Fig 3.2 Schematic representation of GÜNER System

3.2.1 Load Lock and Transfer Chambers

The 25x25 cm^2 glass substrates are placed in the load lock chamber after a special substrate cleaning. This chamber has only mechanical (rotary vane) pump for vacuum. When the pressure reaches 10^{-3} Torr, the substrate is ready to be taken into transfer chamber. The only chamber where one can ‘touch’ the substrate is the load lock. The other chambers are always kept under vacuum.

Transfer chamber is connected to each chamber from six transfer gate valves (TGV). It has both mechanical and turbo-molecular pumps by which the 10^{-6} Torr vacuum level can be easily attained. A robot arm is placed inside the chamber that can rotate 360 degrees for the movement of the substrate to the desired chamber. The arm also moves forward and backward for the movement of the substrate through TGV’s.

Both the load lock and the transfer chambers are represented in Figure 3.3.

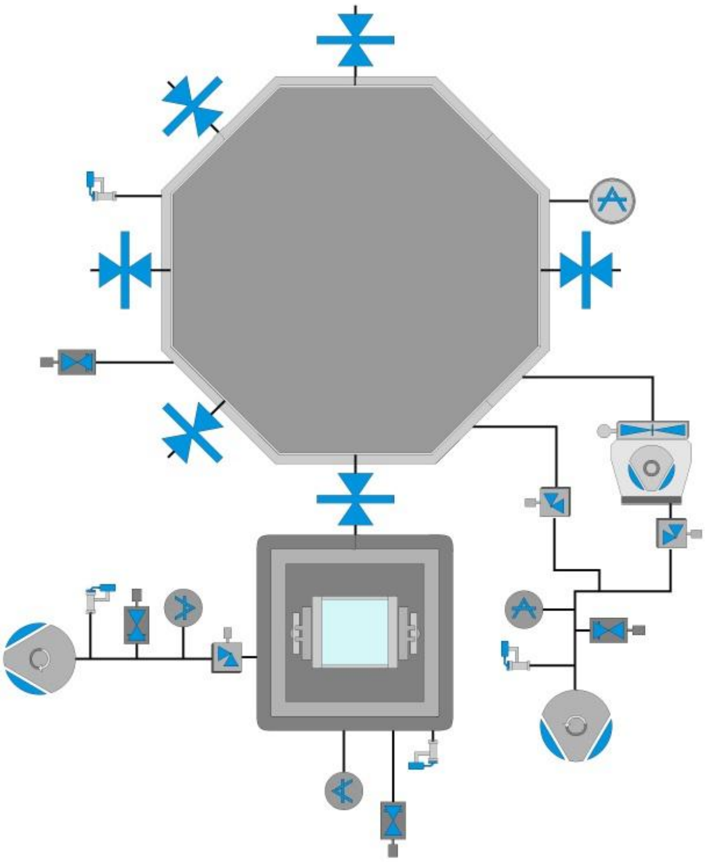

Fig 3.3 Schematic representation of load lock and transfer chambers

3.2.2 CCP Chambers

Capacitively coupled plasma (CCP) is one of the most common types of industrial plasma sources. CCPs have wide applications in the semiconductor processing industry for thin film deposition and etching. It essentially consists of two metal electrodes separated by a small distance, placed in a reactor. The gas pressure in the reactor is usually lower than atmosphere [25].

A typical CCP system is driven by a single radio-frequency (RF) power supply, at 13.56 MHz. One of the two electrodes is connected to the power supply (called cathode), and the grounded one is called anode. The plasma formed in this configuration is called a capacitively coupled plasma.

When an electric field is generated between electrodes, atoms become ions that release electrons. The electrons in the gas are accelerated by the RF field and can ionize the gas directly or indirectly by collisions, producing secondary electrons. When the electric field is strong enough, it can lead to what is known as electron avalanche. After avalanche breakdown, the gas becomes electrically conductive due to abundant free electrons. Often it accompanies light emission from excited atoms or molecules in the gas [25].

In GÜNER system, three CCP chambers are present as seen in Figure 3.4. In each chamber, one of the silicon layers is deposited. The deposited materials to the walls of the chambers can desorb when plasma is formed. Since the doping process is a vital step in solar cell production, each doping process has its own chamber and all gas lines are separated. For instance, only p-type CCP chamber has B_2H_6 inlet, whereas n-type CCP chamber has PH_3 and intrinsic CCP chamber has only SiH_4 entrance. Common process gases (CPG) that are He, H_2, NH_3, CH_4, C_2F_6, NF_3 have inlet to every chamber due to several reasons such as plasma cleaning or diluting the process gases. To break vacuum, dry N_2 gas is used for each chamber.

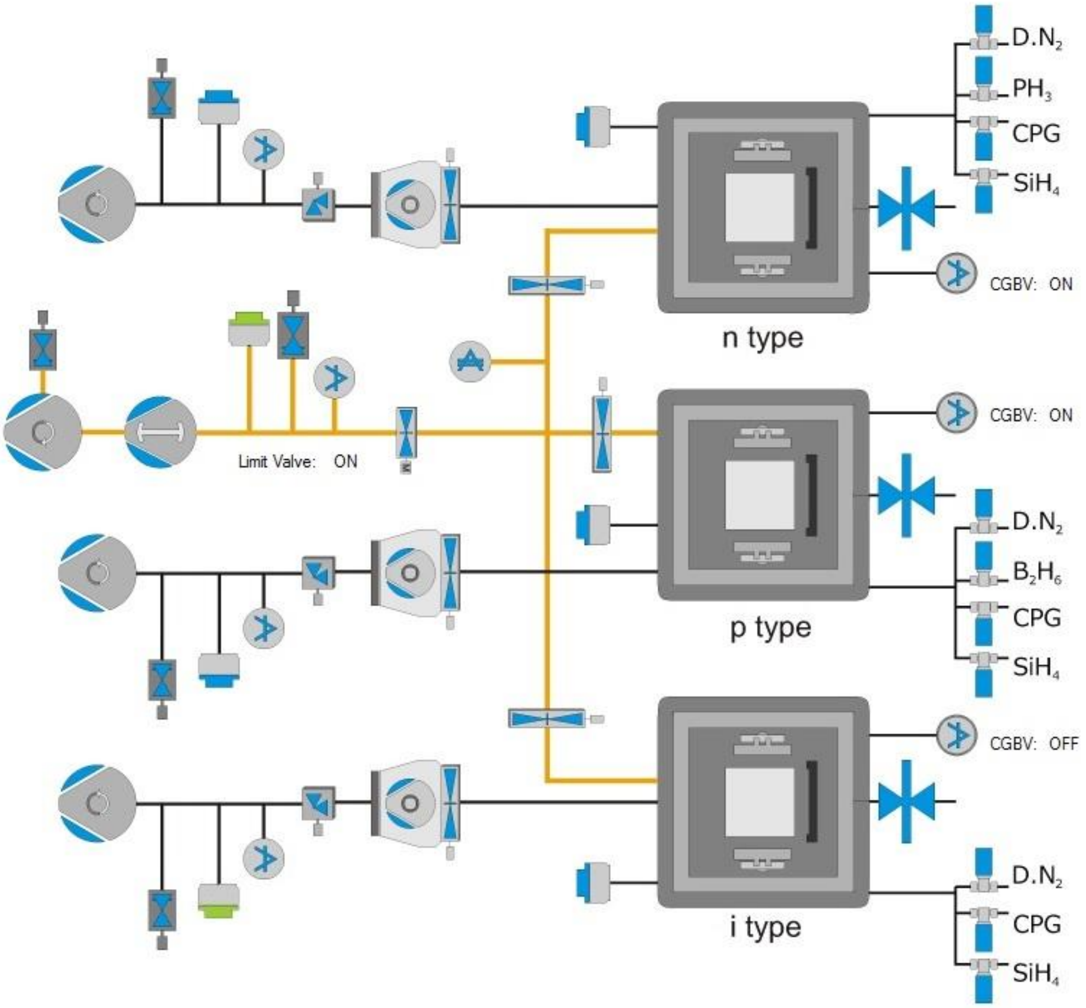

Fig 3.4 Schematic representation of CCP chambers and the common line

The chambers are driven by RF power source (13.56 MHz) that has a maximum power output of 600W and each chamber has its own power matchbox. The power is supplied to the upper electrode and lower electrode is the ground. The base pressure is less than $1x10^{-6}$ Torr and this level is provided by turbo-molecular pump. Each chamber also has a mechanical pump to decrease the pressure to 10^{-3} Torr. The distance between the electrodes is fixed at 2.5 cm. The gas entrance to the chamber is from cathode and the shower-head scheme is given in Figure 3.5. In order to maintain desired substrate temperature, three heaters, each has a capacity of

1000W are embedded in anode. To overcome excess heating by applied RF power, cathode has cooling water lines.

While deposition, turbo pump gate valves (TPGV) are closed and the suction is provided by common line (CL). CL consists of a mechanical pump, a root pump, a baratron vacuum gauge, a throttle valve and root pump gate valves (RPGV) for each chamber. The throttle valve controls and stabilizes the pressure while deposition with changing the position of its butterfly. The common line is connected to the exhaust system that is located outside the cleanroom, in which all the process gases are diluted and burned before entering the atmosphere.

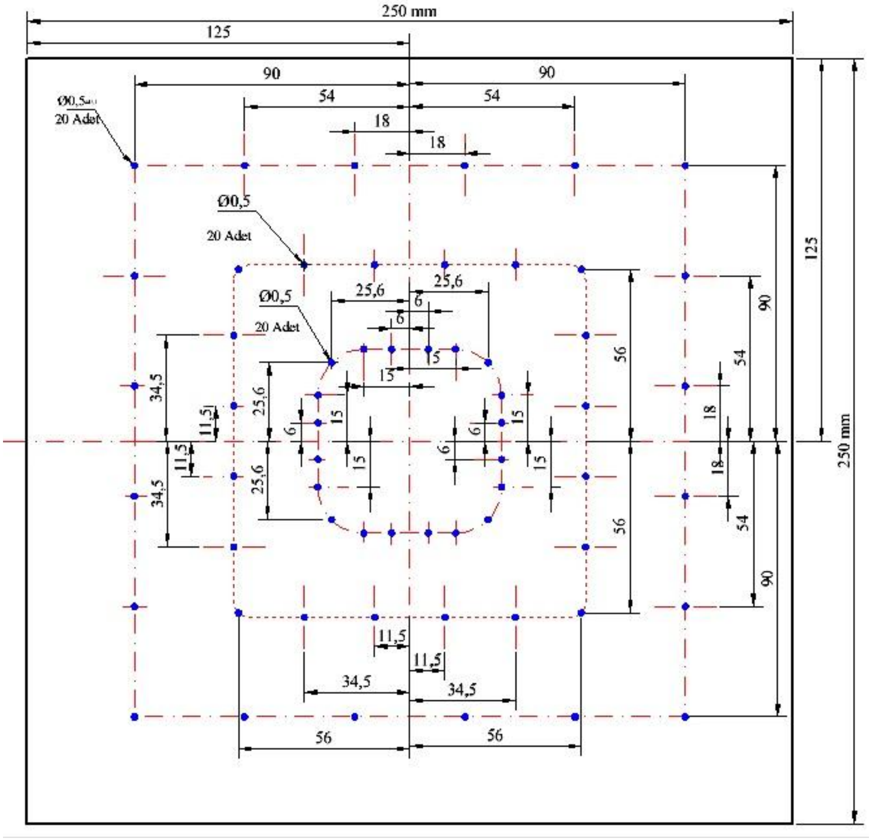

Fig. 3.5 CCP Shower-head Scheme

3.2.3 ICP Chamber

An inductively coupled plasma (ICP) is a type of plasma source in which the energy is supplied by electric currents which are produced by electromagnetic induction, that is, by time-varying magnetic fields. There are two types of ICP geometries: planar and cylindrical. In planar geometry, the electrode is a coil of flat metal wound like a spiral. In cylindrical geometry, it is like a helical spring. When a time-varying electric current is passed through the coil, it creates a time-varying magnetic field around it, which in turn induces azimuthal electric currents in the rarefied gas, leading to the formation of a plasma [25].

The ICP chamber of GÜNER has planar geometry and it is designed for the complete stack deposition of the solar cells. Therefore it has both doping gas inlets (B_2H_6 and PH_3), SiH_4, common process gases and dry nitrogen inlets. The gas entrance is located atop the chamber.

The RF power supply connected to the ICP chamber has a capacity of 5kW and the chamber has its own matchbox. The RF coil is placed between the chamber walls and the quartz wall. The pressure inside the chamber and inside the quartz partition must always be close to each other to avoid the cracking of the quartz. Therefore a pressure equalizer valve (PEQ-BV) is utilized. Moreover, while deposition, to avoid plasma formation inside the quartz partition a by-pass block valve (BP-BV) is utilized as seen in Figure 3.6. The base pressure of $1x10^{-6}$ Torr is provided by a mechanical and a turbo-molecular pump. The outlet of the mechanical pump is connected to the exhaust system to dilute and burn the process gases. Heaters are embedded in the lower electrode as same configuration as the CCP chambers. The deposition pressure is controlled and stabilized by a throttle valve placed in front of the turbo-molecular pump.

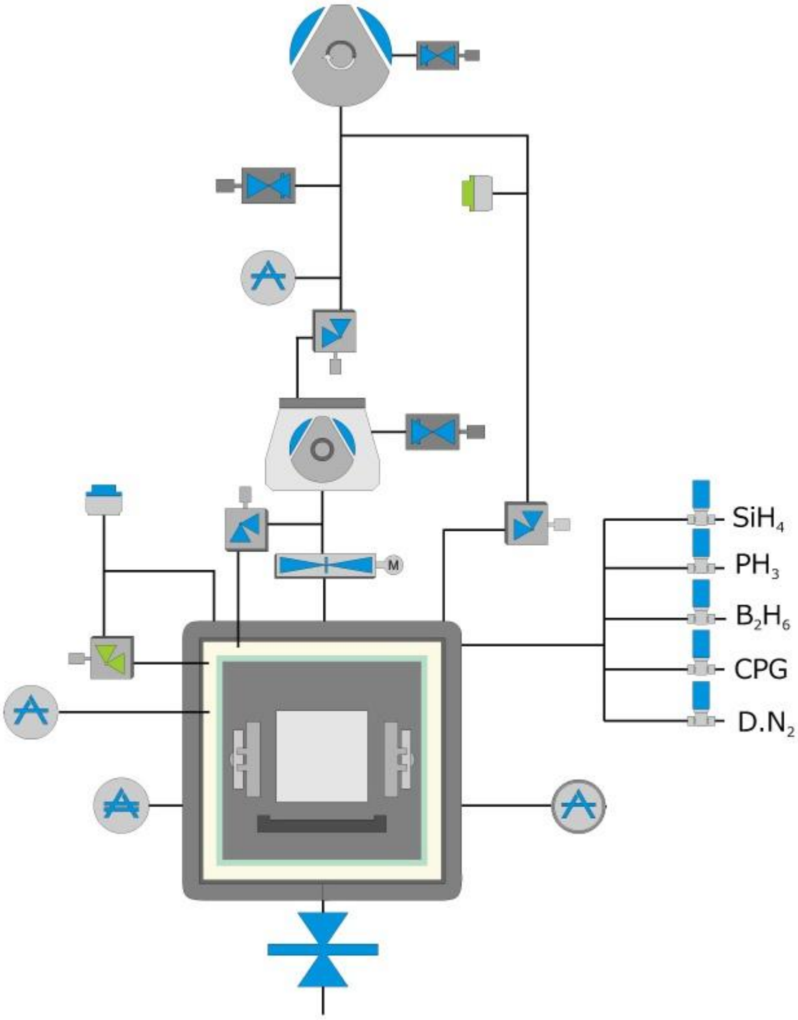

Fig 3.6 Schematic representation of ICP chamber

3.2.4 Sputtering Chamber

Sputtering is one of the most commonly used techniques in Physical Vapor Deposition (PVD) for depositing thin films. It is simply the ejection of atoms from the target due to high energy ion bombardment of energetic neutrals or ions. In other words, it could be considered as a cleaning method due to the ejection of atoms from the surface by the created collisions. These ejected atoms from the surface, namely the target, are deposited on the substrates [26]. A wide variety of materials such as metals, alloys and insulators can be deposited as thin films by this method.

Furthermore, sputter deposition facilitates the production of films of high melting point substances which are difficult to form by conventional evaporation [5].

In the sputtering chamber, two targets are located above the substrate. The first one is the silver (Ag), which is used generally as the back contact of solar cells, and the second is aluminum doped zinc oxide (AZO), which is used as the transparent conductive oxide (TCO). These targets are placed between three heaters. The heating in this chamber is done from above, whereas in all of the PECVD chambers it is done from below. Thus the heating period of the surface of the substrate is much shorter. The 5kW RF power source is connected to the magnetrons atop each target. After the matchbox, a switch is located to enable the user to select the proper magnetron. Magnetrons and the targets are cooled down by cooling water. The base pressure of 10^{-6} Torr is provided by a mechanical and a turbo-molecular pump. Since there is no flammable or toxic process gas present in sputtering, the mechanical pump is not connected to the exhaust system. For sputtering process, the noble gas argon is used which does not make any chemical bonds with the target surface. Moreover, it is the cheapest noble gas and its atoms are not as small as helium atoms. The gas entrances are separated for each magnetron and are given from the lateral sides of the chamber. Another robot arm is placed inside sputtering chamber for the horizontal movement of the substrate below the targets. While deposition, this arm makes oscillation-like movements (forward and backward) to achieve better thickness uniformity of the films. The deposition pressure is controlled and stabilized by a throttle valve placed in front of the turbo-molecular pump.

The sputtering chamber is represented in Figure 3.7.

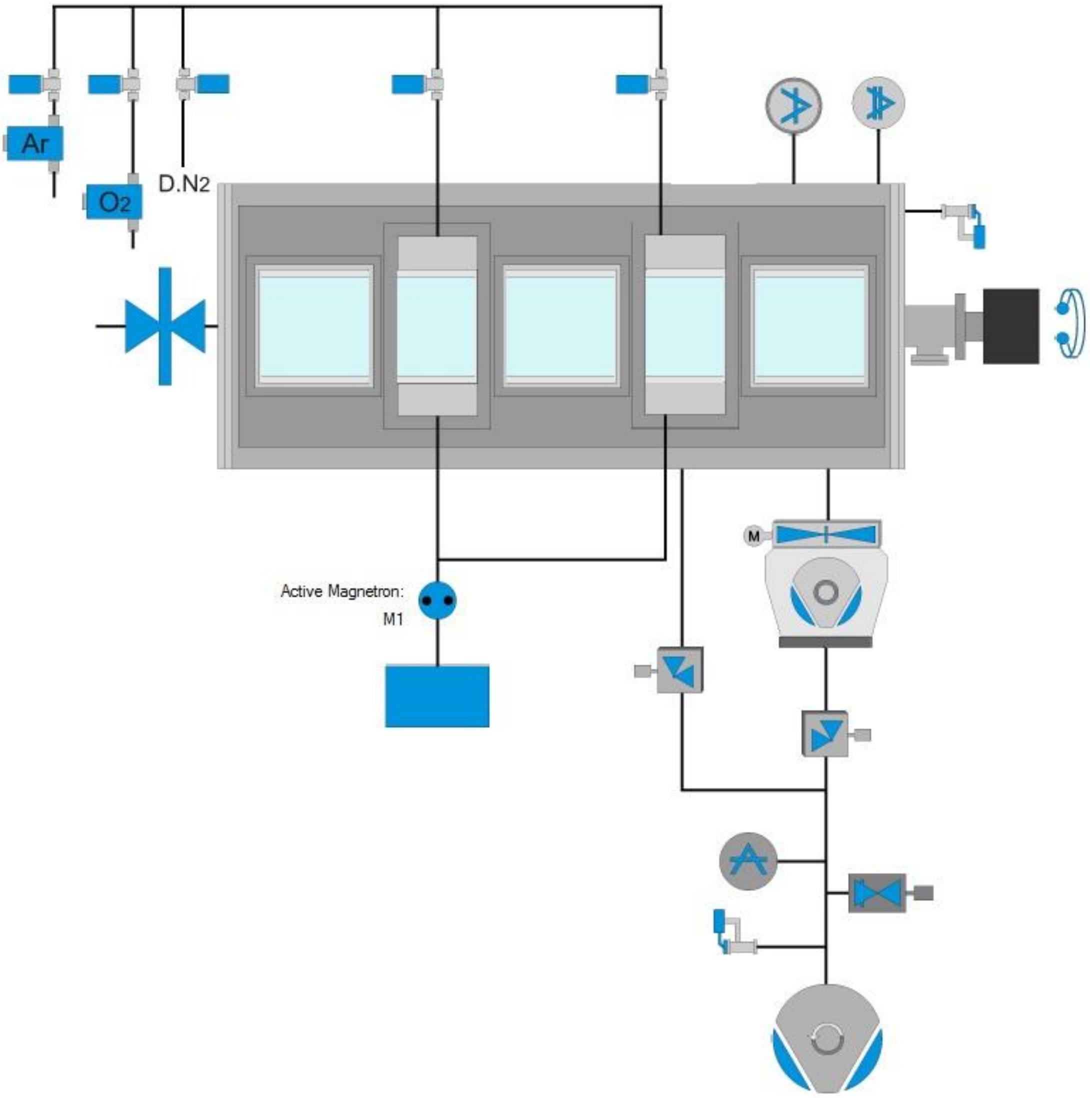

Fig 3.7 Schematic representation of sputtering chamber

3.2.5 Process Gas Lines

All the gas containers are located inside the gas room, which is located outside the Physics Department, METU. The configuration and distribution of the gas lines coming inside the cleanroom are illustrated in Figure 3.8.

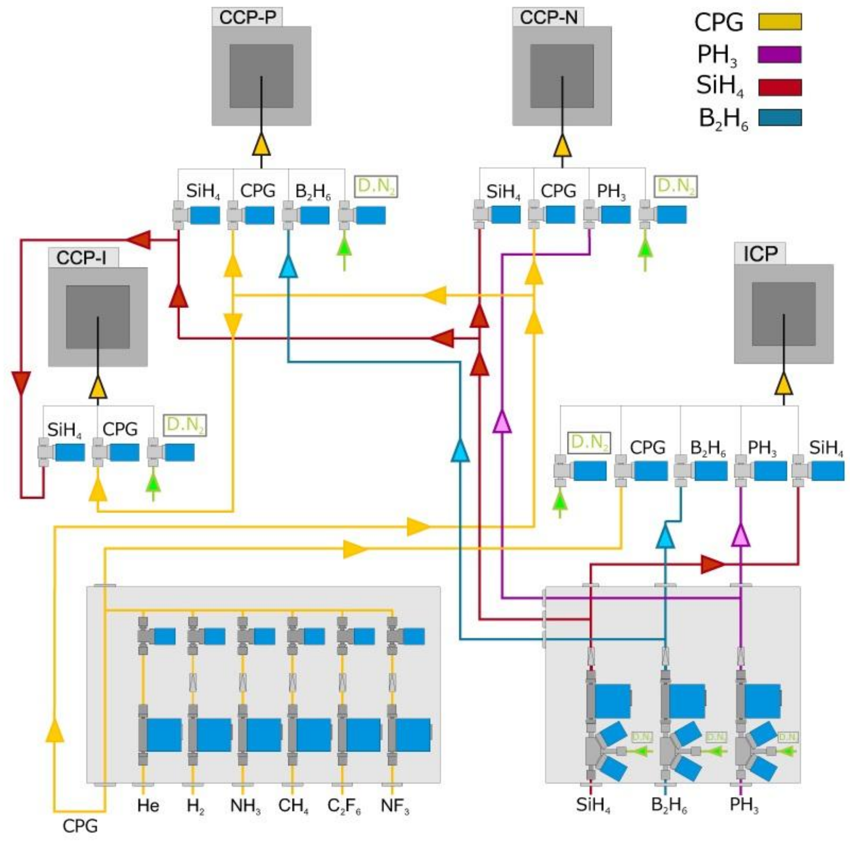

Fig. 3.8 The configuration of gas lines

3.3 Substrate Cleaning Procedures

3.3.1 Glass Cleaning

1. The 25x25x0.11 cm^3 Schott glass substrates are firstly washed in dishwasher with ordinary detergent.
2. They are immediately taken into cleanroom and placed into ultrasonic bath that contains 10 lt deionized (DI) water and 100 ml special detergent (Detojet) at 45 ºC for 15 minutes.
3. They are placed into ultrasonic bath that contains DI water at 50 ºC for 15 minutes.
4. They are rinsed with cold DI water for 15 minutes.
5. They are superficially dried with nitrogen gun.

6. They are placed into furnace for complete drying at 70 ºC for 1 hour under N_2 atmosphere.

3.3.2 Textured Si Wafer Cleaning

In the following two sub-sections, Radio Corporation of America (RCA) cleaning procedures are summarized [27].

3.3.2.1 RCA-1

1. Prepare RCA bath: 5 parts water (H_2O), 1 part 27% ammonium hydroxide (NH_4OH), 1 part 30% hydrogen peroxide (H_2O_2)

2. Soak wafer in RCA-1 bath at 70 °C for 10 minutes.

3. DI rinse for 2.5 minutes.

3.3.2.2 RCA-2

1. Prepare RCA-2 bath: 6 parts H_2O, 1 part hydrogen chloride (HCl), 1 part 30% H_2O_2

2. Soak wafer in RCA-2 bath at 70 °C for 10 minutes.

3. DI rinse for 2.5 minutes and dry.

Textured Si wafer cleaning procedure for HIT structure production is as follows;

1. Perform RCA-2.
2. HF/ HNO_3 [1:20] etching (pyramid rounding step) for 60 seconds.
3. DI rinse for 2.5 minutes.
4. Diluted %2.5 HF/ %2.5 HCI [1:1] for 90 seconds.
5. DI rinse for 2 minutes.
6. Perform RCA-1.

7. Diluted %2.5 HF/ %2.5 HCI [1:1] for 90 seconds.

8. DI rinse for 2 minutes and dry.

3.4 Plasma Cleaning

In each deposition, not only the substrate but also the walls and the cathode of the chamber are also covered with former deposition radicals. If no cleaning is performed, those deposited material will start to fall on the substrate as powder. Thus the film quality in terms of electrical and optical properties as well as film uniformity will be deteriorated. To avoid this undesired film growth, the chamber walls should be cleaned or etched by aggressive radicals.

Plasma etching is usually achieved by C_2F_6/O_2 mixture or NF_3. In order not to contaminate the chamber with carbon, NF_3/He mixture is used in GÜNER. Helium is used to decrease the rapid etching rate of fluor radicals by acting as dilutant. Moreover, He is a noble gas, so it does not interfere in any reaction.

The optimized process parameters for plasma cleaning are tabulated below in Table 3.1.

Table 3.1 Plasma Cleaning Parameters

NF_3 Flow Rate (sccm)	He Flow Rate (sccm)	Applied RF Power (W)	Pressure (Torr)
40	300	200	0.8

CHAPTER 4

LAYER OPTIMIZATIONS

4.1. Optimization of AZO Layer

4.1.1 Design of Experiments (DOE)

Sputtering parameters are deposition pressure, substrate temperature, applied RF power and argon flow rate. Since the residence times of the molecules are controlled by pressure, argon flow rate is eliminated from this study. It is fixed at 125 sccm. The starting matrix is tabulated in Table 4.1. Sample codes are labeled same as done in GÜNER logbook. In this matrix, power was changed for three depositions, whereas pressure and temperature were changed only twice.

Table 4.1. DOE of AZO calibration set

Sample Code	Applied Power (W)	Pressure (mTorr)	Substrate Temperature (^oC)
AZO125	400	3	150
AZO126	600	3	150
AZO127	800	3	150
AZO129	600	3	100
AZO130	600	5	150

4.1.2 Thicknesses, Average Deposition Rates and Uniformity

4.1.2.1 Profilometer Results

For the determination of the film thicknesses, three one-side polished silicon steps were placed on the glass substrate; one at the center, one at the edge, and the leftover at the middle of these two. They might not reflect the same thickness deposited on the glass since (1) the distance to the target is lower (a few microns) and (2) materials are different.

In Table 4.2, values evaluated from profilometer can be seen. The uniformity calculations were made by the formula below;

$$Uniformity = \frac{\text{Max} - \text{Min}}{2 \text{ x } Average} \qquad \text{Eqn (4.1)}$$

Average deposition rates were given in terms of nm/pass instead of nm/min, because time is not a proper unit for this case (substrate make an oscillation-like motion under the target, so it does not face the plasma all the time).

Table 4.2 Results from profilometer

Sample Code	Applied Power (W)	Pressure (mTorr)	Substrate Temp (^{o}C)	Thickness at Center	Thickness at Middle	Thickness at Edge	Average Thickness (nm)	Uni formity	Average Dep Rate (nm/pass)
AZO125	400	3	150	260	180	180	207	0.19	34.5
AZO126	600	3	150	280	180	130	197	0.38	65.7
AZO127	800	3	150	180	150	260	197	0.27	98.5
AZO129	600	3	100	280	230	120	210	0.38	70
AZO130	600	5	150	200	180	200	193	0.05	64.3

It is easily seen from the table above, deposition rates increase with power. However, uniformity of the films is very poor at 3 mTorr. Earlier, it was decided to lower the deposition pressure to reduce the manual cleaning period of the chamber. So, the typical working pressure is 3 mTorr for AZO deposition.

4.1.2.2 Ellipsometer Results

The calculations done were the same as the previous section. However, instead of three points, ten points were modeled by ellipsometer. The obtained values are tabulated in Table 4.3 in terms of nm. The results can be seen in Table 4.4.

Table 4.3 Thickness mapping by Ellipsometer

	AZO 125	AZO 126	AZO 127	AZO 129	AZO 130
Center	212	221	231	221	192.7
Corner	235	224	235	203	183.9
N200	247	225	152 (outlier)	207	195.9
N300	251	229	228	223	195.6
N400	241	224	228	225	194.6
d/2	242	226	220	222	179.9
H200	245	220	220	226	196.9
H300	240	226	231	227	196
H400	215	228	215	218	195.3
H500	212	224	213	220	194.9

Table 4.4 Results from Ellipsometer

	AZO 125	AZO 126	AZO 127	AZO 129	AZO 130
Average thickness (nm)	234	225	225	219	193
Uniformity	0.08	0.02	0.05	0.04	0.04
Average Deposition Rate (nm/pass)	39	75	112.5	73	64.3

The uniformity values obtained from ellipsometer are so fine when compared to profilometer results. As mentioned earlier, this is most probably due to material differences. It might be easier to deposit uniformly on amorphous material than polished crystalline Si. There is no color difference on glass, whereas Si steps have different colors visually.

4.1.3 Sheet Resistance, Resistivity and Conductivity (by four point probe)

For the sheet resistances, seven points were averaged for each sample and tabulated in Table 4.5 with resistance and conductivity values. To calculate resistivity, average thicknesses obtained from profilometer was used.

Table 4.5 Sheet resistance, resistivity and conductivity values

Sample Code	Applied Power (W)	Pressure (mTorr)	Substrate Temp (^oC)	Average Sheet Resistance (Ω/□)	Resistivity (Ω cm)	Conductivity (S / cm)
AZO125	400	3	150	47.7	9.86×10^{-4}	1014.41
AZO126	600	3	150	42.4	8.34×10^{-4}	1199.23
AZO127	800	3	150	42.4	8.34×10^{-4}	1199.23
AZO129	600	3	100	44.1	9.26×10^{-4}	1079.80
AZO130	600	5	150	54.5	1.05×10^{-3}	949.07

Only pressure seems to have an effect on the electrical properties of the films. However, it has a slight negative effect.

4.1.4 Structural Analyses (by XRD)

AZO crystal structure is hexagonal wurtzite as represented in Figure 4.1 [28] with lattice constants of a=3.24 Å and c=5.19Å [29]. A typical XRD spectrum for AZO thin films deposited in GÜNER can be seen in Figure 4.2. Presence of the intense (002) peak (and also (004)) implies the grains are strongly c-axis oriented, which means columnar growth (perpendicular to the substrate) of the film [30]. (002) peak positions and Full Width at Half Maximum (FWHM) values are determined by using Peak Fit and the results are given in Table 4.6. The bulk (polycrystalline) values [31,32] were also added to the table.

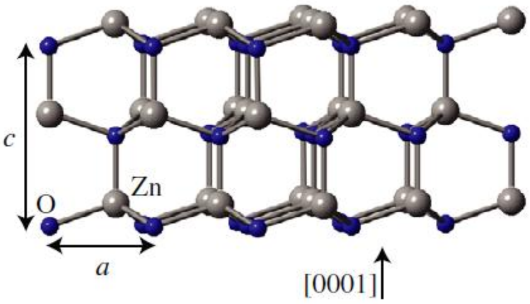

Fig. 4.1 Wurtzite structure of ZnO

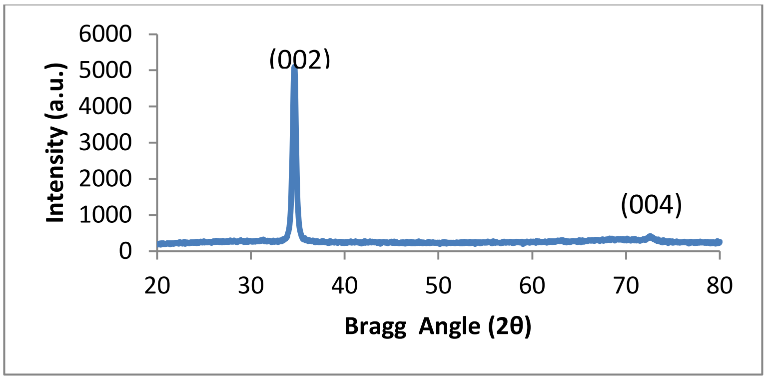

Fig. 4.2 XRD spectrum of AZO130 coded film

Table 4.6 (002) peak positions and FWHM values of AZO films

Sample Code	Applied Power (W)	Pressure (mTorr)	Substrate Temp (°C)	(002) peak position	(002) peak FWHM	Grain Size (nm)
AZO125	400	3	150	34.90	0.4900	17.00
AZO126	600	3	150	34.75	0.5294	15.72
AZO127	800	3	150	34.70	0.5133	16.21
AZO129	600	3	100	34.70	0.4958	16.79
AZO130	600	5	150	34.65	0.3993	20.84
Bulk ZnO (polycrystalline)				34.45 [31]	≈0.35 [32]	23.76*

* Value calculated from Scherrer formula

(002) position shift to higher values implies compressive stress formation on the films (shift to lower values means tensile stress) [31,32]. It can be easily seen from the table above, all of the films deposited for considered matrix have formed compressive stress. Increasing the power from 400 to 800W lead to a slight decrease in peak position (stress). Substrate temperature (in the DOE range) has no effect on peak position. Increasing the deposition pressure from 3 to 5 mTorr, decreased compressive stress a little.

Increase in (002) peak FWHM, in other words broadening of (002) peak corresponds to the decrease in grain size. When grain size decreases, grain boundary increases, which means the number of scattering centers for carriers increase and Hall mobility decreases [33,34]. FWHM values determined were so high when compared with literature. It means that our films' grain sizes are so small. The best film was deposited at high pressure (5 mTorr) in terms of FWHM.

The grain size (t) can be calculated by Scherrer formula;

$$t = \frac{0.9\lambda}{B\,cos\theta} \qquad \text{Eqn (4.2)}$$

where λ is the X-Ray wavelength, B is the corrected peak width and θ is the Bragg angle [34]. The calculated values and the expected grain size value are tabulated above.

4.1.5 Band Gap (by UV-Vis)

ZnO exhibits a direct band-gap (E_g) of 3.2-3.4 eV [29]. This value might be adjusted with different doping atoms and doping concentrations. However, our target fixed at 2 wt. % Al. So to change the E_g, only tools that are at hand are process parameters.

A typical UV-Vis transmission spectrum can be seen in Figure 4.3 for AZO125 coded sample. The range of the wavelength is 200-1100 nm.

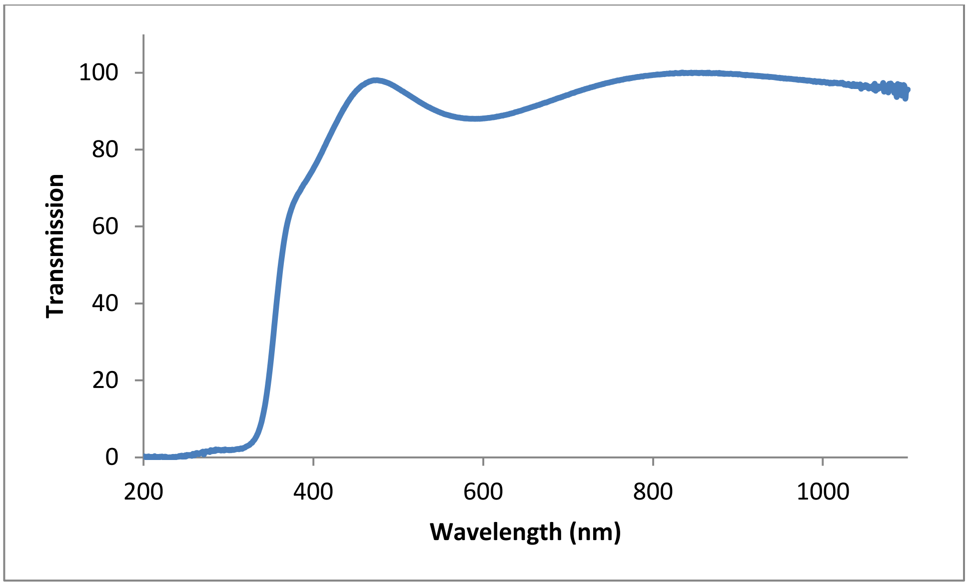

Fig. 4.3 UV-Vis spectrum of AZO125 coded film

To calculate absorption coefficient, below relation was used. Average thickness (d) was taken as 200 nm for each sample.

$$\alpha(\lambda) = -\frac{1}{d}\ln(T(\lambda)) \qquad \text{Eqn (4.3)}$$

The relation between absorption and band gap values is given as;

$$(\alpha\lambda\nu) = A(\lambda\nu - E_g)^{1/2} \qquad \text{Eqn (4.4)}$$

Then, $(\alpha\lambda\nu)^2$ vs $\lambda\nu$ is plotted in Figure 4.4, since AZO is a direct transition type semiconductor [3]. In Figure 4.5, the inspected portion of the curve is magnified and the intersection values (E_g) are listed in Table 4.7.

It might be concluded that the only parameter that affects the band gap is deposition pressure. A slight increase from 3 to 5 mTorr, decreased the band gap from 3.30 to 3.23 eV. At low power (400W), band gap is a little lower (1%).

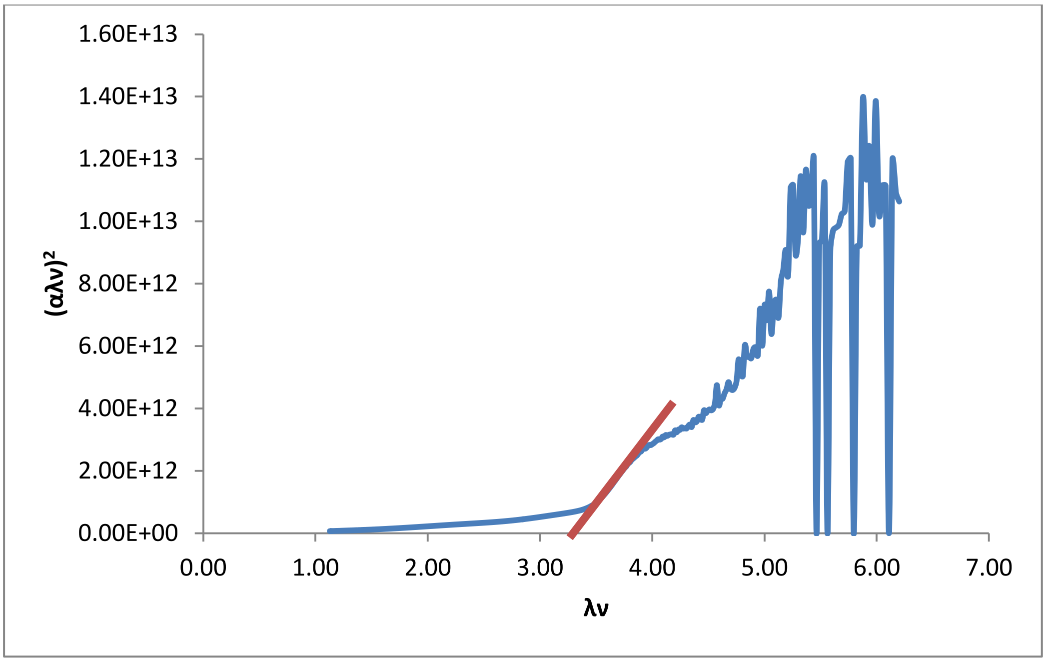

Fig. 4.4 $(\alpha\lambda\nu)^2$ vs λν plot of AZO125 coded film

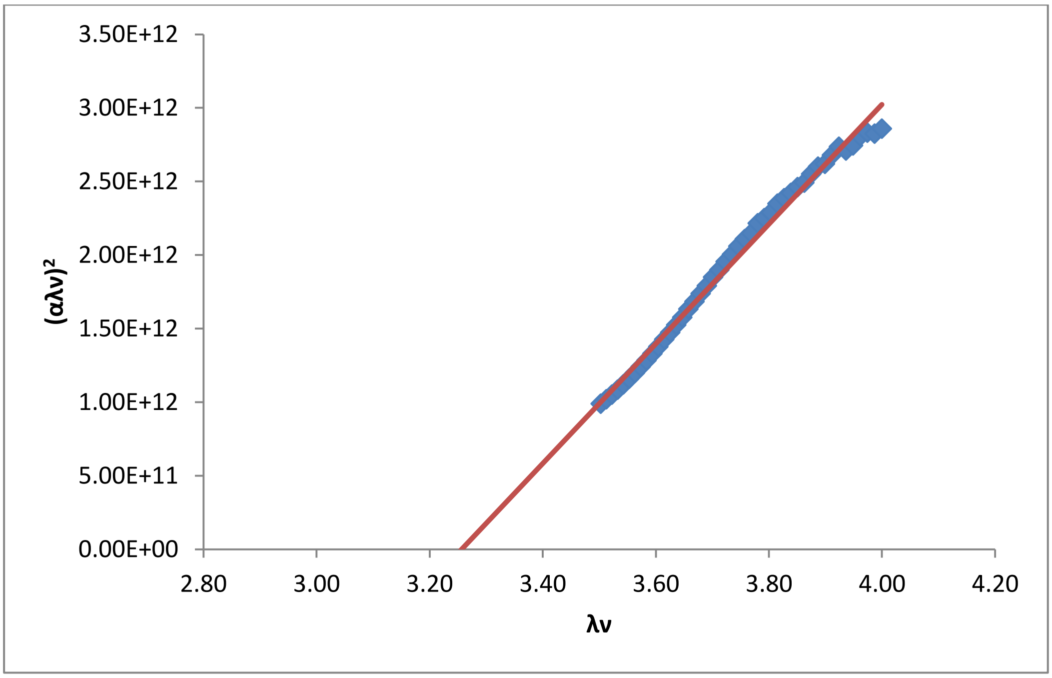

Fig. 4.5 Intersection of $(\alpha\lambda\nu)^2$ vs λν plot of AZO125 coded film

Table 4.7 E_g values of AZO films

Sample Code	Applied Power (W)	Pressure (mTorr)	Substrate Temperature (°C)	Band Gap (eV)
AZO125	400	3	150	3.26
AZO126	600	3	150	3.30
AZO127	800	3	150	3.30
AZO129	600	3	100	3.29
AZO130	600	5	150	3.23

4.1.6 Transmission and Reflection Measurements (by Integrated Sphere)

Transmission measurements were conducted via integrated sphere and resulting plot from film side is given in Figure 4.6.

Increasing power lead to blue shift while increasing pressure resulted in red shift. Temperature did not have any significant effect on transmission. Although it is hard to differentiate amongst the films, AZO 130 is more preferable for a solar cell; because it has better transmission in red region and also in IR.

Transmission from glass substrate side was also measured and plotted in Figure 4.7. The same observations can be seen as the transmission from film side. However, this time temperature have an effect on transmission. In 400-600 nm range, decreasing the substrate temperature has a negative effect in transmission.

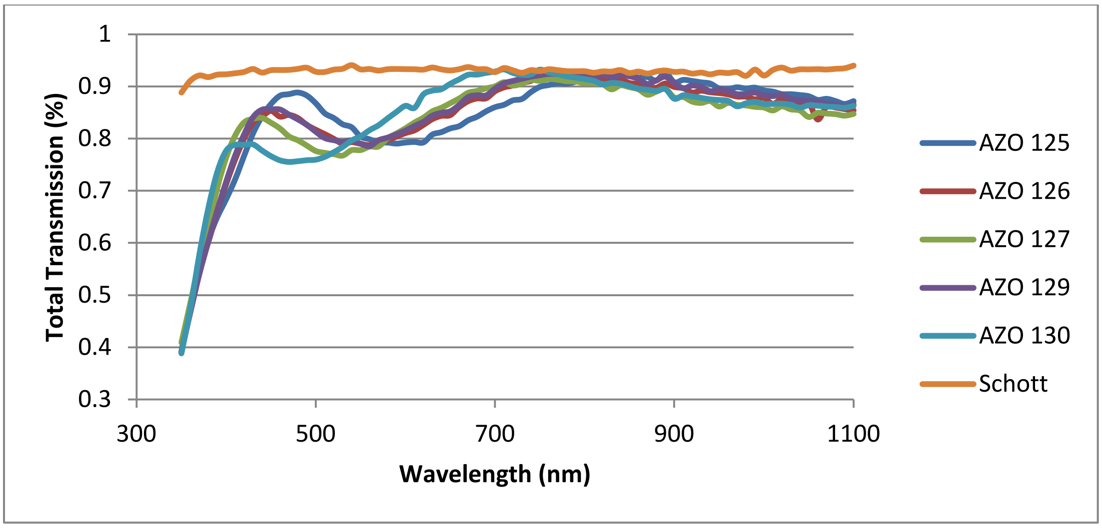

Fig. 4.6 Transmission of AZO films from film side

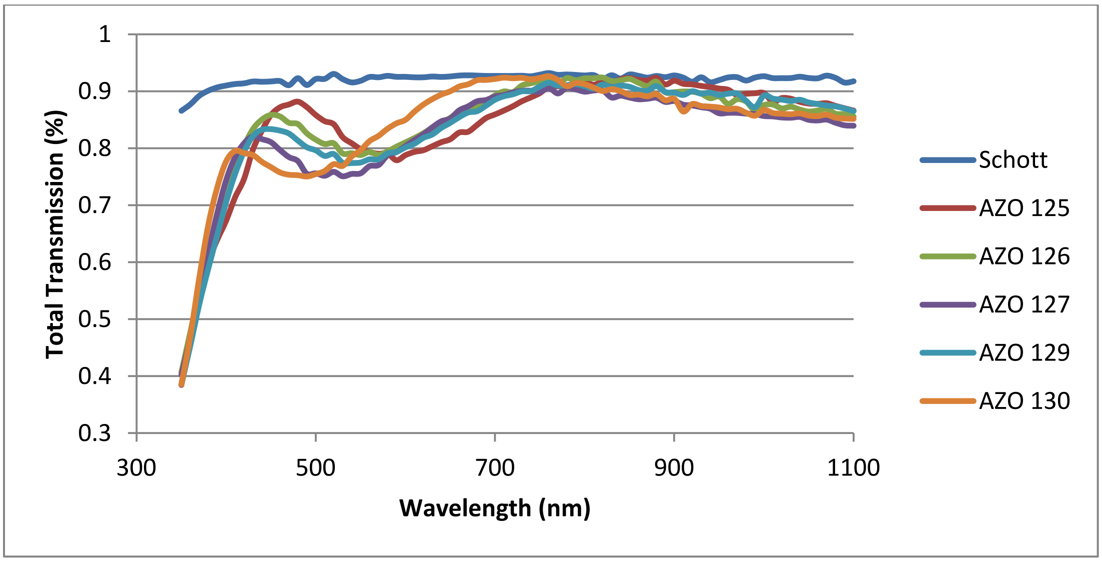

Fig. 4.7 Transmission of AZO films from glass side

Reflection measurements were also done and resulting plot is given in Figure 4.8. According to the relation (R = 1 - T), the results are as expected. In Figure 4.9, transmission, reflection and absorption plots were plotted for AZO 130 coded film. After 540 nm, there is no absorption.

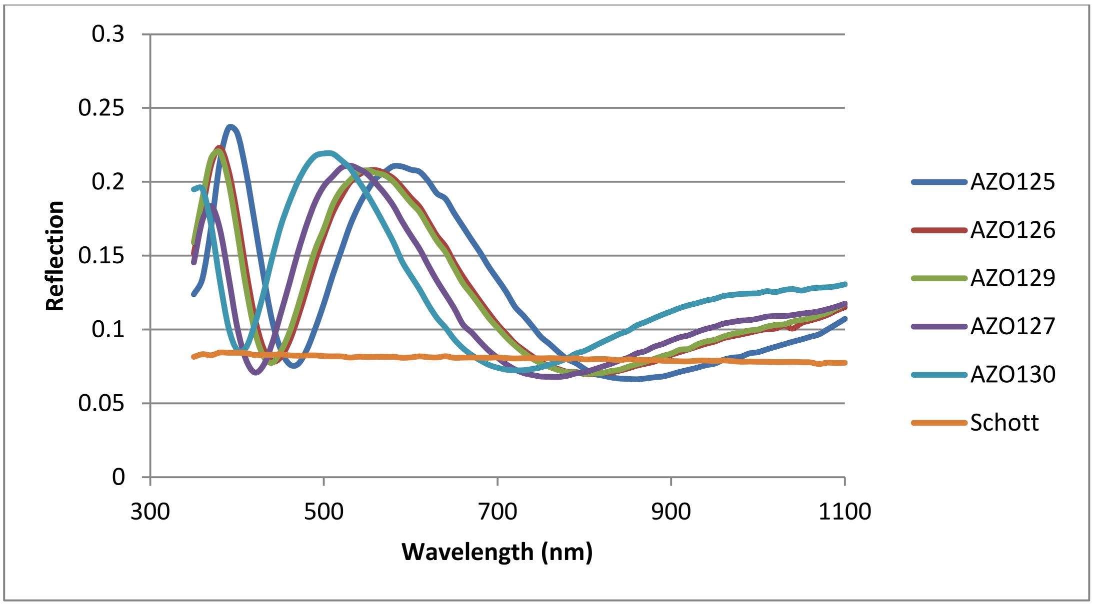

Fig. 4.8 Reflection of AZO films

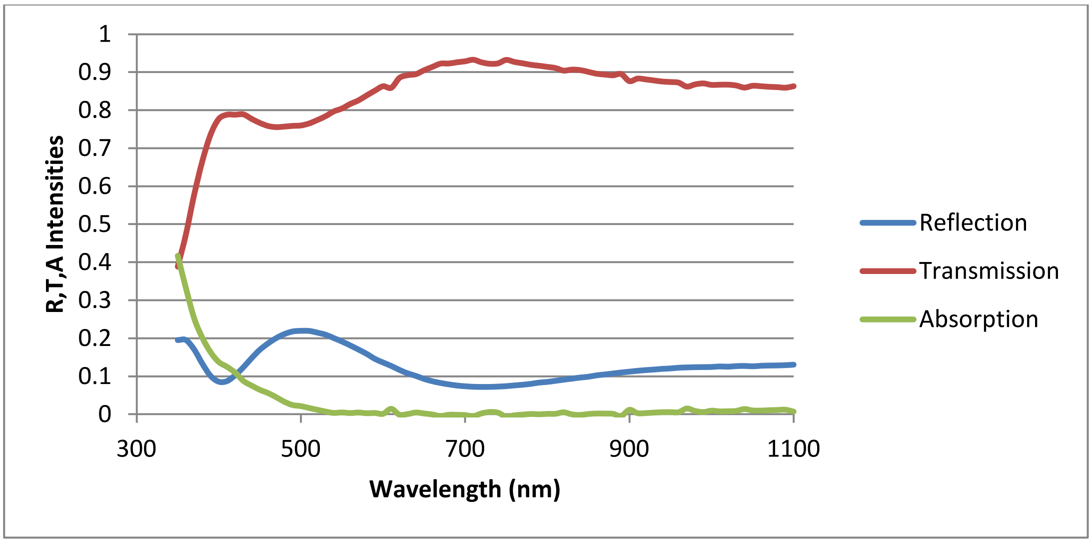

Fig. 4.9 Transmission, Reflection and Absorption of AZO 130 coded film

4.1.7 Conclusion

The first conclusion from the characterizations above, GÜNER deposited AZO thin films have high quality in terms of conductivity and transmission. Those two properties are the main features of transparent conductive oxides (TCO). Conductivity values are at the order of 10^3 S/cm and films have around 90-92 % transmission.

Secondly, uniformity of AZO films are so fine for 25 x 25 cm^2 samples.

Lastly, in terms of band-gap and structure, films exhibit the same properties as the literature.

However, these features are not so tunable with GÜNER's sputtering chamber. Only pressure is a tuning tool as a process parameter. To go over deposition pressure may lead to better films, but it is not needed at this stage of solar cell production.

4.2 Optimization of Intrinsic a-Si Layer

4.2.1 Design of Experiments (DOE)

The experiment set given in Table 4.8 was used to optimize the intrinsic amorphous silicon layer and also the i-type CCP chamber. The parameters for these depositions were substrate temperature, deposition pressure, applied power and silane (SiH_4) flow rate. After a long term of heater design, the new heaters were installed to the chamber and temperatures up to 225 °C could be reached. In the table below, the experiments were coded as run numbers. The first three are the repeating experiments so they are named as zero. They were made after four normal experiments to see the reproducibility of the samples. The parameters of these repeating runs were chosen as the old design's optimum values.

Table 4.8. DOE Matrix

run	T_{subs}	P_{dep} (Torr)	Pow (W)	F_{SiH4} (sccm)
0	200	0.78	100	250
0_2	200	0.78	100	250
0_3	200	0.78	100	250
1	175	0.5	50	200
2	225	0.5	50	200
3	175	0.5	150	200
4	225	0.5	150	200
5	175	1	50	200
6	225	1	50	200
7	175	1	150	200
8	225	1	150	200
9	175	0.5	50	300
10	225	0.5	50	300
11	175	0.5	150	300
12	225	0.5	150	300

4.2.2 Sample Preparation

Corning glass (25x25x0.22 cm^3) was used as the substrate in this optimization set for intrinsic a-Si:H deposition in GÜNER system. It can be used for Raman spectroscopy, optical and conductivity measurements. Moreover, a piece of low doped silicon wafer (10-20 Ω) was placed on this glass substrate for the FTIR measurements. Three one side polished silicon wafers were used to determine the film thicknesses, uniformity and the deposition rates. Two quartz sticks were placed for the electron spin resonance (ESR) measurements which is conducted by Dr. Zaki Saleh. His results are excluded in this thesis. The positions of the samples on glass can be seen in Figure 4.10.

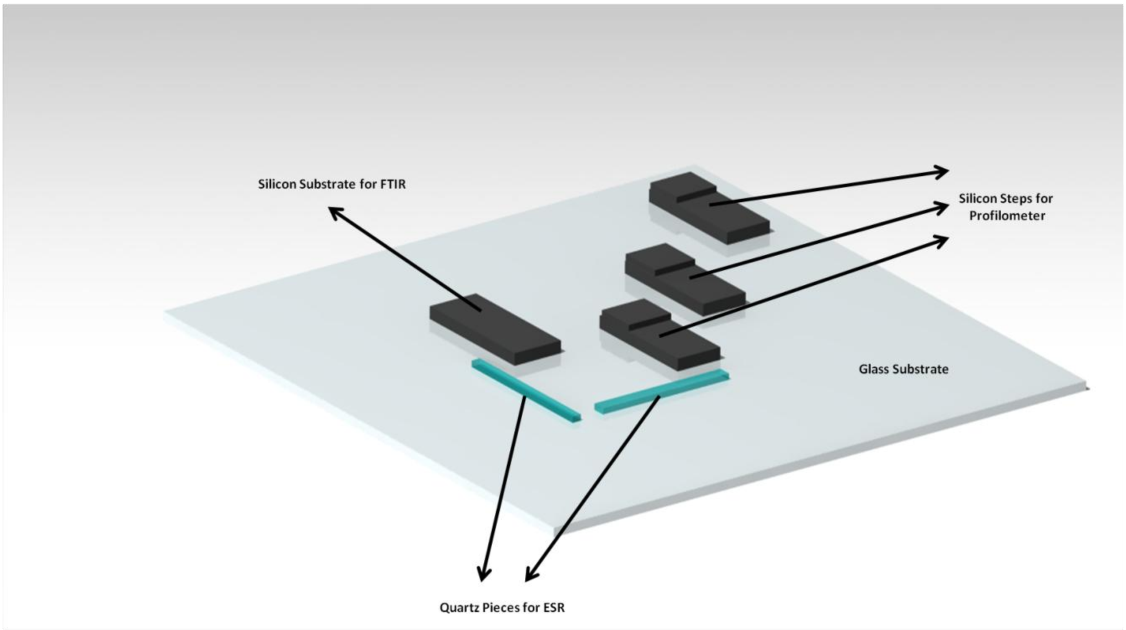

Fig. 4.10 Positions of the samples on glass

4.2.3 Thicknesses and Average Deposition Rates by Profilometer and Ellipsometer

Table 4.9 gives information about the thicknesses of the films and average deposition rates. For the profilometer measurements, three one-side polished silicon steps were placed on the substrate. One at the center, one at the edge and the last one was placed in the middle of the other two. Generally the thickness at the edge was different than the other two value, and it can also be visually understood. So for the uniformity, this value may be ignored. Ellipsometer measurements were done on the center of the substrate. So the substrates for the thickness measurements are different. However, the optical and the mechanical measurements are in agreement. Run numbers 5 and 6 were seem to be the best in terms of uniformity and deposition rates.

Table 4.9 Thicknesses and average deposition rates of the intrinsic films by profilometry and ellipsometry

	thickness (nm)					Av. Dep Rate (nm/s)	
	profilometer				ellipsometer	profilometer	ellipsometer
run	**Center**	**Middle**	**Edge**	**Av.**	**Center**		
0	peeled	peeled	200	200	peeled	0.22	-
0_2	peeled	190	170	180	peeled	0.4	-
0_3	peeled	peeled	peeled	-	peeled	-	-
1	150	125	130	135	133	0.27	0.27
2	83	75	60	72.7	95	0.15	0.20
3	137	132	165	144.7	154	0.35	0.37
4	122	100	peeled	111	124	0.19	0.21
5	295	297	200	264	313	0.66	0.78
6	294	320	195	269.7	318	0.67	0.79
7	peeled	peeled	peeled	-	peeled	-	-
8	peeled	peeled	peeled	-	peeled	-	-
9	100	80	120	100	-	0.25	-
10	135	105	100	113.3	126	0.09	0.10
11	150	157	peeled	153.5	150	0.17	0.17
12	105	90	160	118.3	-	0.13	-

4.2.4 Hydrogen Content by FTIR

FTIR transmission analyses were conducted in Lab 118 for the determination of the hydrogen content in the films. A typical transmission spectrum can be seen in Figure 4.11. The vibration modes of silicon peaks are tabulated in Table 4.10.

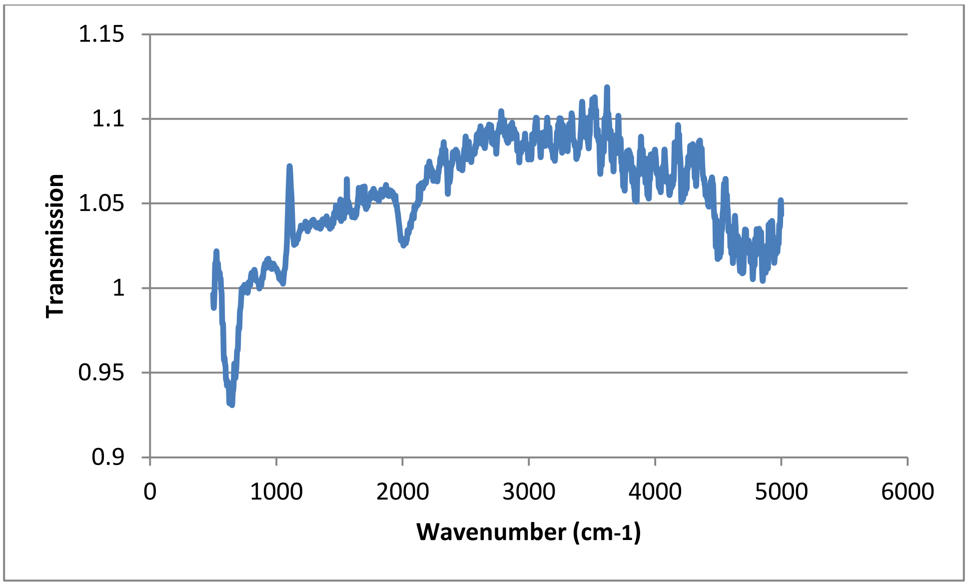

Fig. 4.11 Transmission spectrum of sample coded as run3

Table 4.10 Vibration modes of a-Si:H

Wavenumber (cm^{-1})	Mode
640	Si-Si bending
2000	Si-H stretching
2090	$Si\text{-}H_2$ or $Si\text{-}H_3$ stretching
1080	Si-O

For the calculation of the hydrogen content in the films, Equation 4.5 was used [35]. In this calculation only the bending mode peak that is located around 640 cm^{-1} is used as done in the literature. For the extraction, sectioning, base-line addition, etc. Peak Fit was used.

$$C_H = \frac{A_w}{N_{Si}} \int_{\nu_{r/w}} \frac{\alpha(\nu)}{\nu} d\nu \approx \frac{A_w}{N_{Si}} \sum_{\nu_{r/w}} \frac{\alpha(\nu)}{\nu} \Delta \nu \qquad \text{Eqn (4.5)}$$

where $\alpha(\nu)$ is the absorption coefficient, $\nu_{r/w}$ stands for the rocking-wagging bands around 640 cm^{-1}, $A_w = 1.6 \times 10^{19}$ cm^{-2} is the proportionality constant and $N_{Si} = 5 \times 10^{22}$ cm^{-3} is the atomic density of pure silicon [35].

The absorption coefficient is related to the transmission as the below relation;

$$\alpha = \frac{-\log(T)}{d} \qquad \text{Eqn (4.6)}$$

where d is the thickness of the film.

After substituting absorption coefficient and the values in Equation 4.1, the resulting equation becomes;

$$C_H \approx \frac{6400}{d\,[nm]} \sum_{\nu_{r/w}} \frac{-\log(T)}{\nu} \qquad \text{Eqn (4.7)}$$

The results are given in Table 4.11. Run number 0_3 (the repeating run) could not be calculated due to delamination. Moreover, the delaminated runs 7 and 8 are assumed to have a thickness of 300 nm and the repeating runs (0 and 0_1) have a thickness of 200 nm.

The best quality plasma grown a-Si:H films have less than 10% hydrogen content. If hydrogen concentration exceeds 25%, hydrogen-related voids in the film occurs [2].

Table 4.11 Hydrogen contents of the films

Run No	C_H (%)
0	8.95
0_2	14.48
1	10
2	11.5
3	12.9
4	15.2
5	7.38
6	7.64
7	11
8	8.91
9	12.18
10	11.18
11	15.57
12	19.23

4.2.5 Conductivity Measurements

Conductivity measurements for all amorphous silicon films have been made. Ohmic contacts were prepared by evaporating a few micrometers of Aluminum on the amorphous layer and then annealing under nitrogen for an hour at 180 ^{0}C was done. Then an electric voltage V was applied between the two contact pads and resulting electrical current was measured[2].

The photoconductivity measurements were done under AM1.5 sun illumination. It is given by the formula below:

$$\sigma_p = \frac{I}{U}\frac{w}{ld} \qquad \text{Eqn (4.8)}$$

where U is the applied voltage, w is the distance between the two electrodes, d is the film thickness, I is the measured current, and *l* is the length of the electrodes.

In Table 4.12, the photoconductivity results for a-Si:H thin film for different plasma conditions are tabulated.

Table 4.12 Photoconductivity values for intirinsic a-Si:H prepared with different deposition conditions

a-Si:H						
run	**T_{subs}**	**P_{dep} (Torr)**	**Pow (W)**	**F_{SiH4} (sccm)**	**Av. Dep Rate (nm/s)**	**σ- photo. 1/ohm.cm**
1	175	0.5	50	200	0.27	1.9342E-04
2	225	0.5	50	200	0.15	6.0038E-06
3	175	0.5	150	200	0.35	2.0107E-05
4	225	0.5	150	200	0.19	4.5998E-06
5	175	1	50	200	0.66	2.8292E-04
6	225	1	50	200	0.67	2.8298E-04
7	175	1	150	200	peeled	
8	225	1	150	200	peeled	
9	175	0.5	50	300	0.25	1.5738E-05
10	225	0.5	50	300	0.09	1.7867E-04
11	175	0.5	150	300	0.17	1.4488E-05
12	225	0.5	150	300	0.13	2.2651E-05

The photoconductivity should be higher than 1x 10^{-5} - 10^{-4} Ω^{-1} cm^{-1} [2].

4.2.6 Band Gap by Ellipsometer

The model used in ellipsometry also gives band gap of the films. The results were tabulated below. It can be seen that the band gaps of the material does not change so much in this parameter range. The missing runs in Table 4.13 cannot be modeled yet.

Table 4.13 Band gaps by ellipsometry

Run	Eg (eV)
1	1.74
2	1.69
3	1.74
4	1.76
5	1.74
6	1.62
10	1.69
11	1.76

4.2.7 Structure by Raman Spectroscopy

The structural analyses made by Raman spectroscopy showed that the first five runs yielded in amorphous phase. However, after the last measurement the camera of the spectrometer is damaged and now it is not working properly. On the other hand, according to our older experiments no crystalline phase in this matrix is expected since the hydrogen dilution, pressure and power are low for phase transition. Raman spectrum of the first six runs can be seen in Figure 4.12. They all are typical for amorphous silicon.

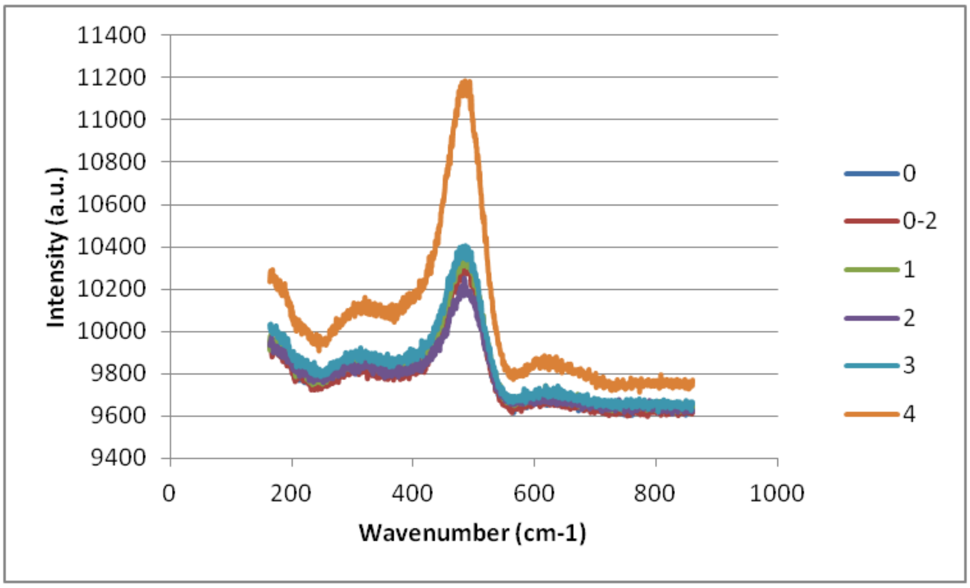

Fig. 4.12 Raman spectra

4.2.8 Plasma Diagnostics by Optical Emission Spectroscopy

In each deposition, at least 5 optical emission spectrum was taken. Then the average of those data was mentioned here. In Table 4.14, the ratios of the SiH, H_β, H_α can be seen, which are around 414, 486 and 656 nm in the spectrum, respectively [36]. The decrease in SiH/H ratios implies the depletion of the silane. The best films deposited were run numbers 5 and 6. All peak ratios were nearly the highest values for 5 and 6.

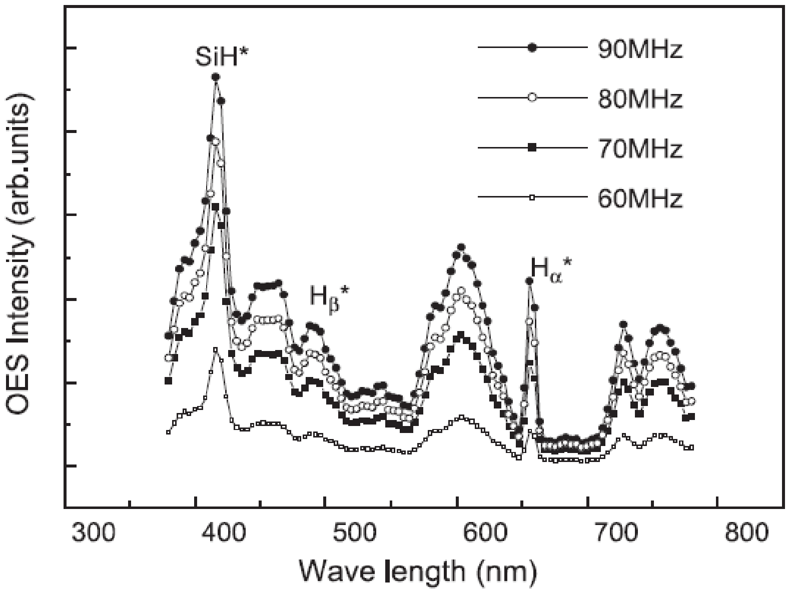

Fig 4.13 A representative silane plasma OE spectrum [36]

Table 4.14 Ratios of the emission peaks

Run No	SiH / H_α	SiH / H_β	H_β / H_α	Stability
0_1	1.04	1.48	7.11E-01	Peeled
0_2	1.07	1.62	6.62E-01	Peeled
0_3	1.05	1.72	6.14E-01	Peeled
1	1.19	1.42	8.52E-01	
2	9.85E-01	1.16	8.56E-01	
3	8.31E-01	1.24	6.78E-01	
4	7.37E-01	1.19	6.17E-01	
5	1.39	1.71	8.16E-01	
6	1.36	1.55	8.75E-01	
7	6.44E-01	1.13	5.70E-01	Peeled
8	7.95E-01	1.42	5.60E-01	Peeled
9	1.23	1.62	7.61E-01	
10	1.27	1.66	7.68E-01	
11	7.64E-01	1.54	4.93E-01	
12	6.80E-01	1.36	5.05E-01	

4.2.9 Effects of Process Parameters on Deposition Rate, Uniformity and Hydrogen Content

JMP program was used for the statistical analyses. The process parameters were substrate temperature, deposition pressure, applied power and silane flow rate. Their effects on the film properties such as thickness uniformity, deposition rate, hydrogen content, band gap, photo-conductivity were investigated.

The analyses for the average deposition rate (obtained by profilometer) showed that only deposition pressure and substrate temperature have significant effect on the film properties. The asterisk marked (*) terms seen in Table 4.15 are the main parameters for average deposition rate.

Table 4.15 Parameters affecting deposition rate by JMP

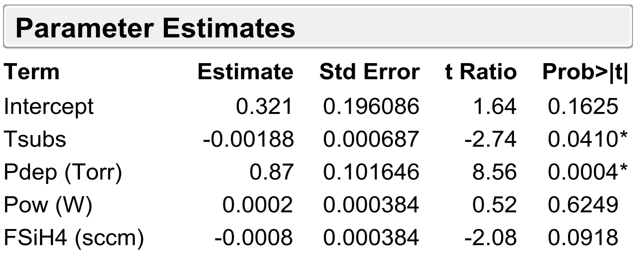

Parameter Estimates

Term	Estimate	Std Error	t Ratio	Prob>|t|
Intercept	0.321	0.196086	1.64	0.1625
Tsubs	-0.00188	0.000687	-2.74	0.0410*
Pdep (Torr)	0.87	0.101646	8.56	0.0004*
Pow (W)	0.0002	0.000384	0.52	0.6249
FSiH4 (sccm)	-0.0008	0.000384	-2.08	0.0918

Applied power and deposition pressure are the main parameters for the thickness uniformity of the films as seen in Table 4.16.

Table 4.16 Parameters affecting thickness uniformity by JMP

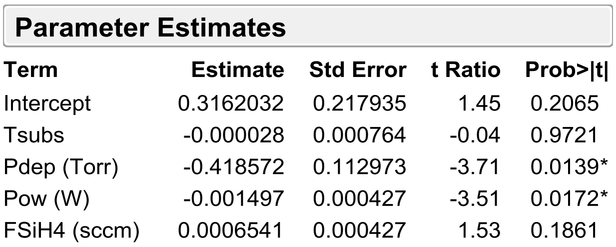

Parameter Estimates

Term	Estimate	Std Error	t Ratio	Prob>|t|
Intercept	0.3162032	0.217935	1.45	0.2065
Tsubs	-0.000028	0.000764	-0.04	0.9721
Pdep (Torr)	-0.418572	0.112973	-3.71	0.0139*
Pow (W)	-0.001497	0.000427	-3.51	0.0172*
FSiH4 (sccm)	0.0006541	0.000427	1.53	0.1861

Hydrogen content of the films were only affected by applied power as seen in Table 4.17.

Table 4.17 Parameters affecting hydrogen content by JMP

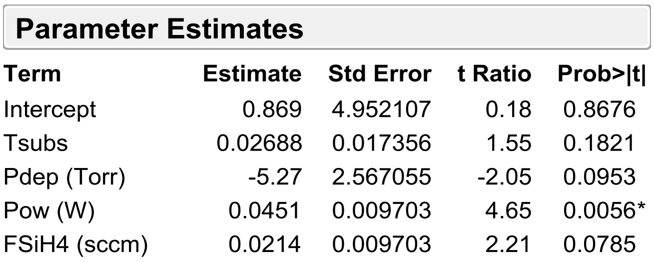

Parameter Estimates

Term	Estimate	Std Error	t Ratio	Prob>|t|
Intercept	0.869	4.952107	0.18	0.8676
Tsubs	0.02688	0.017356	1.55	0.1821
Pdep (Torr)	-5.27	2.567055	-2.05	0.0953
Pow (W)	0.0451	0.009703	4.65	0.0056*
FSiH4 (sccm)	0.0214	0.009703	2.21	0.0785

According to these results, average deposition rate, uniformity and hydrogen content are related in terms of process parameters. So any change in process parameters will affect three of them. Therefore, they should be considered together. The prediction profiler given by JMP can be seen in Figure 4.14.

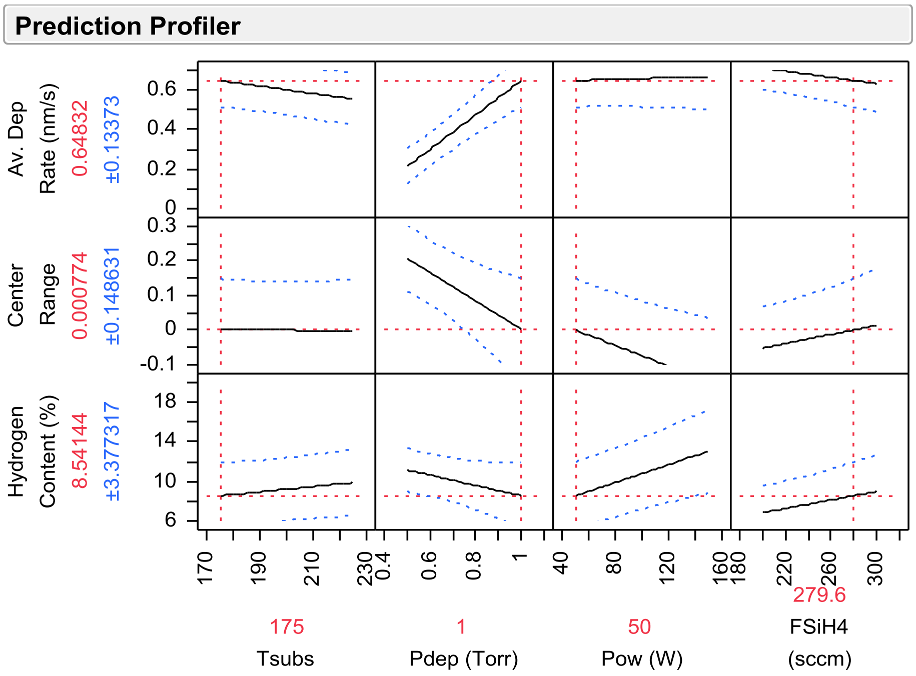

Fig. 4.14 Prediction profiler by JMP

In the x-axis, the process parameters are listed. In the y-axis film properties are listed. The black lines in the plots are the models. The dashed blue lines below and above the model lines are the standard deviation lines. The red lines are the prediction lines. By changing the place of the red lines, one can see what the model will give.

In Figure 4.14, temperature affects the hydrogen content in a positive way. On the other hand it affects deposition rate in the opposite way. So the red line was placed to the minimum temperature value in range, namely 175 °C. Increase in pressure were yielded in higher deposition rates, better uniformity and lower hydrogen content. Thus maximum pressure in the range was selected. Increasing power may increase the deposition rate a little but it has a negative effects on both hydrogen content and uniformity. Minimum value selection was meaningful. The effect of silane flow rate on the film properties cannot be seen separately. However, it can change the film properties a little according to the model. So, one can change the flow rate as desired.

4.2.10 Effects of Process Parameters on Band Gap

Band gap was not changing significantly as mentioned in the Results part of this report. Also, as seen in Table 4.18, JMP results showed that band gap was independent of the process parameters for the conducted matrix.

Table 4.18 Parameters affecting band gap by JMP

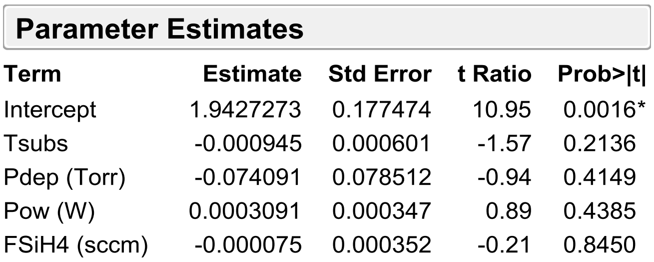

Parameter Estimates

Term	Estimate	Std Error	t Ratio	Prob>|t|
Intercept	1.9427273	0.177474	10.95	0.0016*
Tsubs	-0.000945	0.000601	-1.57	0.2136
Pdep (Torr)	-0.074091	0.078512	-0.94	0.4149
Pow (W)	0.0003091	0.000347	0.89	0.4385
FSiH4 (sccm)	-0.000075	0.000352	-0.21	0.8450

4.2.11 Effects of Process Parameters on Photo-Conductivity

From the JMP results seen in Table 4.19, photo conductivity is independent of operating parameters and within expected range.

Table 4.19 Parameters affecting photo conductivity by JMP

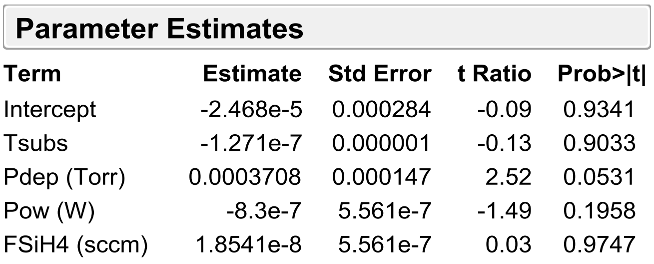

Parameter Estimates

Term	Estimate	Std Error	t Ratio	Prob>|t|
Intercept	-2.468e-5	0.000284	-0.09	0.9341
Tsubs	-1.271e-7	0.000001	-0.13	0.9033
Pdep (Torr)	0.0003708	0.000147	2.52	0.0531
Pow (W)	-8.3e-7	5.561e-7	-1.49	0.1958
FSiH4 (sccm)	1.8541e-8	5.561e-7	0.03	0.9747

4.2.12 Effects of Process Parameters on Atomic Emission Lines and Average Deposition Rate

As mentioned earlier, average deposition rate was affected by deposition pressure and substrate temperature.

SiH / H_α ratio is dependent on deposition pressure and applied power as seen in Table 4.20.

Table 4.20 Parameters affecting SiH / H_α ratio by JMP

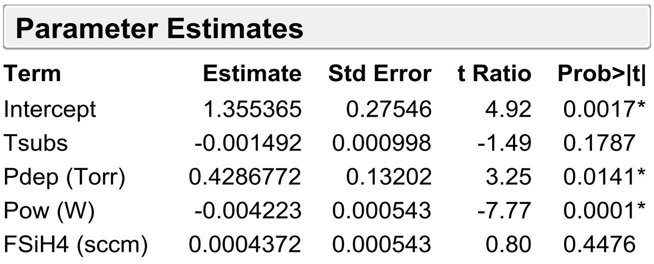

Parameter Estimates

Term	Estimate	Std Error	t Ratio	Prob>|t|
Intercept	1.355365	0.27546	4.92	0.0017*
Tsubs	-0.001492	0.000998	-1.49	0.1787
Pdep (Torr)	0.4286772	0.13202	3.25	0.0141*
Pow (W)	-0.004223	0.000543	-7.77	0.0001*
FSiH4 (sccm)	0.0004372	0.000543	0.80	0.4476

SiH / H_β ratio is dependent on parameters as seen in Table 4.21.

Table 4.21 Parameters affecting SiH / H_β ratio by JMP

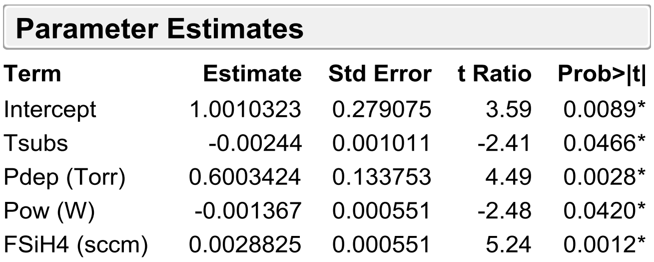

Parameter Estimates

Term	Estimate	Std Error	t Ratio	Prob>|t|
Intercept	1.0010323	0.279075	3.59	0.0089*
Tsubs	-0.00244	0.001011	-2.41	0.0466*
Pdep (Torr)	0.6003424	0.133753	4.49	0.0028*
Pow (W)	-0.001367	0.000551	-2.48	0.0420*
FSiH4 (sccm)	0.0028825	0.000551	5.24	0.0012*

In Figure 4.15 prediction of SiH / H ratios and average deposition rate with respect to process parameters can be seen.

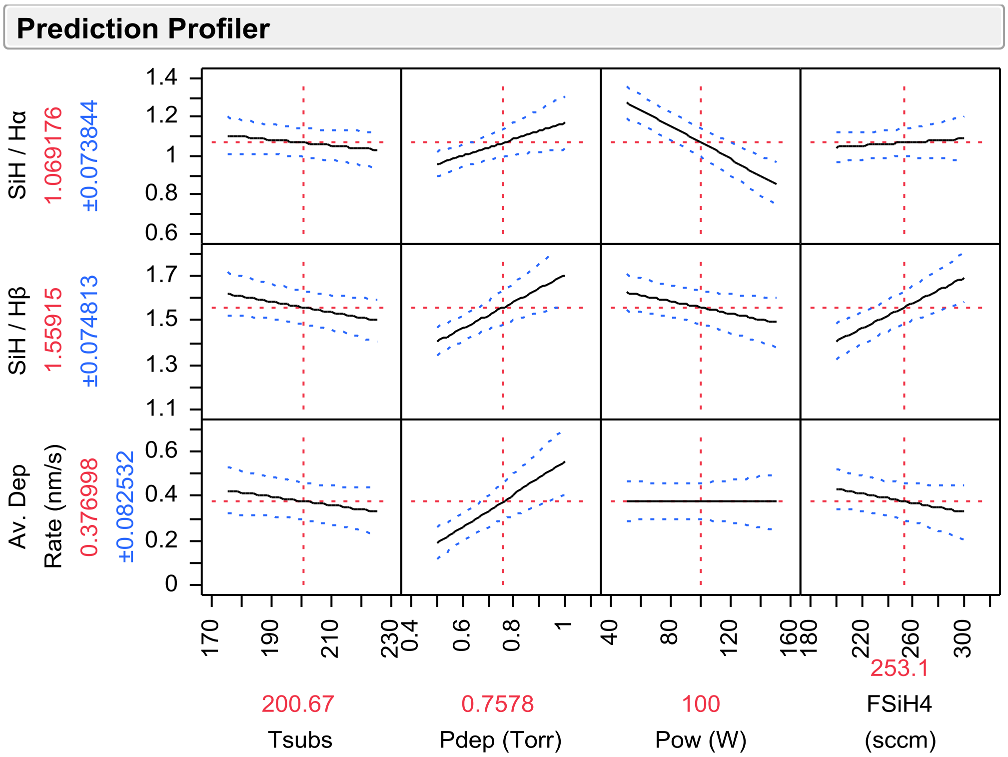

Fig. 4.15 Prediction profiler by JMP

Temperature did not affect the SiH / H_α ratio whereas SiH / H_β ratio decreased with increasing substrate temperature. It means that the number of H_β radicals dominated the chamber. Since the average deposition rate decreases with temperature and the more H_β radicals, it may be due to the higher etching rate of hydrogen.

Both of the SiH / H ratios were affected by deposition pressure positively. Increasing the deposition pressure actually means that more silane (SiH_4) and hydrogen molecules are available in the chamber. Since bond dissociation of Si-H (75 kcal/mol) is lower than H-H (104.2 kcal/mol) [37], SiH ratio in plasma may increase. As a result, increase in SiH radicals in plasma medium, increases the deposition rate.

Increasing the power applied to the plasma yielded in lower SiH / H ratios. Increasing the power increases the depletion rate of silane. However, depletion of silane did not have any effects on the deposition rate. One could expect higher deposition rates but with increasing power, the energy of the hydrogen radicals may increase that will end up with a higher etching rate.

Increasing the flow rate while keeping the pressure constant means the residence time of the molecules in the chamber gets lower. Flow rate did not have a significant effect on SiH / H_α ratio or deposition rate. However, SiH / H_β ratio reduced, which implies H_β emission was lower for this parameter. Since H_β emission needs more energy than the H_α emission and the residence times of the molecules are lowered, H_β emission might not have the time to take place.

4.2.13 Profilometer vs. Ellipsometer

Results obtained from profilometer and ellipsometer can be seen in Table 4.9. In Figure 4.16, they were plotted against each other. The slope of this plot is nearly one and the intercept is -10 nm. So the ellipsometer results will be 10 nm higher than the profilometer results. However, glass substrate was used for ellipsometer measurements and silicon wafers were used for profilometer measurements.

Moreover the tolerance of profilometer is higher than 10 nm. So the thickness results by both measurements are nearly perfectly matching.

For future studies ellipsometer will be used at multiple locations for better uniformity mapping.

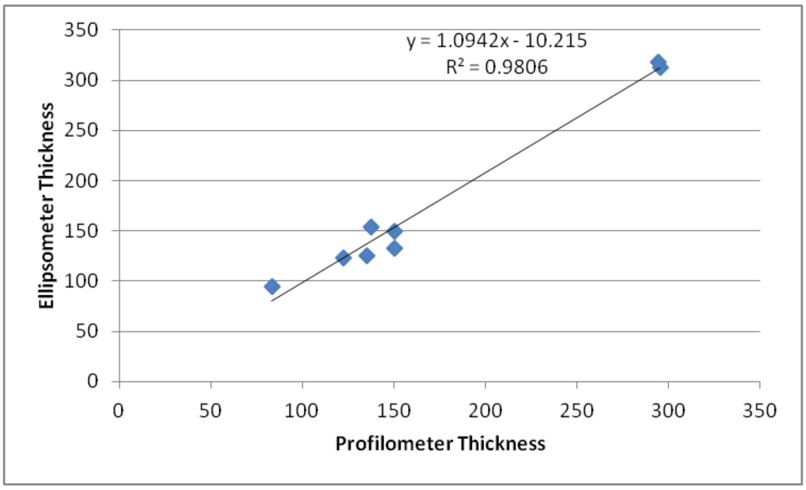

Fig. 4.16 Profilometer vs. ellipsometer

4.2.14 Phase Transition Studies

Previously, phase transition of amorphous silicon (a-Si) to microcrystalline silicon (μc-Si) was observed at high deposition powers and high pressures in CCP chamber. However, the thickness uniformity of the films were unacceptable. Phase transition was also observed in ICP chamber at very high powers (2.5 to 3 kW), but the ICP deposited films have some unexpected properties [38]. This transition at our deposition conditions, namely low powers and intermediate pressures were missing up to this point.

In order to observe the phase transition of a-Si to μc-Si, the experiments tabulated in Table 4.22 were conducted. Power, deposition pressure and substrate temperatures were fixed for all of the experiments. Hydrogen dilution was changed during experiments. Ratio (R) is defined as silane flow rate to the total flow rate. Transition was observed from Raman spectra as seen in Figure 4.17.

Table 4.22 Transition experiments' parameters and results

sample	Power (W)	Pressure (Torr)	T (°C)	F_{SiH4} (sccm)	F_{H2} (sccm)	Ratio (%)	Deprate (nm/s)	X_C (%)
ref	50	1	200	300		10	0.29	0
c4				200	100	6.7	0.19	0
c5				150	150	5	0.14	0
c6				100	200	3.3	0.10	15
c7				50	250	1.7	0.05	70
c8				120	180	4	peeled	0
c9				75	225	2.5	0.08	36

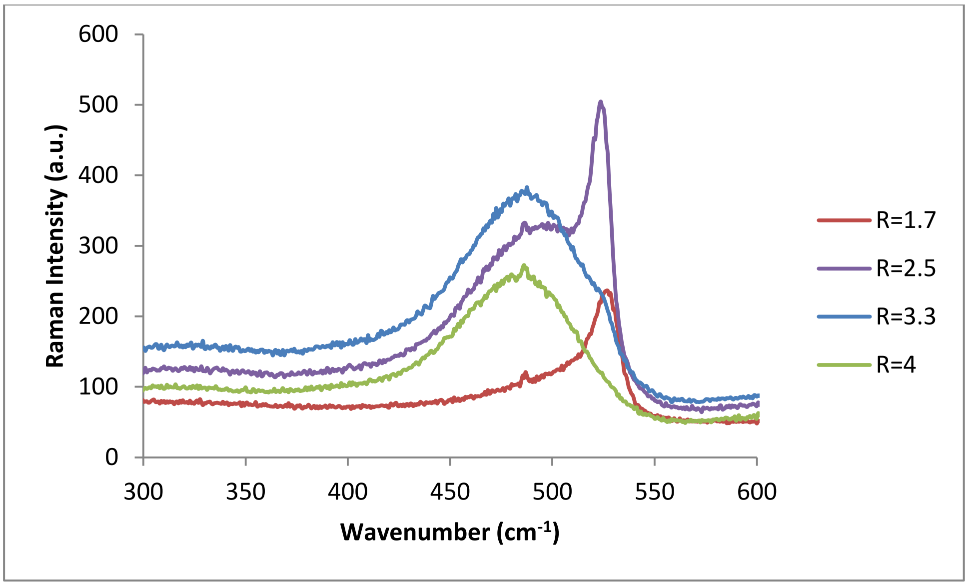

Fig. 4.17 Raman spectra of phase transition with respect to silane ratio

It is clearly seen from Figure 4.17, as hydrogen dilution increases, or in other words silane ratio (R) decreases, Raman crystallinity increases rapidly for this deposition range. In order to quantify the crystallinity, Raman spectrum should be deconvoluted as done in Figure 4.18 below.

The crystalline volume fraction (X_c) of Si can be defined by the integrated area ratio as done elsewhere [39,40]:

$$X_c = \frac{I_{520} + I_{510}}{I_{480} + I_{510} + I_{520}} \qquad \text{Eqn. (4.9)}$$

where I_{480} ,I_{510} and I_{520} are the integrated areas of the amorphous phase, intermediate phase and crystalline phase, respectively.

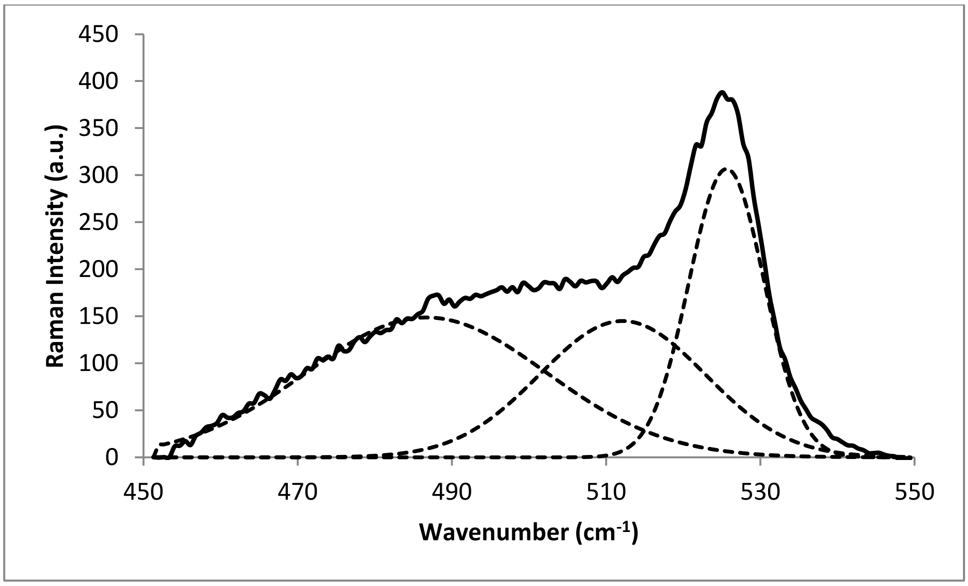

Fig. 4.18 Deconvoluted Raman spectrum of c9 coded experiment (R=2.5)

In Figure 4.19 below, crystalline volume fraction was plotted with respect to silane content (R). It was observed that exceeding 4% leads to no crystal formation. On the other hand, lowering R gave rise to crystal formation, tremendously. For the prediction of the intermediate hydrogen dilution, a polynomial was fitted and shown in the same plot.

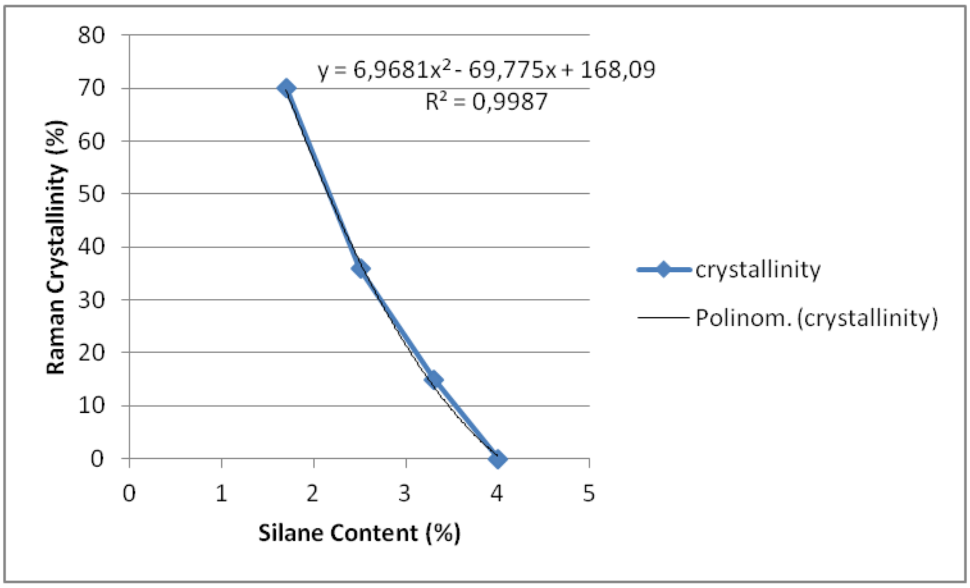

Fig. 4.19 Raman crystallinity with respect to silane content

The relation between deposition rates and crystallinity can be seen in Figure 4.20. As the crystal content increases, deposition rate decreases linearly at constant total flow rates. Moreover, crystalline deposition rates were so low when compared to amorphous rates as expected (see Table 4.22).

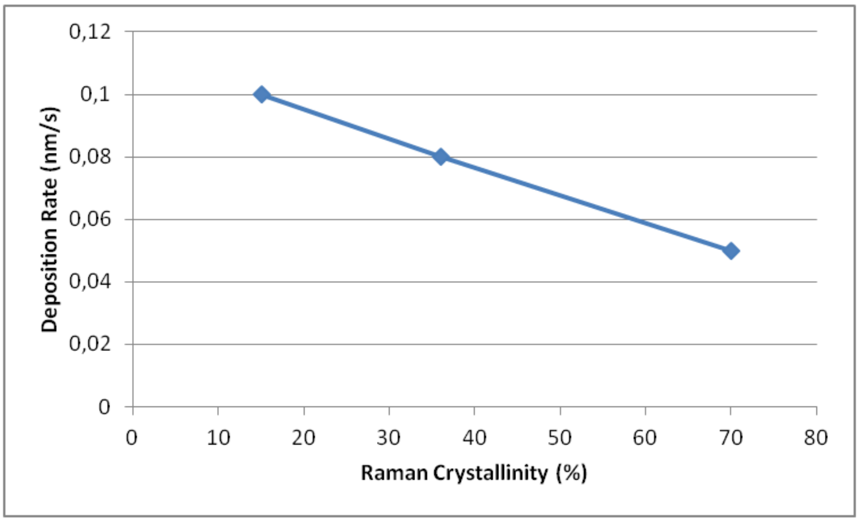

Fig. 4.20 Relation between crystal content and deposition rate

4.2.15 Conclusion

While conducting the optimization matrix, it was found that run numbers 5 and 6 yielded in best films in terms of hydrogen content, uniformity and deposition rate. The statistical analyses by JMP showed that in the optimizing range the best film will be obtained at 50 W, 1 Torr, 175 °C substrate temperature and approximately 280 sccm SiH_4 flow. Moreover, phase transition can be easily observed with increasing hydrogen dilution.

4.3 Optimization of n- and p-doped Layers

4.3.1 Design of Experiments (DOE)

The independent process parameters for PECVD process were: deposition pressure, applied power, substrate temperature, dopant to silane flow ratio and total flow rate. Among these, pressure and power were mainly affecting the thickness uniformity, as experienced in intrinsic layer optimization set. Therefore they were fixed for the p and n doping matrices.

As a first matrix, three parameters were investigated in two levels as seen in Table 4.23. In Table 4.24, DOE can be seen. After completing and analyzing these 8 experiments, the dual effects of the investigated parameters on the thickness uniformity, hydrogen contents of the films, photo and dark conductivities, band gaps were determined. For the investigation of reproducibility of the chambers, 'repeat' coded samples were deposited three times. The sample codes and deposition parameters can be easily seen in Table 4.25.

Table 4.23 Doping parameters, levels and values

Doping Parameters	Levels	Values
Pressure (Torr)	1	
Power (W)	50	
Temperature (°C)	2	175 - 225
Dopant to SiH_4 Ratio	2	0.01 - 0.05
Total Flowrate (sccm)	2	250 - 450

Table 4.24 DOE (design of experiments)

Pattern	Temperature	Dopant to Silane Ratio	Total Flowrate
Repeat	175	0.01	250
+ + +	225	0.05	450
+ − +	225	0.01	450
− − +	175	0.01	450
Repeat	175	0.01	250
+ + −	225	0.05	250
− + +	175	0.05	450
− + −	175	0.05	250
+ − −	225	0.01	250
Repeat	175	0.01	250

Table 4.25 Parameters of the experiment sets

Sample code	T_{subs} (°C)	R (N_{dopant}/N_{SiH4})	Total Flow (sccm)	Power (W)	Pressure (Torr)
n1 / p1	175	0.01	250	50	1
n1r1 / p1r1	175	0.01	250		
n1r2 / p1r2	175	0.01	250		
n2 / p2	175	0.05	250		
n3 / p3	175	0.05	450		
n4 / p4	175	0.01	450		
n5 / p5	225	0.01	250		
n6 / p6	225	0.05	250		
n7 / p7	225	0.01	450		
n8 / p8	225	0.05	450		

4.3.2 Transition Experiments

After completing the optimization matrix, conductivity transition experiments have been conducted. The well-known dark-conductivity transition figure [2] is given as Figure 4.21. In this figure, the left side is p-doping where dopant to silane ratio increases to left. Intermediate region is the intrinsic ('non-intentionally doped') region. Right part is the n-doping region, and it mirrors the dopant to silane increase trend.

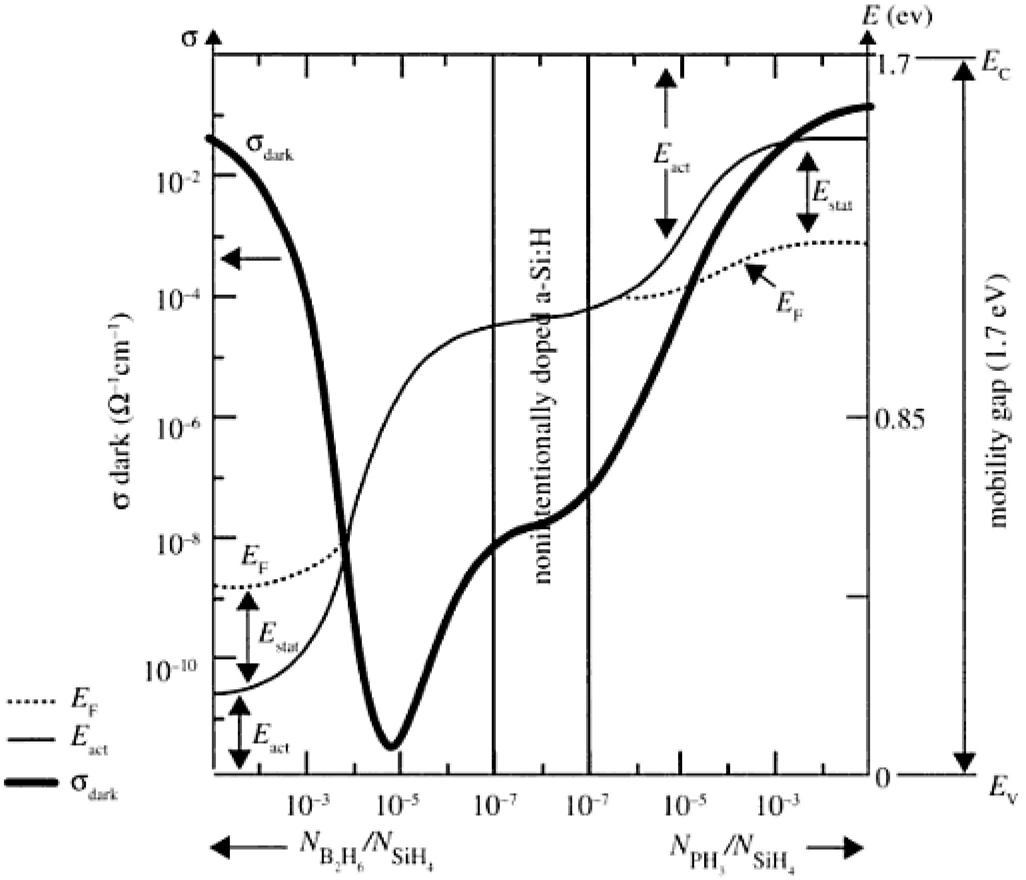

Fig. 4.21 Transition from p-doped to intrinsic and to n-doped a-Si:H

The aim of this transition set was to obtain such a figure. However, GÜNER system has a restriction to reach lower values for dopant to silane ratio because of the limitations of the mass flow controllers (MFC). MFC's cannot control flow rates lower than 10 sccm. Moreover, they have limits for maximum flows. As a result the minimum value for this ratio in GÜNER is 0.0025.

The experiment set can be seen in Table 4.26. The set was conducted for both p and n-doping. The first two runs (namely 7 & 8) were conducted for optimization set. The total flow could not be kept constant due to the mentioned MFC limitations for runs 10 & 11. Run 12 was made as the 'non-intentionally doped' sample.

Table 4.26 Transition set experiments

Code	Power (W)	Pressure (Torr)	Substrate Temperature (°C)	Ratio (N_{dopant}/N_{silane})	F_{SiH4}	F_{dopant}	F_{Total} (sccm)
7	50	1	225	0.01	428	22	450
8	50	1	225	0.05	360	90	450
9	50	1	225	0.005	439	11	450
10	50	1	225	0.003	650	10	670
11	50	1	225	0.0025	790	10	800
12	50	1	225	0	450	0	450

4.3.3 Sample Preparation

Corning glass (25x25x0.22 cm^3) was used as the substrate in these optimization sets in GÜNER system. It can be used for Raman spectroscopy, optical and conductivity measurements. Moreover, a piece of low doped silicon wafer was placed on this glass substrate for the FTIR measurements. Two one side polished silicon wafers were used to determine the film thicknesses, uniformity and the deposition rates by profilometry. Previously, three silicon samples were used. However, it was shown that ellipsometer thickness calculations gave the similar results that of profilometer. So the number of the silicon pieces were reduced for these optimization sets. The positions of the samples on glass can be seen in Figure 4.22.

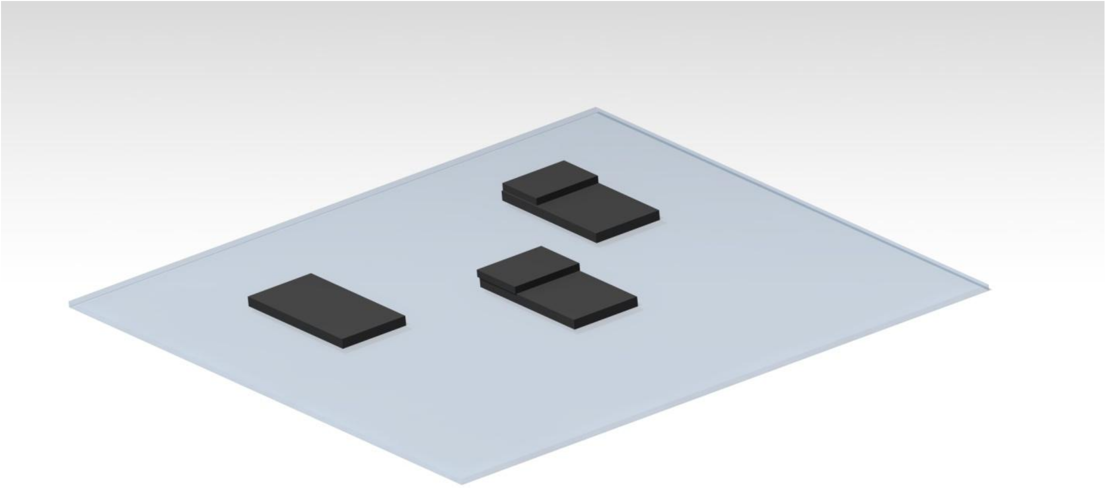

Fig. 4.22 Positions of the samples on glass substrate

4.3.4 Thicknesses and Average Deposition Rates by Profilometer and Ellipsometer

The film thicknesses and deposition rates were determined by both profilometer and ellipsometer. For the profilometry measurements, two silicon samples were used. The mapping of the thicknesses were made by taking 5 points from center to edge on the substrate by ellipsometer. So profilometer results were averaged for two values, ellipsometer were done for at least three points. The last point that is at the very edge was usually neglected for the results calculated below in Table 4.27 and 4.28.

Table 4.27 Average thicknesses and deposition rates for n-matrix

	Ellipsometer		Profilometer	
Sample code	Average Thickness (nm)	Average deposition rate (nm/s)	Average Thickness (nm)	Average deposition rate (nm/s)
n1	178.3	0.20	170	0.19
n1r1	177.0	0.20	205	0.23
n1r2	162.8	0.18	177.5	0.20
n2	148.3	0.16	105	0.12
n3	108.3	0.18	90	0.15
n4	113.5	0.19	75	0.13
n5	116.3	0.13	120	0.13
n6	133.0	0.15	130	0.14
n7	149.8	0.25	177.5	0.30
n8	120.8	0.20	130	0.22

Table 4.28 Average thicknesses and deposition rates for p-matrix

	ellipsometer		profilometer	
Sample code	Average Thickness (nm)	Average deposition rate (nm/s)	Average Thickness (nm)	Average deposition rate (nm/s)
p1	380.0	0.42	366.7	0.41
p1r1	308.5	0.34	325	0.36
p1r2	447.3	0.50	435	0.48
p2	378.8	0.42	370	0.41
p3	311.3	0.52	310	0.52
p4	193.5	0.32	220	0.37
p5	398.3	0.44	400	0.44
p6	362.3	0.40	417.5	0.46
p7	313.3	0.52	345	0.58
p8	258.3	0.43	295	0.49

First three samples were the repeating runs, which means all of the deposition parameters were the same. It is seen from Table 4.27 that the thicknesses for these repeating runs showed a reproducible trend. However, p-chamber showed an opposite trend, as seen in Table 4.28.

4.3.5 Thickness Uniformities by Ellipsometer

Five data for each sample have been modeled for each deposition. The last datum that is at the edge was neglected. The uniformity calculations were made by Equation 4.1.

The reproducibility in terms of uniformity for n-chamber was not convenient as seen in Table 4.29. On the other hand, the situation was better for p-chamber.

n5 coded sample has the uniformity of 1%, which was the best one among n-samples. The uniformities for p-chamber was observed to be lower than n-chamber, i.e. p1, p3, p5 and p6 were acceptable in terms of thickness uniformity.

Table 4.29 Uniformities for p and n-matrix

sample code	uniformity	sample code	uniformity
n1	0.06	p1	0.05
n1r1	0.10	p1r1	0.02
n1r2	0.17	p1r2	0.07
n2	0.11	p2	0.12
n3	0.11	p3	0.03
n4	0.17	p4	0.22
n5	0.01	p5	0.06
n6	0.18	p6	0.06
n7	0.11	p7	0.29
n8	0.06	p8	0.15

4.3.6 Hydrogen Content by FTIR

FTIR transmission analyses were conducted as done in section 4.2.4. A typical transmission spectrum can be seen in Figure 4.23. The vibration modes of silicon peaks are tabulated in Table 4.30.

The peak located around 2090 cm^{-1} is a measure of number of defect states in a-Si:H. As this peak arises, the number of defects increases, so does the Staebler-Wronski Effect (SWE) [41].

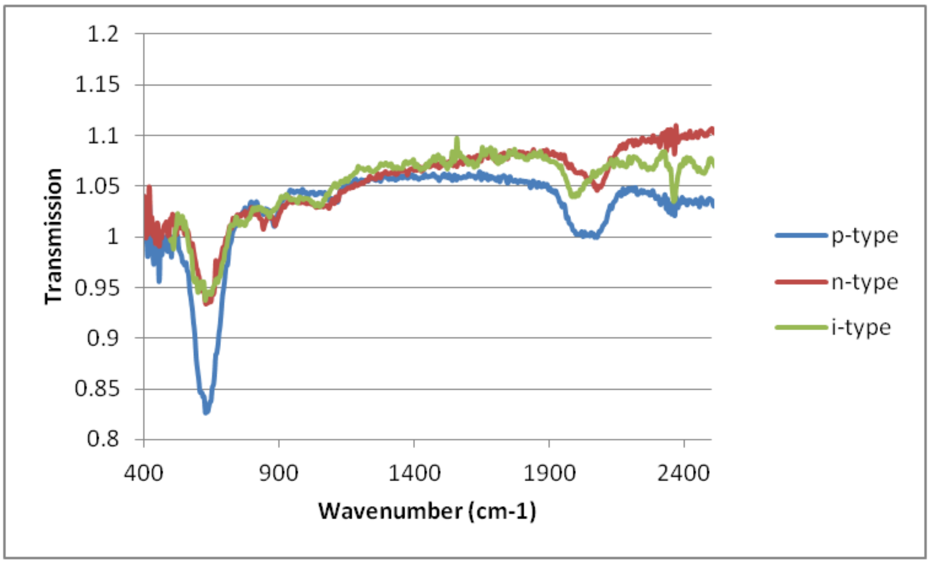

Fig. 4.23 Representative transmission spectrum of intrinsic and doped a-Si:H thin films

Table 4.30 Vibration modes of a-Si:H [42]

Wavenumber (cm^{-1})	Mode
640	Si-Si bending
2000	Si-H stretching
2090	Si-H_2 or Si-H_3 stretching
1080	Si-O

Calculated hydrogen contents for the both n and p matrices were given in Table 4.31 and 4.32, respectively. Most of the n-type films and all of the p-type films were satisfactory according to the literature [2]. Moreover, the reproducibility of the films for both n and p-type were acceptable.

Table 4.31 Hydrogen content of the n-type films

Sample code	T_{subs} (^oC)	R (N_{PH3}/N_{SiH4})	Total flow (sccm)	C_H (%)
n1	175	0.01	250	8.2
n1r1	175	0.01	250	8.56
n1r2	175	0.01	250	9.21
n2	175	0.05	250	13.4
n3	175	0.05	450	12.64
n4	175	0.01	450	20.62
n5	225	0.01	250	10.58
n6	225	0.05	250	12.62
n7	225	0.01	450	7.89
n8	225	0.05	450	7.51

The best quality plasma grown a-Si:H films have less than 10% hydrogen content. If hydrogen concentration exceeds 25%, hydrogen-related voids in the film occurs [2].

Table 4.32 Hydrogen content of the p-type films

Sample code	T_{subs} (^{o}C)	R (N_{PH3}/N_{SiH4})	Total flow (sccm)	C_H (%)
p1	175	0.01	250	8.38
p1r1	175	0.01	250	10.8
p1r2	175	0.01	250	8.75
p2	175	0.05	250	7.46
p3	175	0.05	450	8.36
p4	175	0.01	450	11.89
p5	225	0.01	250	6.9
p6	225	0.05	250	5.22
p7	225	0.01	450	6.85
p8	225	0.05	450	4.42

4.3.7 Conductivity Measurements

Conductivity measurements for all amorphous silicon films have been made as explained in Section 4.2.5.

The same formula was also used for the dark conductivity measurements. The calculated conductivities for both n and p-type films were tabulated in Table 4.33 and 4.34, respectively. The results are similar to the literature [2]. However, reproducibility of n-type films were problematic, whereas p-type results were acceptable.

Table 4.33 Dark and photo-conductivities of the n-type films

	σ- dark (1/ohm.cm)	**σ- photo (1/ohm.cm)**
n1	2.76E-05	4.88E-05
n1r1	3.46E-03	4.02E-03
n1r2	5.05E-05	7.74E-05
n2	7.01E-05	1.04E-04
n3	8.60E-05	1.40E-04
n4	5.68E-05	1.02E-04
n5	4.36E-02	4.74E-02
n6	1.90E-03	2.42E-03
n7	4.51E-03	5.32E-03
n8	2.58E-03	3.35E-03

Table 4.34 Dark and photo-conductivities of the p-type films

	σ- dark (1/ohm.cm)	**σ- photo (1/ohm.cm)**
p1	5.47E-05	8.37E-05
p1r1	1.20E-05	3.13E-05
p1r2	1.59E-05	3.52E-05
p2	3.40E-05	4.43E-05
p3	5.67E-05	6.87E-05
p4	3.40E-05	8.55E-05
p5	7.39E-05	1.48E-04
p6	3.27E-04	3.76E-04
p7	3.27E-05	7.13E-05
p8	8.31E-04	9.31E-04

4.3.8 Band Gap by Ellipsometer

The model used in ellipsometry also gives band gap of the films. For each film, five different band gaps were mapped through the substrate. The averaged results were tabulated below. It can be seen that the band gaps of the material did not change so much in this parameter range. It was also seen from the repeating runs that n-chamber is more reproducible when compared to p-chamber in terms of band gaps.

Table 4.35 Band gaps by ellipsometry

sample code	band gap	sample code	band gap
n1	1.71	p1	1.62
n1r1	1.71	p1r1	1.51
n1r2	1.69	p1r2	1.63
n2	1.71	p2	1.42
n3	1.66	p3	1.48
n4	1.65	p4	1.51
n5	1.79	p5	1.45
n6	1.68	p6	1.49
n7	1.65	p7	1.64
n8	1.66	p8	1.62

4.3.9 Transition Studies

To determine the conductivities and have a calibration curve like Figure 4.21, doping sets were conducted and dark and photo-conductivities were calculated. The results were given below in Figure 4.24 and Table 4.36 for p-doped samples and in Figure 4.25 and Table 4.37 for n-doped samples. 10^{-2} to 10^{-3} (ohm cm)$^{-1}$ levels for conductivities are common in solar cell production [2]. So, now we are able to choose a desired doping level.

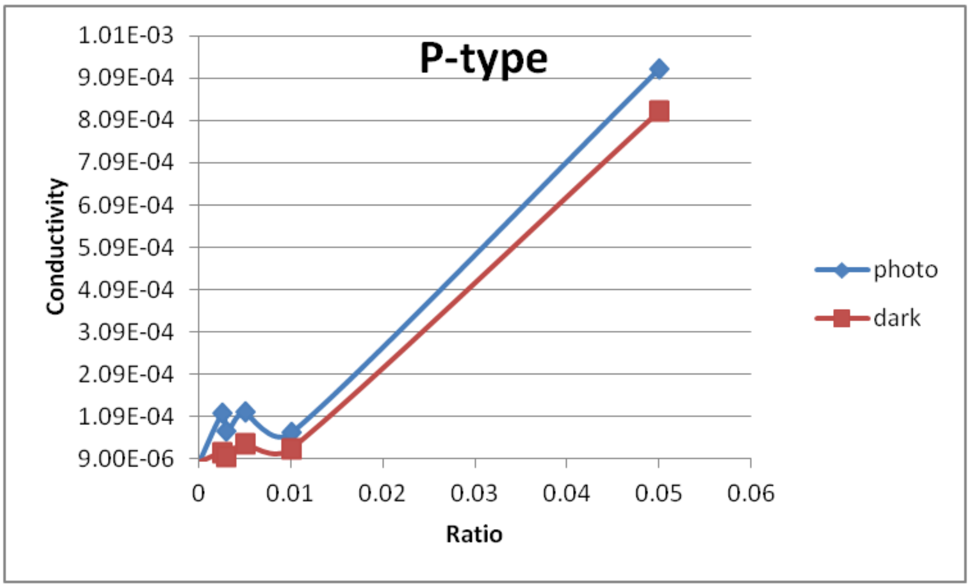

Fig. 4.24 Dark and photo-conductivities vs dopant to silane ratio for p-doped films

Table 4.36 Dark and photo-conductivities with respect to dopant to silane ratio for p-doped samples

Ratio	σ_{dark} (1/ohm.cm)	σ_{photo} (1/ohm.cm)
0	1.12E-06	3.34E-06
0.0025	2.39E-05	1.17E-04
0.003	1.31E-05	7.38E-05
0.005	4.47E-05	1.20E-04
0.01	3.27E-05	7.13E-05
0.05	8.31E-04	9.31E-04

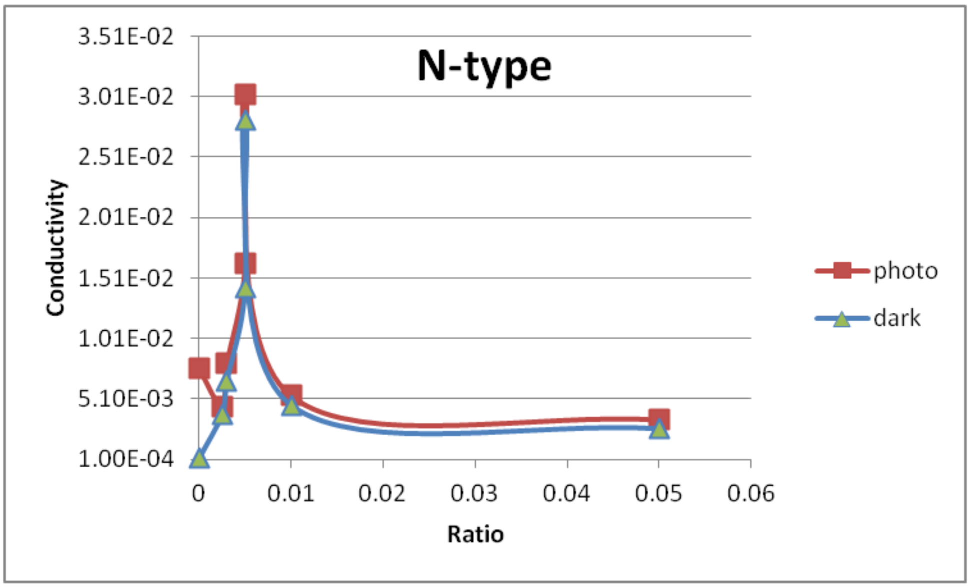

Fig. 4.25 Dark and photo-conductivities vs dopant to silane ratio for n-doped films

Table 4.37 Dark and photo-conductivities with respect to dopant to silane ratio for n-doped samples

Ratio	σ_{dark} (1/ohm.cm)	σ_{photo} (1/ohm.cm)
0	1.61E-04	7.53E-03
0.0025	3.82E-03	4.38E-03
0.003	6.54E-03	7.98E-03
0.005	1.43E-02	1.62E-02
0.005	2.81E-02	3.02E-02
0.01	4.51E-03	5.32E-03
0.05	2.58E-03	3.35E-03

4.3.10 The Effects of Process Parameters on p-type Films

After obtaining the properties of p-doped films, the effects of process parameters were investigated. For this purpose JMP program was used, which is a statistical program that uses t-test with a confidence level of 95%.

The process parameters were substrate temperature, dopant to silane flow ratio and total flow rate. Their effects on the film properties such as thickness uniformity, deposition rate, hydrogen content, band gap, dark and photo-conductivities were investigated.

In Figure 4.26, the results of the influence of process parameters on hydrogen content of the films can be seen. It is affected only by substrate temperature and dopant to silane gas ratio in a negative trend. As temperature increases, the energy at the surface might detach the hydrogen from the film.

On the other hand, for the investigated range of parameters films did not show significant differences in terms of conductivities and deposition rates (see Table 4.38).

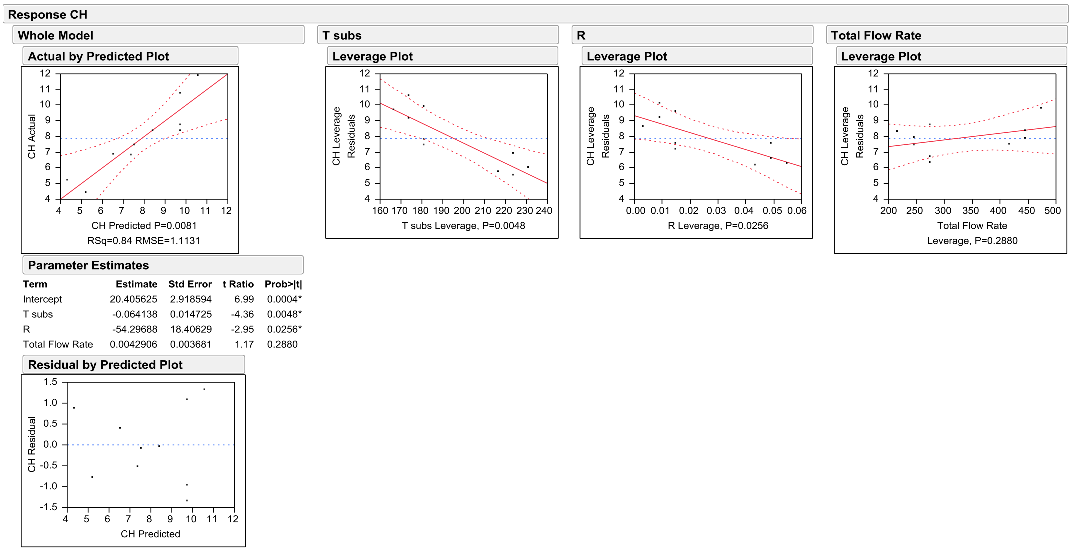

Parameter Estimates

Term	Estimate	Std Error	t Ratio	Prob>|t|
Intercept	20.405625	2.918594	6.99	0.0004*
T subs	-0.064138	0.014725	-4.36	0.0048*
R	-54.29688	18.40629	-2.95	0.0256*
Total Flow Rate	0.0042906	0.003681	1.17	0.2880

Fig. 4.26 Influence of process parameters on hydrogen contents of the p-films

Table 4.38 Significance of the process parameters on investigated p-film properties

Process Parameters	Average Dep. Rate	Uniformity	C_H	Photo Conductivity	Dark Conductivity	Band Gap
T_{subs}	0	0	+	0	0	0
R (N_{dop}/N_{silane})	0	0	+	0	0	0
Total Flow	0	0	0	0	0	0

In Figure 4.27 below, the prediction profiler can be seen. It is also used as the effect trends on films.

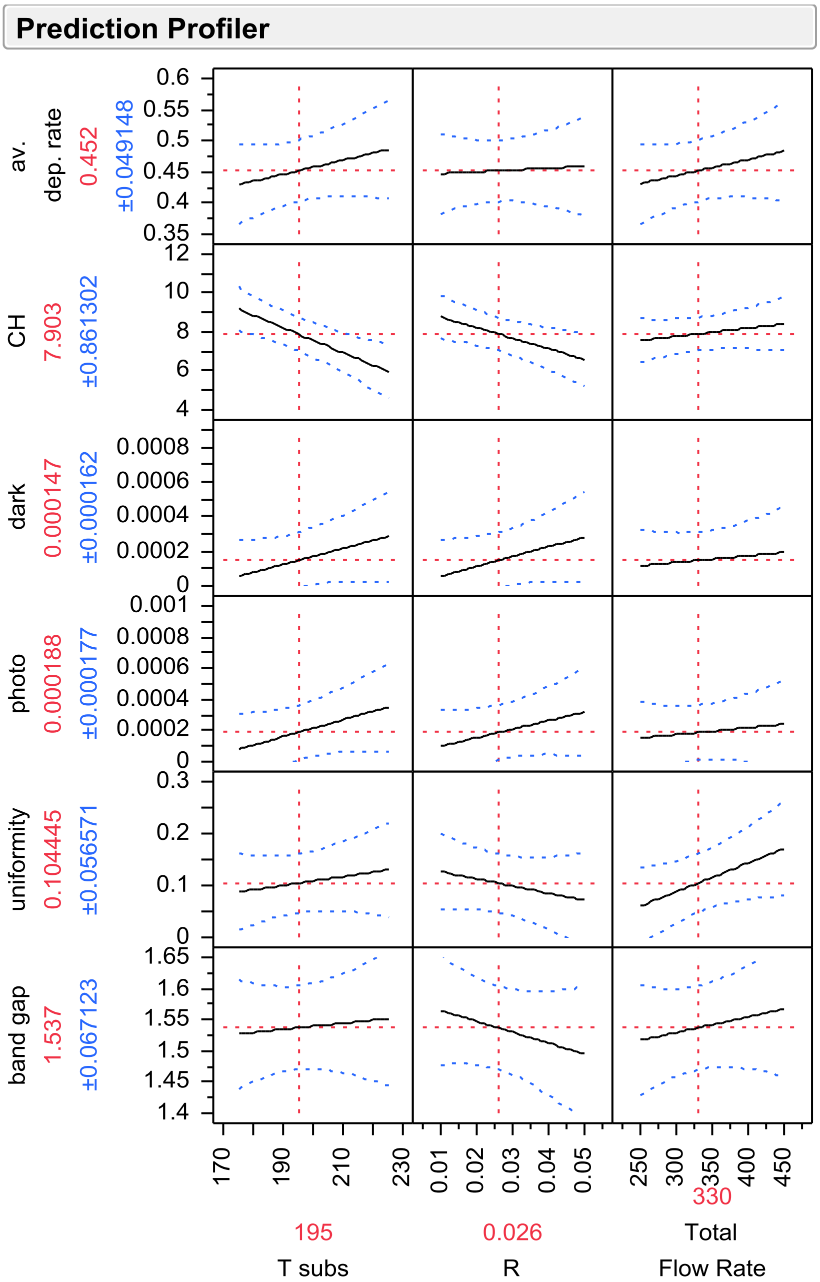

Fig. 4.27 Prediction profiler for p-films

4.3.11 The Effects of Process Parameters on n-type Films

For n-case, none of the process parameters were significantly affecting the film properties as mentioned in Table 4.39 except total flow. Total flow has a negative influence on the band gap Hydrogen content case was demonstrated in Figure 4.28. As the total flow increases, number of hydrogen molecules in the chamber increases. They might etch the weak bonds in the structure and increase the number of Si-Si bonds. So the material tends to be crystalline, and the band gap decreases.

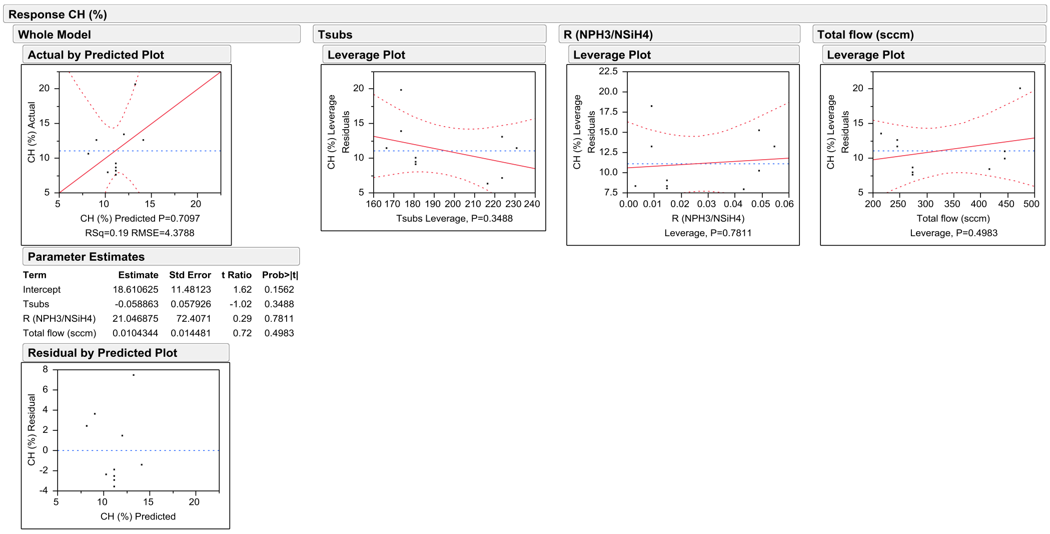

Term	Estimate	Std Error	t Ratio	Prob>|t|
Intercept	18.610625	11.48123	1.62	0.1562
Tsubs	-0.058863	0.057926	-1.02	0.3488
R (NPH3/NSiH4)	21.046875	72.4071	0.29	0.7811
Total flow (sccm)	0.0104344	0.014481	0.72	0.4983

Fig.4.28 Influence of process parameters on hydrogen contents of the n-films

Table 4.39 Significance of the process parameters on investigated n-film properties

Process Parameters	Average Dep.Rate	Uniformity	C_H	Photo Conductivity	Dark Conductivity	Band Gap
T_{subs}	0	0	0	0	0	0
R (N_{dop}/N_{silane})	0	0	0	0	0	0
Total Flow	0	0	0	0	0	+

In Figure 4.29, the prediction profiler can be seen.

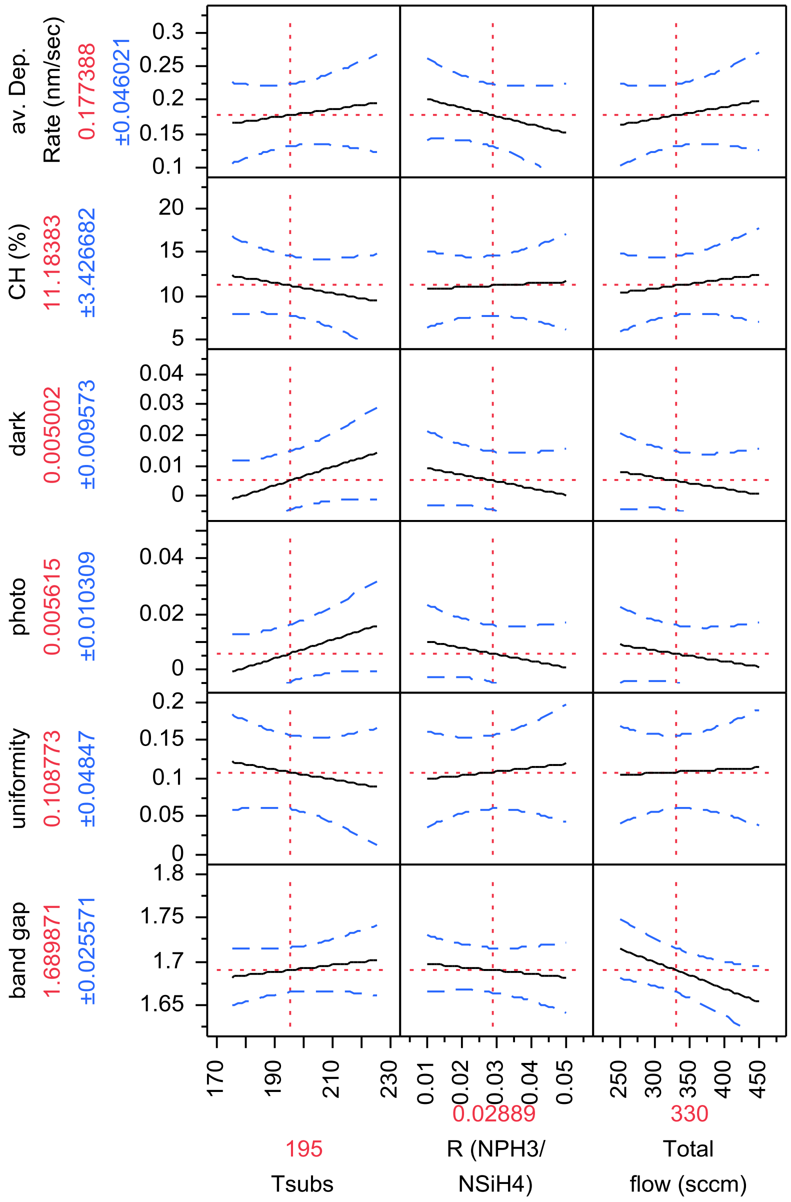

Fig. 4.29 Prediction profiler for n-films

4.3.12 Profilometer vs. Ellipsometer

Results obtained from profilometer and ellipsometer were compared in Figure 4.30 and 4.31 for n and p-type films, respectively. The results were not as good as the intrinsic optimization set, which has a slope of 1 and intercept of 10nm. The reason may be thickness non-uniformities at where the measurement was done. Also profilometer is not a proper device to measure thicknesses lower than 100 nm. As seen from Figure 4.30, after exceeding 100 nm, the results became similar. For the p-type results, which are thicker than n-type, the slope is approximately 0.9.

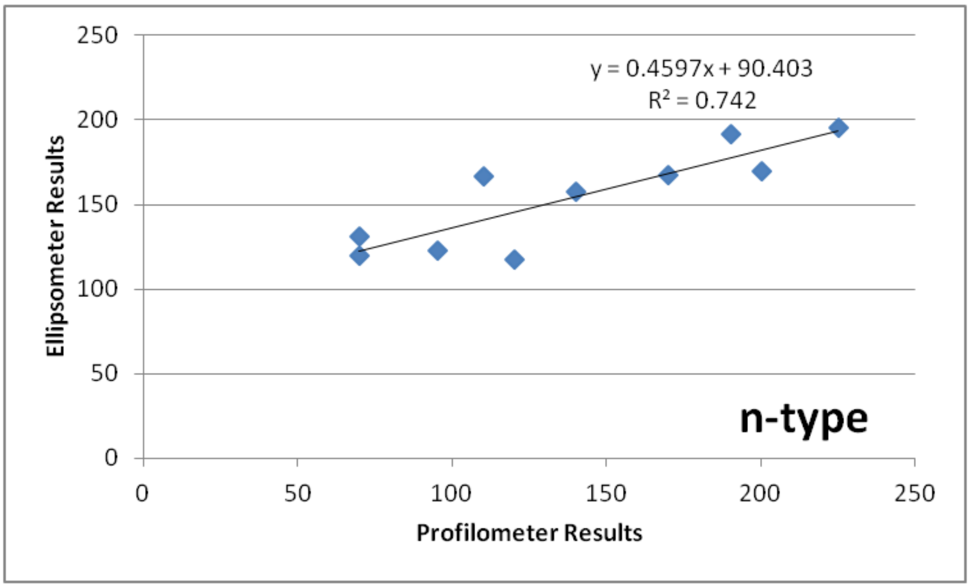

Fig. 4.30 Profilometer vs. ellipsometer for n-type

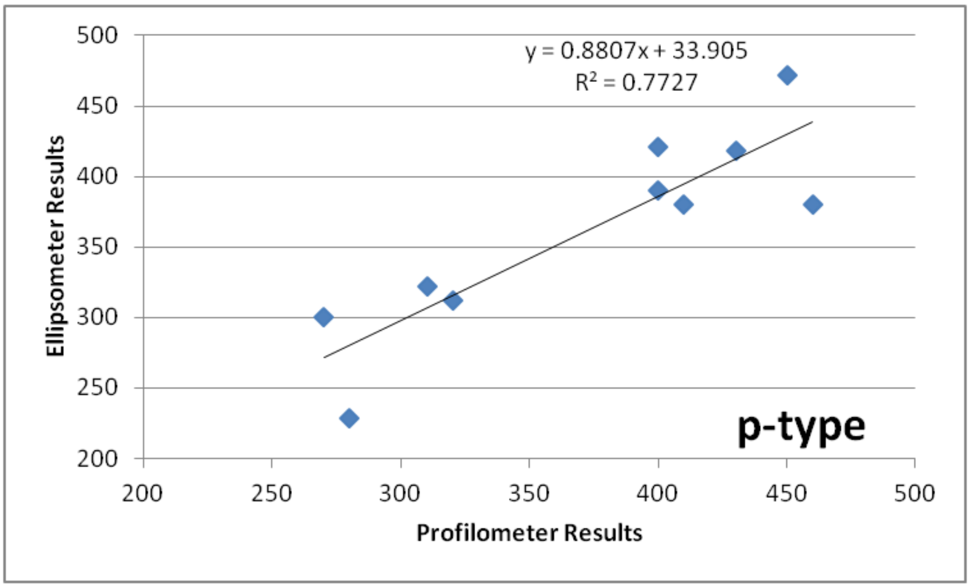

Fig. 4.31 Profilometer vs. ellipsometer for p-type

4.3.13 Conclusion

After optimization of intrinsic layer, doped layers were optimized. Most of the physical properties of the doped films were determined that will yield in the deposition of desired layers of the not only p-i-n single junction solar cell, but also HIT (hetero-junction with thin intrinsic thin layer) solar cell.

CHAPTER 5

RESULTS & DISCUSSION

5.1 p-i-n a-Si:H Type Solar cells

After completing the layer optimizations, p-i-n a-Si:H type solar cell and module production were started. However, we have to compete with a shorting problem between the contacts. The whole stack was schematically demonstrated in Figure 1.4. In thin film structure, one collects electrons from intrinsic layer, not from a wafer. Therefore, if there is any pinhole in the absorber layer or any shunt through the edges, solar cell will not work. It is crucial to deposit a continuous film on the substrate and edge isolation must be done properly.

In order to solve this shorting problem, first edge isolation of samples were verified. After to be certain of isolation, masking of the samples was decided to be the next step. Shadow masks (silicon wafers) placed on the samples were considered to be problematic, since plasma may reach under wafers. Then they were replaced with Teflon masks. However, none of these approaches lead to a solution. Then a 25 x 25 cm^2 cell was scribed into several smaller cells without using a mask by laser. Most of the cells were shorted. So it is understood that the problem was in the absorber layer. On the other hand, some of the cells did work. In Figure 5.1, the most efficient cell in that study can be seen. The production parameters for absorber layer and front and back contacts are given in tables 5.1 and 5.2, respectively. Sample has 1 x 1 cm^2 area. Solar characterizations (I-V curves) were conducted via Newport Solar Simulator under AM 1.5G illumination (90 mW/cm^2) at room temperature.

As seen from the figure, the cell has 0.74 V open circuit voltage, 5.38 mA/cm^2 short circuit current density, 34.6 % fill factor and an initial efficiency of 1.65 %. This cell is a proof that a junction and a diode formation was achieved in some parts of the 25 x 25 cm^2 substrate. However, the shorting problem for the most of the cells were not solved.

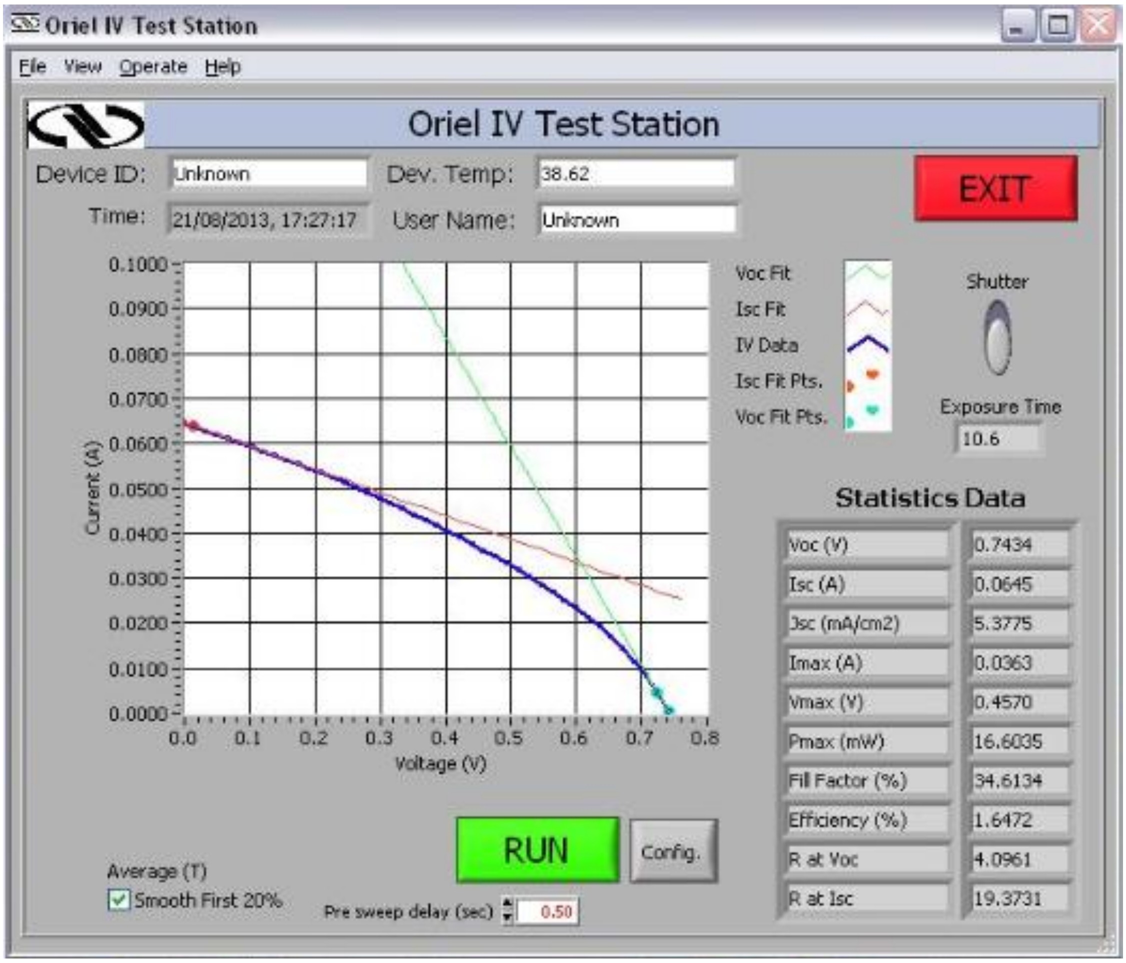

Device ID: Unknown
Dev. Temp: 38.62
Time: 21/08/2013, 17:27:17
User Name: Unknown
Exposure Time: 10.6
Average (T)
☑ Smooth First 20%
Pre sweep delay (sec) 0.50

Voc (V)	0.7434
Isc (A)	0.0645
Jsc (mA/cm2)	5.3775
Imax (A)	0.0363
Vmax (V)	0.4570
Pmax (mW)	16.6035
Fill Factor (%)	34.6134
Efficiency (%)	1.6472
R at Voc	4.0961
R at Isc	19.3731

Fig. 5.1 The first working p-i-n a-Si:H type solar cell

Table 5.1 Production parameters for the absorber layer of the first working p-i-n solar cell

a-Si:H layer	Substrate Temperature (°C)	RF Power (W)	Deposition Pressure (Torr)	Deposition Time	N_{SiH4} (sccm)	N_{B2H6} (sccm)	N_{PH3} (sccm)
p-type	175	50	1	73 s	286	14	-
Intrinsic	175	50	1	25 min	300	-	-
n-type	225	50	1	256 s	439	-	11

Table 5.2 Production parameters for the contact layers of the first working p-i-n solar cell

Layer	N_{Ar} (sccm)	Deposition Pressure (mTorr)	Substrate Temperature (°C)	RF Power (W)	# of pass
AZO (back)	125	3	50	100	4
Ag	125	3	Room T.	100	4
AZO (front)	125	3	150	600	8

It is understood that the problem occurs in the absorber layer. The shorting may be caused by pinholes, powder formation and raining on substrate from cathode or un-continuous film growth. To avoid this shorting problem;

(1) Thicker films were deposited.

(2) Instead of heating the substrate just before the deposition under gas flow, heating was done under vacuum for longer times.

(3) Residence times of the radicals in the plasma was reduced with increasing flow rates, so that the particles did not have enough time to form powder.

(4) Different power regimes were experimented.

(5) The shower head was removed to have a cross-flow regime.

However, none of those trials lead to a solution.

It was considered that the problem was occurring due to non-uniform heating of the chamber. While the anode and the substrate were heating up, the cathode was not reached the same level. Last trial was to ignite a plasma at high powers, and use it as a heat source inside the chamber. For this purpose, nitrogen plasma was ignited at 300 W for 30 minutes in the intrinsic chamber just before the deposition. This procedure was resulted in Figure 5.2. Moreover, in this production, back contact was thermally evaporated, not sputtered. The front AZO process is fixed for every solar cell deposition. The absorber layer production parameters are given in Table 5.3.

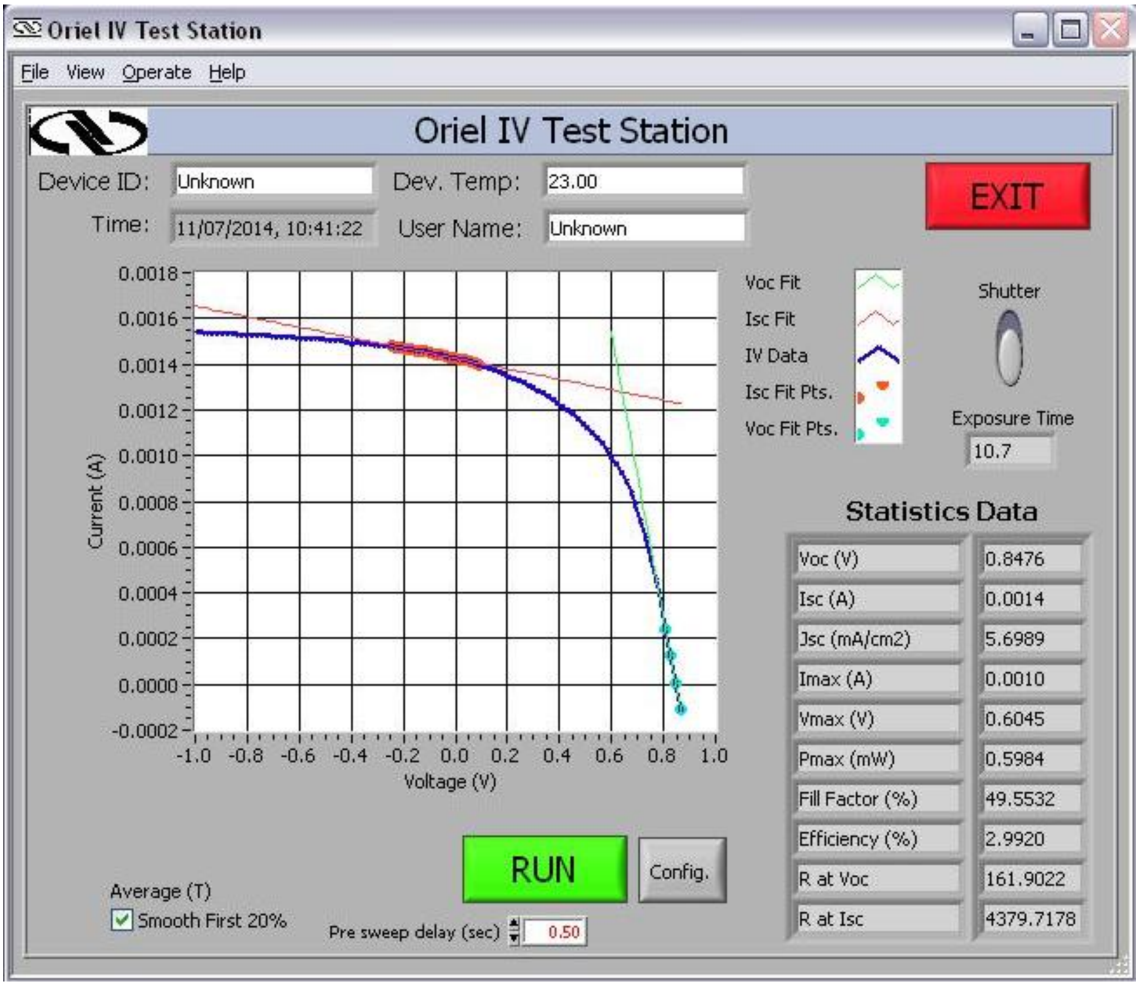

Device ID: Unknown

Time: 11/07/2014, 10:41:22

Dev. Temp: 23.00

User Name: Unknown

Exposure Time 10.7

Average (T)

☑ Smooth First 20%

Pre sweep delay (sec) 0.50

Statistics Data

Voc (V)	0.8476
Isc (A)	0.0014
Jsc (mA/cm2)	5.6989
Imax (A)	0.0010
Vmax (V)	0.6045
Pmax (mW)	0.5984
Fill Factor (%)	49.5532
Efficiency (%)	2.9920
R at Voc	161.9022
R at Isc	4379.7178

Fig. 5.2 The most efficient p-i-n a-Si:H type solar cell

Table 5.3 Production parameters for the absorber layer of the most efficient p-i-n solar cell

a-Si:H layer	Substrate Temp. (°C)	RF Power (W)	Deposition Pressure (Torr)	Deposition Time	N_{SiH4} (sccm)	N_{B2H6} (sccm)	N_{PH3} (sccm)
p-type	175	50	1	73 s	343	17	-
Intrinsic	200	50	1	20 min	350	-	-
n-type	225	50	1	256 s	439	-	11

In the Figure 5.3, the first p-i-n a-Si:H structured 25 x 25 cm^2 solar module deposited in GÜNAM, also Turkey can be seen. Although it has shorting problem, the series connection of the cells by three laser scribing processes was achieved perfectly.

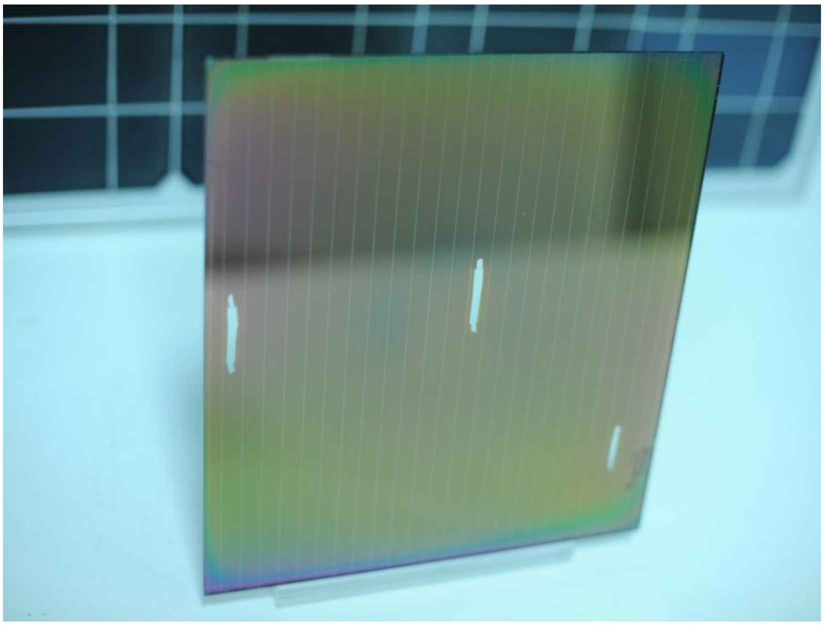

Fig. 5.3 The first 25 x 25 cm^2 p-i-n a-Si:H type solar module of Turkey

5.2 HIT Type Solar Cells

For the development of HIT solar cells, Eygi's [43] procedure was followed. The layers were optimized in sequence and then the stack was deposited. The whole stack was schematically demonstrated in Figure 1.5.

Samples have 2 x 2 cm^2 area after edge isolation and a picture is shown in Figure 5.4. Solar characterizations (I-V curves) were conducted via Newport Solar Simulator under AM 1.5G illumination (90 mW/cm^2) at room temperature.

Fig 5.4 A visual of complete heterojunction solar cell

5.2.1 Surface Texturing of c-Si Wafer

Texturing is essential to decrease the surface reflection and increase current density. Therefore, before depositing the amorphous silicon layers, the wafer was subjected to a special treatment. Chemical procedure details of texturing can be found elsewhere [44]. Surface and cross-sectional SEM images of textured c-Si wafers can be seen in figures 5.5 and 5.6, respectively.

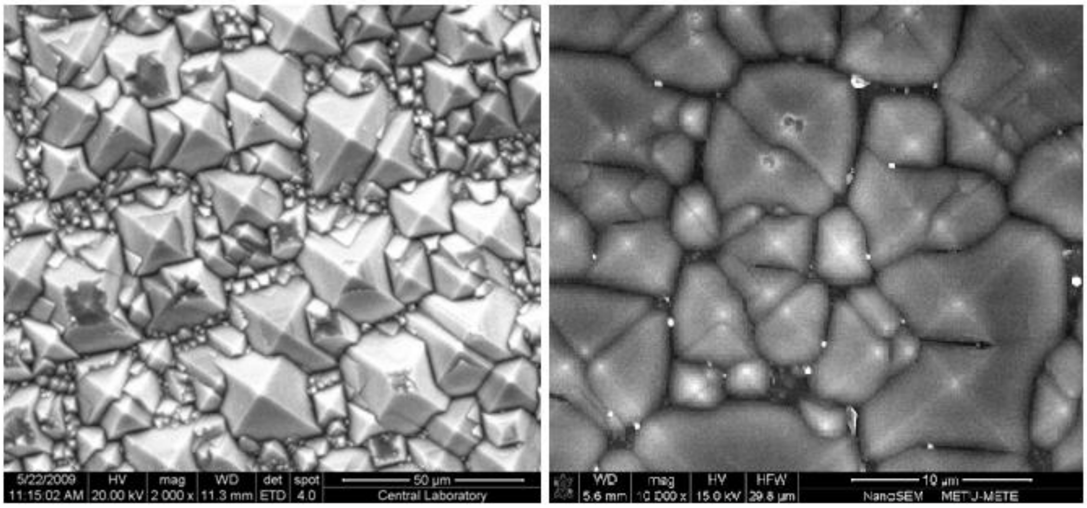

Fig. 5.5 Surface SEM image of the random textured c-Si

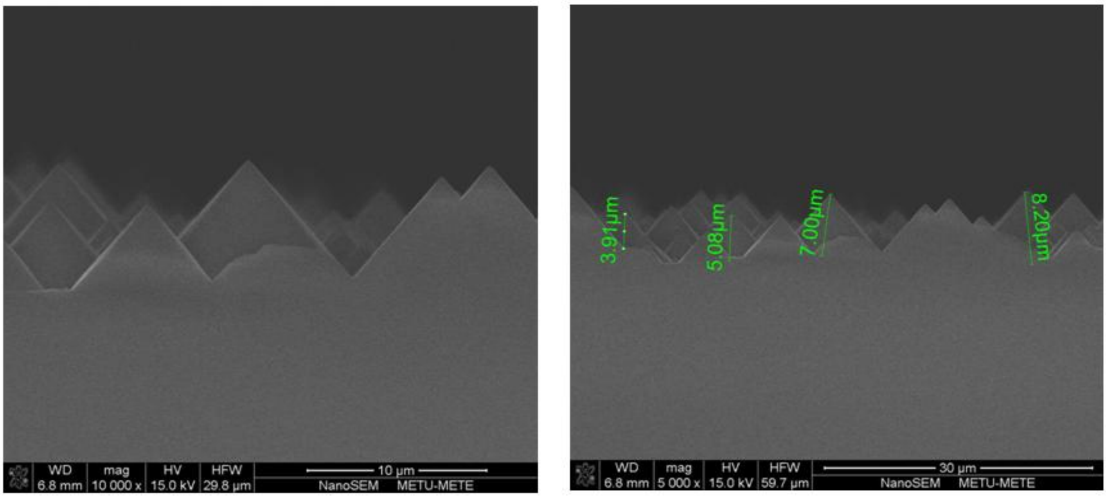

Fig. 5.6 Cross-sectional SEM image of the random textured c-Si

The optical enhancement can be seen in terms of reflectivity in Figure 5.7.

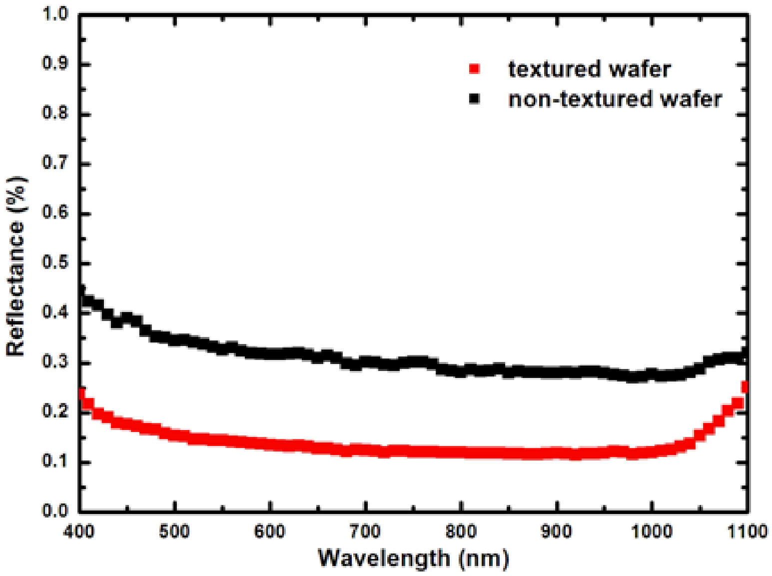

Fig. 5.7 Comparison of non-textured and the random textured c-Si wafers

5.2.2 Optimization of p-type a-Si:H Layer on n-type c-Si Wafer

Optimizations were started with depositing p-type a-Si:H on 1-5 Ω.cm resistive, 250 µm thick (100) n-type FZ (float zone) c-Si wafer. The reason to start with p-type instead of intrinsic layer was to observe the junction formation. On top of the a-Si:H layer, AZO was deposited. The sputtering properties of TCO film was kept constant in the whole thesis as; 400W applied RF power, 125 sccm Ar flow rate, 3 mTorr deposition pressure to keep the thickness constant around 80 nm. On very top and bottom, silver contacts were deposited using thermal evaporation. The resulting stack can be seen in Figure 5.8.

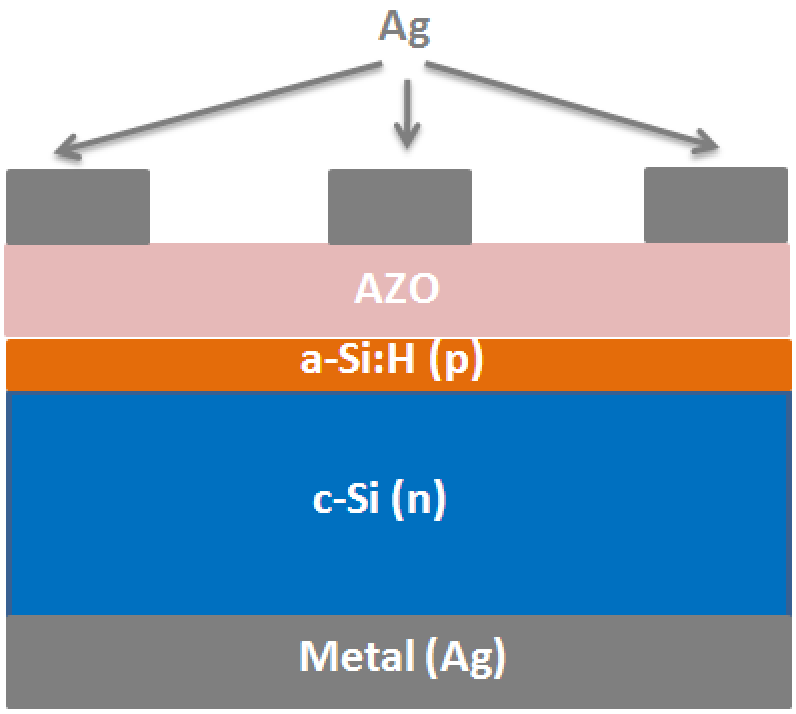

Fig. 5.8 a-Si:H (p) on c-Si (n) heterojunction

According to the 'layer optimizations' experience (see chapter 4), it was observed that the power and deposition pressure were mainly affecting the thickness uniformity. Thus, they were kept constant at 50 W and 1 Torr throughout these optimizations. The film thickness, doping ratio and substrate temperature were determined to be the tuning parameters.

5.2.2.1 Effect of p-type a-Si:H Layer Thickness

The layer thickness was the first parameter to be investigated. The optimum p-type a-Si:H thickness was reported to be 10-15 nm elsewhere [21,45,46]. However, it is not possible to measure the thickness by profilometer and ellipsometer is not reliable for this low values. Therefore the knowledge gained from previously was used. The average deposition rate for these conditions was around 0.5 nm/s. Therefore, instead of deposition rate, deposition time was used in the following Table 5.4.

Table 5.4 DOE for effect of layer thickness

Deposition Time (s)	F_{SiH4} (sccm)	F_{B2H6} (sccm)	N_{B2H6}/N_{SiH4}	Pressure (Torr)	Power (W)	Substrate Temp (ºC)
8	167	83	0.1	0.8	100	165
16	167	83	0.1	0.8	100	165
24	167	83	0.1	0.8	100	165
32	167	83	0.1	0.8	100	165

The results obtained from this DOE are presented in Table 5.5. The very first observation was that the p-n junction was formed in every sample. It was obvious that the best film was deposited at 16 seconds in terms of efficiency, fill factor and V_{oc}. Exceeding this thickness yielded in increase in the number of recombination centers and the series resistance, so the fill factor decreases.

Table 5.5 Results for different film thicknesses

Deposition Time (s)	Efficiency (%)	Fill Factor (%)	V_{oc} (V)	J_{sc} (mA/cm^2)
8	3.8	36.8	0.351	26.4
16	4.8	44.2	0.392	25.2
24	3.6	32.0	0.385	26.2
32	2.7	29.4	0.363	22.4

The following Figure 5.9, proved the same observations. The series resistance that can be understood from the slope from current side (y-axis) was very high for 8, 24, and 32 seconds of deposition. The best so the lowest slope was obtained for 16 seconds. On the other hand, from the voltage side (x-axis) one can understand the level of shunt resistance. The slope should be as high as possible. This resistance implies the current leakages through the p-layer by pinholes or non-uniformities. Therefore high shunt resistance implies better quality films.

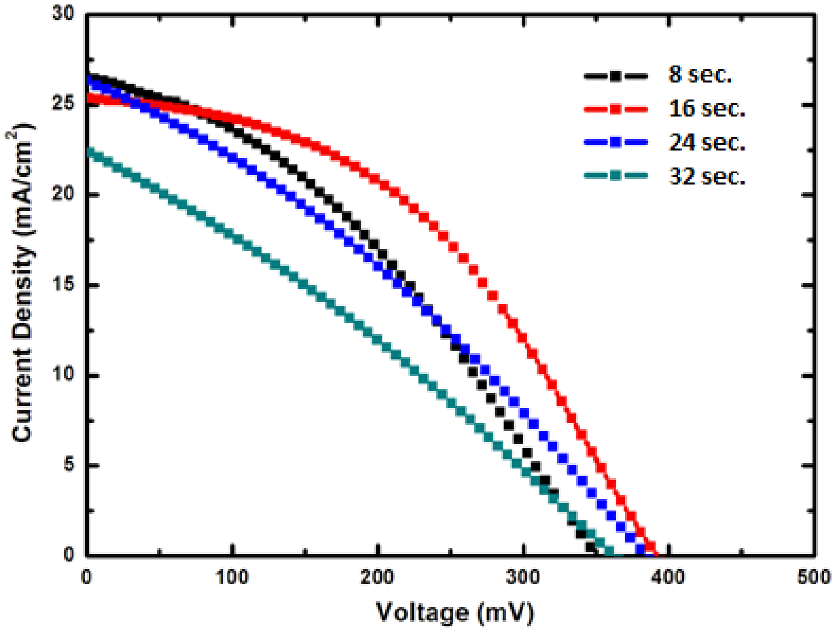

Fig. 5.9 The J-V curves for different thicknesses

5.2.2.2 Effect of p-type a-Si:H Layer Doping Ratio

The second parameter was dopant to silane (N_{B2H6}/N_{SiH4}) volumetric flow rate ratio. It was considered to be the most important parameter since the conductivity and the resistivity values differ significantly with changing this ratio as observed previously. Therefore, the following DOE was prepared as seen in Table 5.6.

Table 5.6 DOE for effect of doping ratio

Deposition time (s)	F_{SiH4} (sccm)	F_{B2H6} (sccm)	N_{B2H6}/N_{SiH4}	Pressure (Torr)	Power (W)	Substrate Temp (°C)
40	238	12	0.01	1.0	50	165
40	217	33	0.03	1.0	50	165
40	200	50	0.05	1.0	50	165
40	185	65	0.07	1.0	50	165
40	167	83	0.1	0.8	100	165

As expected, the photovoltaic properties were affected by this parameter tremendously. The V_{oc}, J_{sc} and FF were reached their highest values for R=0.07. Therefore the efficiency reached the highest value as seen in Table 5.7.

Table 5.7 Results for different doping ratios (R)

N_{B2H6}/N_{SiH4}	Efficiency (%)	Fill Factor (%)	V_{oc} (V)	J_{sc} (mA/cm^2)
0.01	0.1	24.2	0.100	3.4
0.03	4.2	41.0	0.366	25.2
0.05	6.2	48.6	0.457	25.0
0.07	7.3	51.6	0.451	28.2
0.1	4.8	44.2	0.392	25.2

The J-V curve also showed the highest current density at the lowest doping ratio as seen from Figure 5.10.

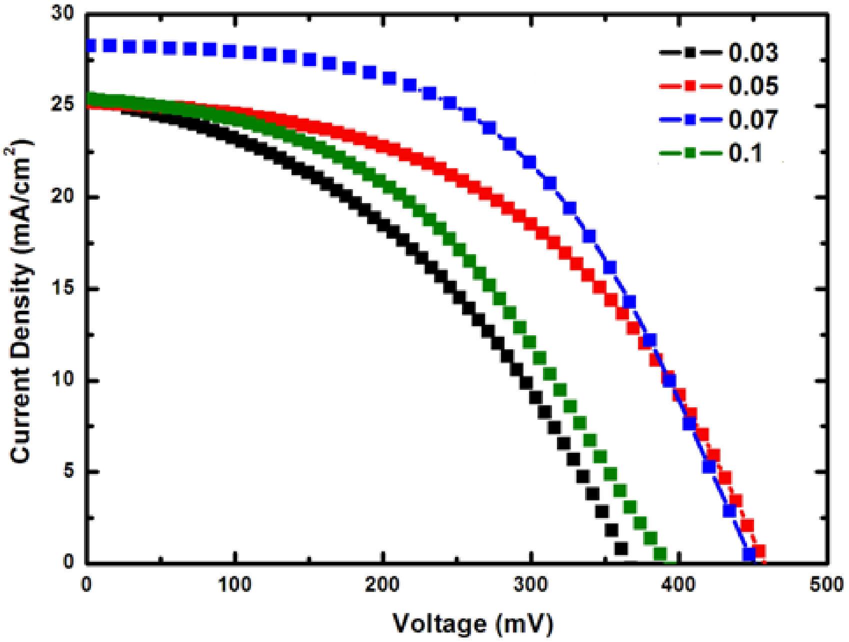

Fig. 5.10 J-V curves for different R

5.2.2.3 Effect Deposition Temperature of p-type a-Si:H Layer

Temperature is a parameter that can affect the surface mobility of the carriers in a positive manner. However, it might induce epitaxial growth at high temperatures which is not desired for heterojunctions. Therefore, substrate temperature was investigated as the third parameter. The DOE is shown in Table 5.8.

The results showed that the best film was deposited at lowest temperature. After exceeding this limit, films behaved similarly as seen in Table 5.9. Lowering the temperature more worsened the activation of dopant atoms and gave undesired results. Therefore they were excluded in this set.

Table 5.8. DOE for effect of substrate temperature

Deposition Time (s)	F_{SiH4} (sccm)	F_{B2H6} (sccm)	N_{B2H6}/N_{SiH4}	Pressure (Torr)	Power (W)	Substrate Temp (°C)
40	185	65	0.07	1.0	50	120
40	185	65	0.07	1.0	50	130
40	185	65	0.07	1.0	50	165
40	185	65	0.07	1.0	50	180

Table 5.9. Results for different substrate temperatures

Substrate Temperature (°C)	Efficiency (%)	Fill Factor (%)	V_{oc} (V)	J_{sc} (mA/cm^2)
120	7.8	54.7	0.488	26.2
130	6.4	48.9	0.450	26.4
165	6.3	48.1	0.456	25.7
180	6.8	49.4	0.470	26.2

In Figure 5.11, it is seen that the intermediate temperatures caused less quality films in terms of resistances. Although the resistances of the highest and lowest limits were quite similar, the lowest substrate temperature limit has made a better junction.

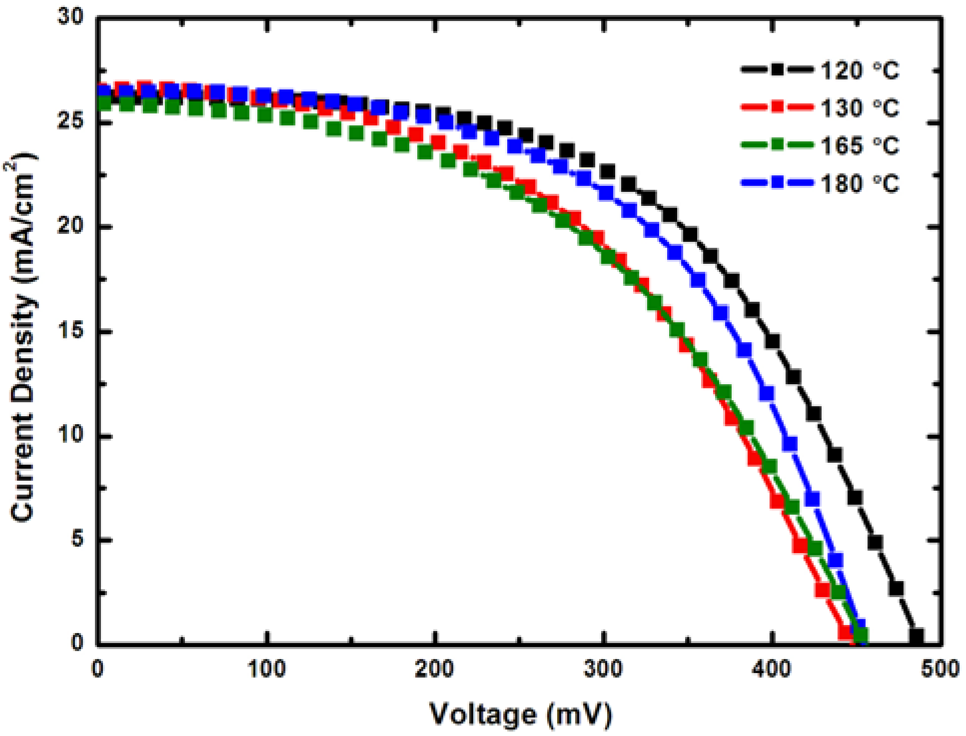

Fig. 5.11 J-V curves for different substrate temperatures

After completing the optimization, it was determined that the best process conditions for p-type a-Si:H were 16 seconds of deposition time under 50 W and 1 Torr, 0.07 dopant to silane volumetric flow rate ratio (185 sccm SiH_4, 65 sccm B_2H_6), and 120 °C substrate temperature.

5.2.3 Optimization of n-type a-Si:H Layer on p-type c-Si Wafer

Optimizations were started with depositing n-type a-Si:H on 1-5 Ω.cm resistive, 250 µm thick (100) oriented n-type FZ (float zone) and CZ (Czochralski) c-Si wafer. On top of the a-Si:H layer, AZO was deposited. The sputtering properties of TCO film was kept constant in the whole study as; 400W applied RF power, 125 sccm Ar flow rate, 3 mTorr deposition pressure to keep the thickness constant around 80 nm. On very top and bottom, silver contacts were deposited using thermal evaporation. The resulting stack can be seen in Figure 5.12.

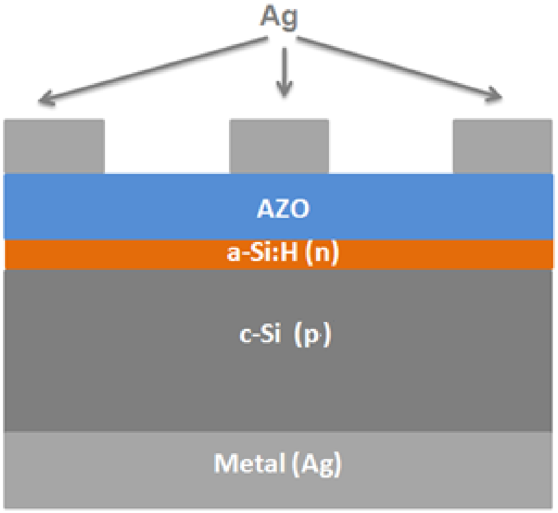

Fig. 5.12 a-Si:H (n) on c-Si (p) heterojunction

5.2.3.1 Effect of n-type a-Si:H Layer Thickness

The layer thickness was the first parameter to be investigated. The optimum n-type a-Si:H thickness was reported to be 10-15 nm elsewhere [21,45,46]. However, it is not possible to measure the thickness by profilometer and ellipsometer is not reliable for this low values. Therefore the knowledge gained from previously was used. The average deposition rate for these conditions was around 0.2 nm/s.

Therefore, instead of deposition rate, deposition time was used in the following Table 5.10.

Table 5.10 DOE for effect of layer thickness

Deposition time (s)	F_{SiH4} (sccm)	F_{PH3} (sccm)	N_{PH3}/N_{SiH4}	Pressure (Torr)	Power (W)	Substrate Temp (°C)
80	200	50	0.05	1	50	180
120	200	50	0.05	1	50	180
160	200	50	0.05	1	50	180

It was concluded from both Table 5.11 and Figure 5.13 that the thickest film deposited at 160 seconds has the best photovoltaic properties. There was a measurement error in 80 seconds.

Table 5.11 Results for different film thicknesses

Deposition time (s)	Efficiency (%)	Fill Factor (%)	V_{oc} (V)	J_{sc} (mA/cm^2)
80	8.65	56.97	0.539	25.33
120	9.27	61.75	0.528	25.60
160	9.41	60.68	0.542	25.77

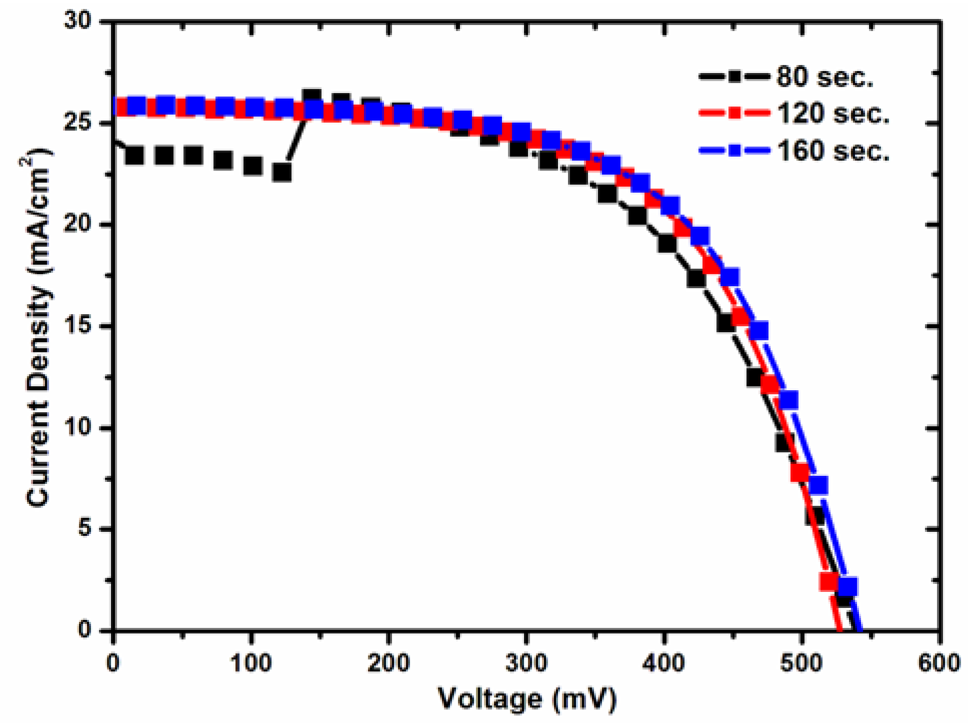

Fig. 5.13 The J-V curves for different thicknesses

5.2.3.2 Effect of n-type a-Si:H Layer Doping Ratio

Volumetric doping ratio (R) was investigated as the second parameter. Total flow rate was kept constant at 250 sccm in this set. The process parameters were tabulated below in Table 5.12.

0.05 doping ratio was found to be the best parameter as seen from Figure 5.14 and Table 5.13. There is again a measurement error in R=0.03.

Table 5.12 DOE for effect of doping ratio (R)

Deposition time (s)	F_{SiH4} (sccm)	F_{PH3} (sccm)	N_{PH3}/N_{SiH4}	Pressure (Torr)	Power (W)	Substrate Temp (ºC)
120	217	33	0.03	1.0	50	180
120	200	50	0.05	1.0	50	180

Table 5.13 Results for different doping ratio (R)

N_{PH3}/N_{SiH4}	Efficiency (%)	Fill Factor (%)	V_{oc} (V)	J_{sc} (mA/cm^2)
0.03	8.60	61.73	0.507	24.72
0.05	9.27	61.75	0.528	25.60

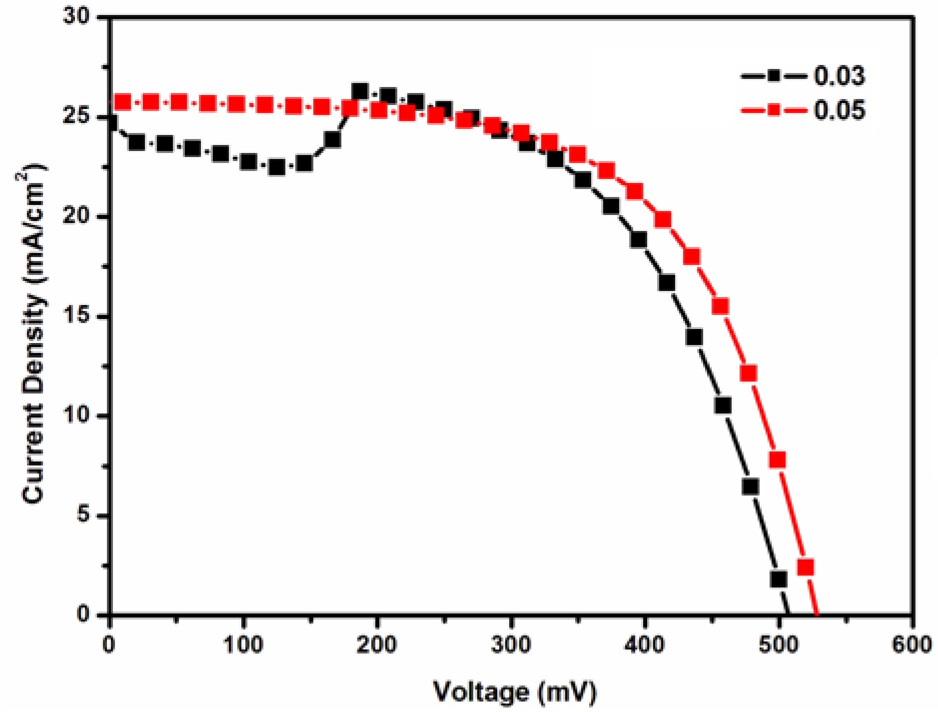

Fig. 5.14 The J-V curves for different R

5.2.3.3 Effect of n-type a-Si:H Layer Substrate Temperature

As the third parameter substrate temperature was investigated in the range of 160-200 °C. Design of experiments was presented in Table 5.14.

Table 5.14 DOE for effect of substrate temperature

Deposition time (s)	**F_{SiH4} (sccm)**	**F_{PH3} (sccm)**	**N_{PH3}/N_{SiH4}**	**Pressure (Torr)**	**Power (W)**	**Substrate Temp (°C)**
160	200	50	0.05	1.0	50	160
160	200	50	0.05	1.0	50	180
160	200	50	0.05	1.0	50	200

Results showed that n-type a-Si:H was highly affected by substrate temperature. As seen from Table 5.15 and Figure 5.15, 180 °C made an obvious peak in the photovoltaic properties.

Table 5.15 Results for different substrate temperatures

Substrate Temperature (°C)	**Efficiency (%)**	**Fill Factor (%)**	**V_{oc} (V)**	**J_{sc} (mA/cm^2)**
160	4.55	38.58	0.418	25.35
180	10.38	61.41	0.542	25.80
200	5.88	45.65	0.514	22.53

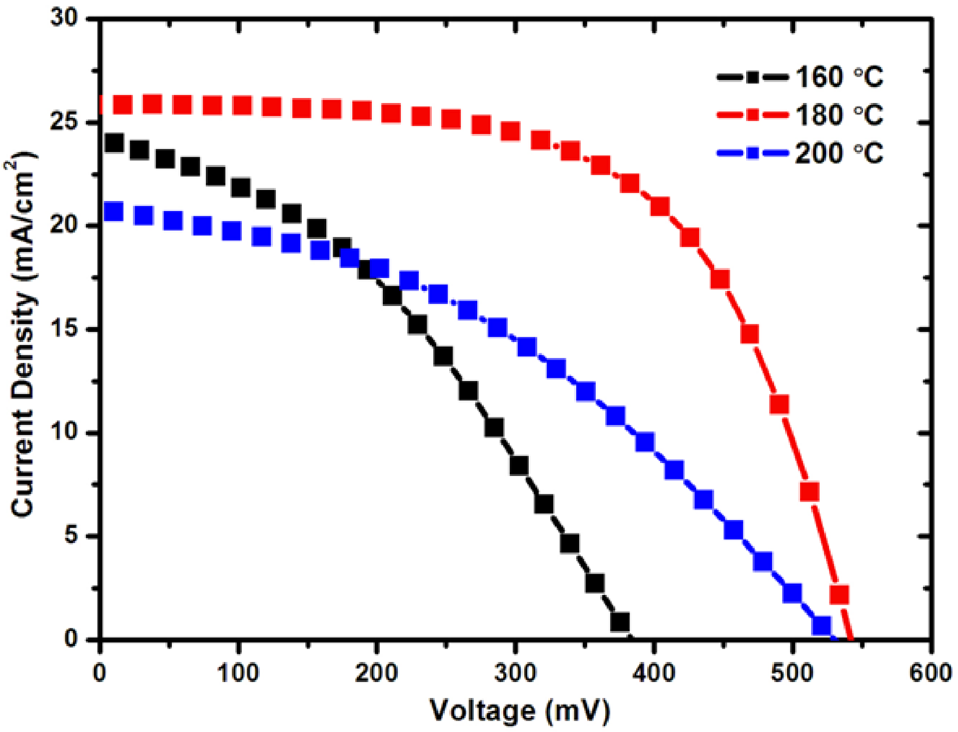

Fig. 5.15 The J-V curves at different substrate temperatures

As a result of the optimization, it was determined that the best process conditions for n-type a-Si:H were 160 seconds of deposition time under 50 W and 1 Torr, 0.05 dopant to silane volumetric flow rate ratio (200 sccm SiH_4, 50 sccm PH_3), and 180 °C substrate temperature.

5.2.4 Full Size Heterojunction without Intrinsic Layer

After determining the best parameters for n- and p-type a-Si:H layers, typical heterojunctions were produced on both p- and n-type 125 x 125 mm^2 c-Si wafers. They are schematically drawn in Figure 5.16. Their back sides were not completely covered with silver to have measurements from back-side also. Silver contacts were deposited by screen-printing.

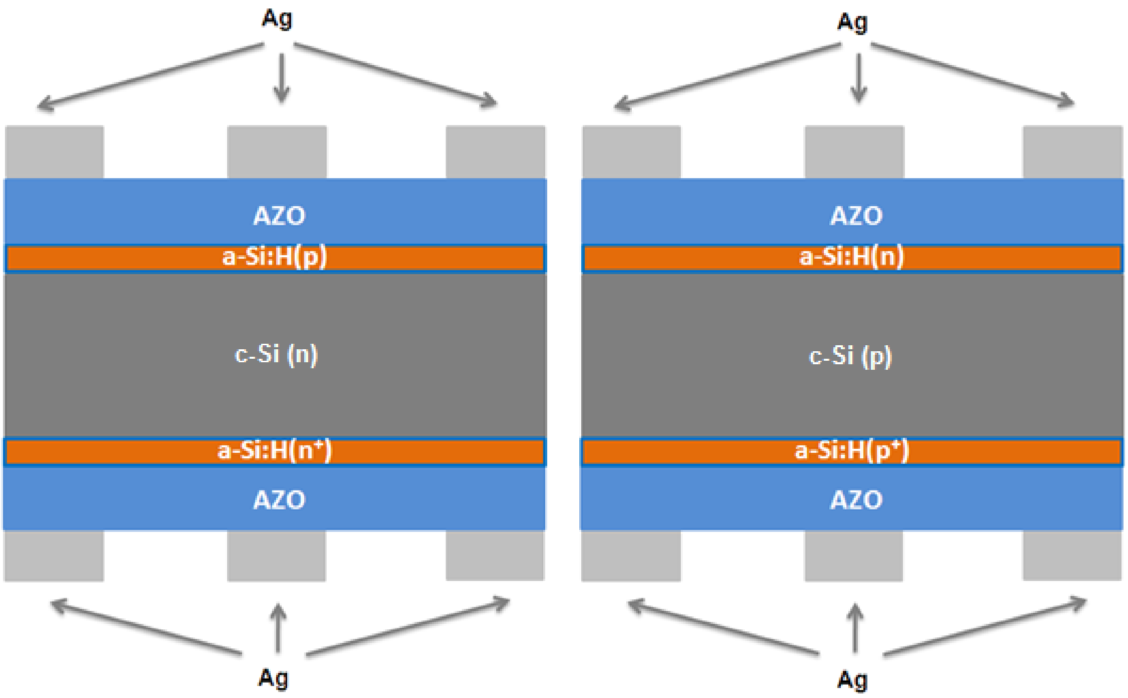

Fig. 5.16 Full size heterojunction without intrinsic a-Si:H layer

Deposition parameters according to optimizations for heterojunction on p-type c-Si 125 x 125 mm^2 wafer are given in Table 5.16.

Table 5.16 Deposition parameters for heterojunction on p-type c-Si wafer

layer	Dep. time (s)	F_{SiH4} (sccm)	F_{dopant} (sccm)	N_{dopant}/N_{SiH4}	Pressure (Torr)	Power (W)	T (ºC)
a-Si:H(n)	160	200	50	0.05	1.0	50	180
a-Si:H(p+)	40	185	65	0.07	1.0	50	120

The photovoltaic properties were given in Table 5.17 and J-V curve is plotted in Figure 5.17. When compared to un-complete (without p+) heterojunction (see Table 5.15), improvement was observed in the current density and voltage on the front side, which implies the back surface field (BSF) layer was working properly. Efficiency and fill factor losses are due to high area and high series resistance of the complete stack. Moreover, the shunt resistances were not high as expected. On the other hand, when the cell was illuminated from the back side, a serious decline in the current was observed. This might explained by the longer pathway of photon to reach the p-n junction.

Table 5.17 Photovoltaic properties for heterojunction on p-type c-Si wafer

	Efficiency (%)	Fill Factor (%)	V_{oc} (V)	J_{sc} (mA/cm^2)
Front side	8.66	49.1	0.592	29.7
Back side	6.66	59.0	0.581	19.4

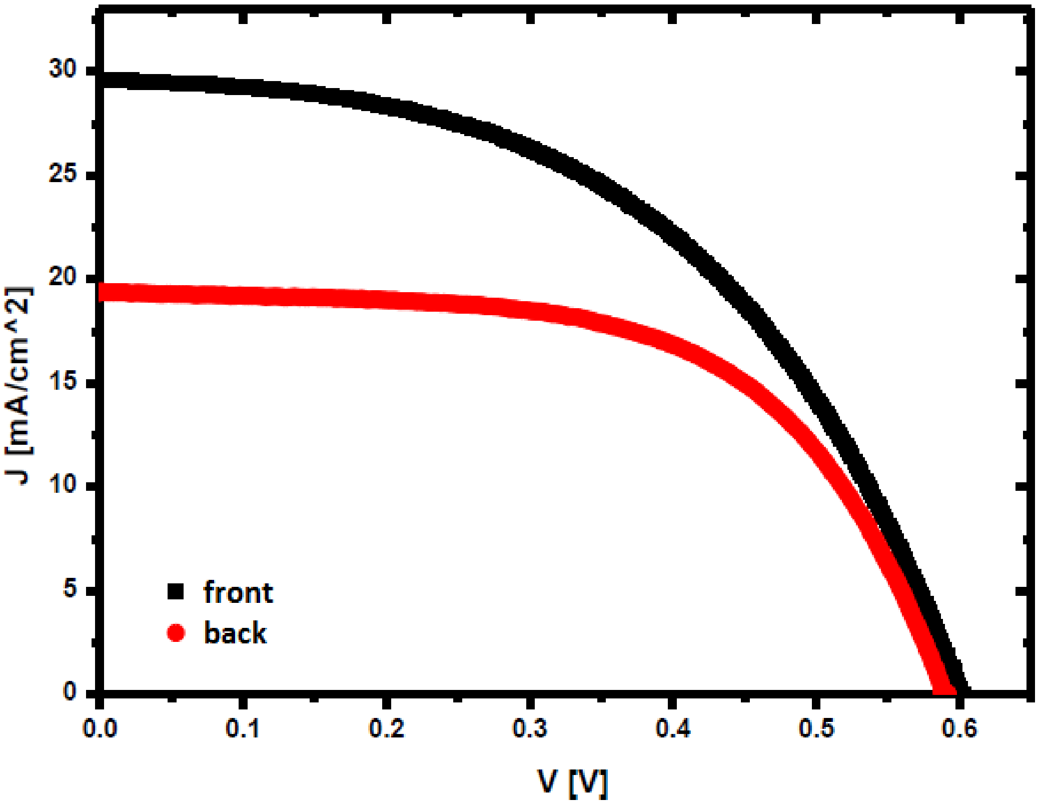

Fig. 5.17 J-V characteristics of full size heterojunction without intrinsic a-Si:H layer on p-type c-Si wafer

When the active area of the cell is lowered to 1.56 cm^2, the photovoltaic parameters were increased tremendously as seen in Table 5.18 and Figure 5.18.

Series resistance got lowered and shunt resistance increased, which lead to higher photovoltaic properties. This might be explained by more uniform a-Si:H films in lower areas and also contact sizes are getting lower, as their shadow.

Table 5.18 Photovoltaic properties for 1.56 cm^2 area heterojunction on p-type c-Si wafer

	Efficiency (%)	**Fill Factor (%)**	**V_{oc} (V)**	**J_{sc} (mA/cm^2)**
Front side	15.85	69.49	0.583	33.66
Back side	9.94	69.79	0.569	21.53

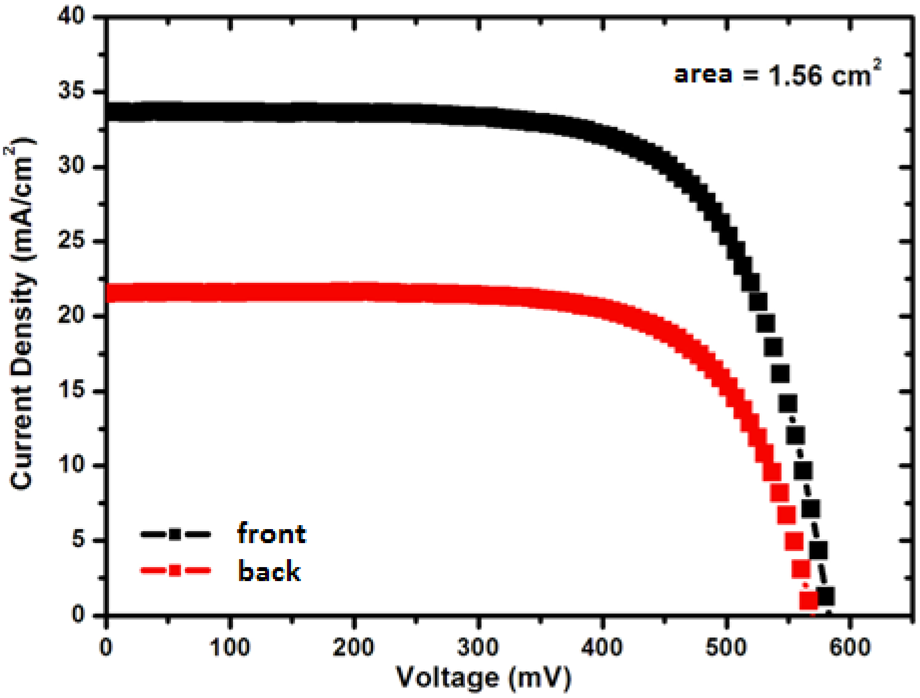

Fig. 5.18 J-V characteristics of 1.56 cm^2 heterojunction without intrinsic a-Si:H layer on p-type c-Si wafer

The same study was done on n-type c-Si wafer also. The deposition parameters of p- and n+ layers were shown in Table 5.19 below.

Table 5.19 Deposition parameters for heterojunction on n-type c-Si wafer

Layer	Dep. time (s)	F_{SiH4} (sccm)	F_{dopant} (sccm)	N_{dopant}/N_{SiH4}	Pressure (Torr)	Power (W)	T (°C)
a-Si:H(p)	40	185	65	0.07	1.0	50	120
a-Si:H(n+)	160	200	50	0.05	1.0	50	180

Table 5.20 Photovoltaic properties for 3.32 cm^2 area heterojunction on n-type c-Si wafer

	Efficiency (%)	Fill Factor (%)	V_{oc} (V)	J_{sc} (mA/cm^2)
Front side	8.82	47.01	0.544	29.64
Back side	2.48	62.09	0.486	7.07

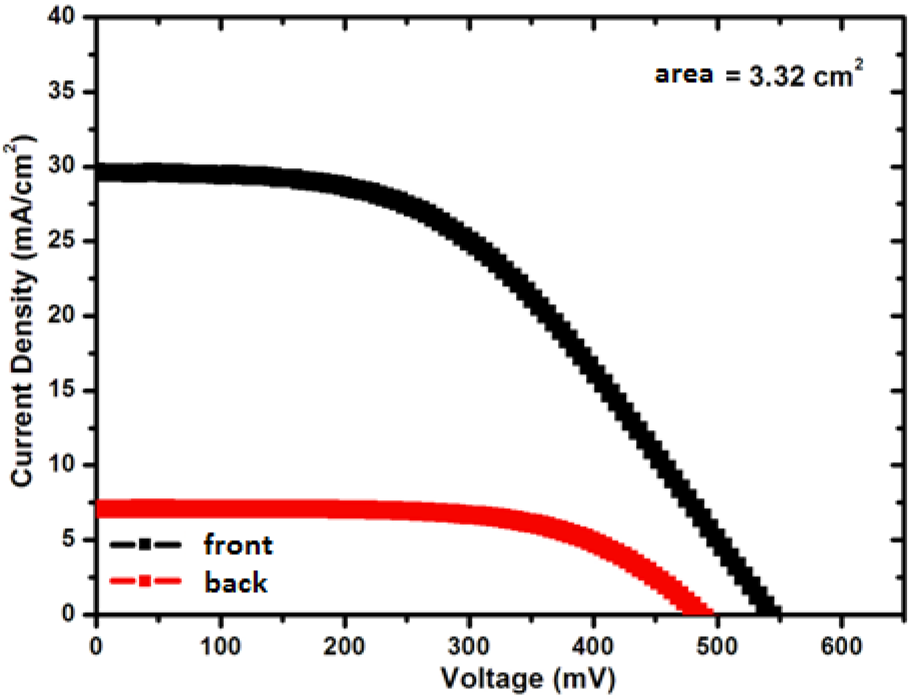

Fig. 5.19 J-V characteristics of 1.56 cm^2 heterojunction without intrinsic a-Si:H layer on n-type c-Si wafer

The photovoltaic properties and J-V characteristics for 3.32 cm^2 active area heterojunction on n-type c-Si were shown in Table 5.20 and Figure 5.19 above. Again the back side showed lower efficiency. The fill factor of the back side is higher when compared to front. However, when the current density is low, fill factor automatically is high for working junction. When compared to un-complete stack (see Table 5.9), BSF layer made the cell better in terms of efficiency, voltage and current density. On the other hand, fill factor decreased slightly. This decrease was due to thicker a-Si layer, which means higher series resistances.

5.2.5 Passivation Studies

Crystalline silicon wafers have several dangling bonds on the surface. Those dangling bonds act as recombination centers on the interfaces. Therefore open circuit voltage of the cell gets lowered if no passivation is made. Passivation can be made with several materials such as silica, silicon nitride, hydrogenated amorphous silicon or hydrogen radicals formed in the plasma. In HIT structure, this passivation is made by a-Si:H but instead of intrinsic a-Si:H, silicon oxide, silicon nitride and hydrogen plasma treatment were also studied because a-Si:H was increasing the defect density at the surface at earlier steps of the study.

5.2.5.1 Oxide Passivation

a-SiO$_X$ layer was deposited on 125 x 125 mm^2 p-type c-Si wafer on both sides under 400 mbar pressure, 2000 sccm O$_2$ flow rate and 950 ºC for several thicknesses by diffusion furnace. After oxidation, samples were prepared in 3 x 3 cm^2 size. Then, the a-Si:H and AZO layers were deposited in GÜNER. Silver contacts were thermally evaporated. In Figure 5.20, the final stack is sketched.

In Table 5.21, deposition parameters of a-Si:H layers are tabulated.

Table 5.21 Deposition parameters for a-Si:H layers in oxide passivation study

Layer	**Dep. Time (s)**	**F_{SiH4} (sccm)**	**F_{dopant} (sccm)**	**N_{dopant}/N_{SiH4}**	**Pressure (Torr)**	**Power (W)**	**T (ºC)**
a-Si:H(n)	160	200	50	0.05	1.0	50	180
a-Si:H(p+)	40	185	65	0.07	1.0	50	120

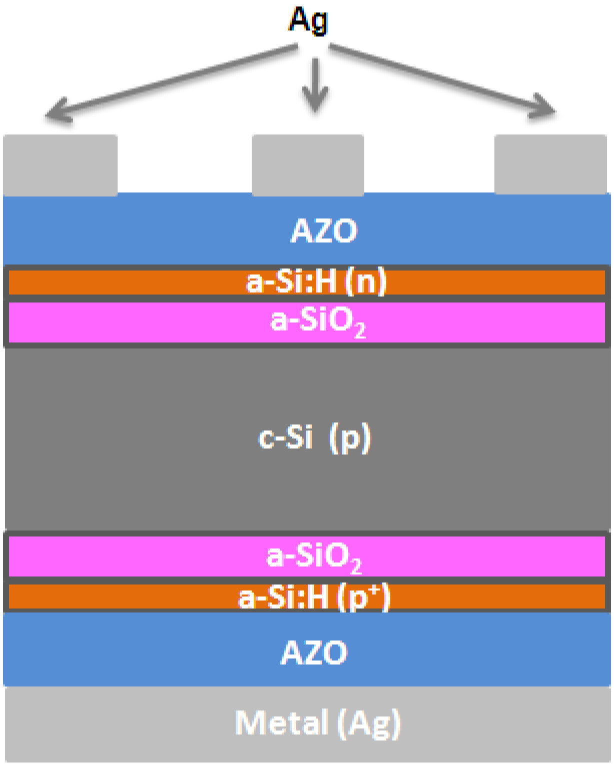

Fig. 5.20 Oxide passivated heterojunction stack

Table 5.22 Oxide passivation results with respect to deposition time

a-SiO$_x$ deposition time (s)	Efficiency (%)	Fill Factor (%)	V_{oc} (mV)	J_{sc} (mA/cm^2)
-	9.74	59.48	555.74	25.06
20	1.67	24.69	464.82	12.39
40	0.0992	25.28	305.62	1.09
60	3.02	36.40	488.36	14.43
120	0.13	26.24	448.36	0.96

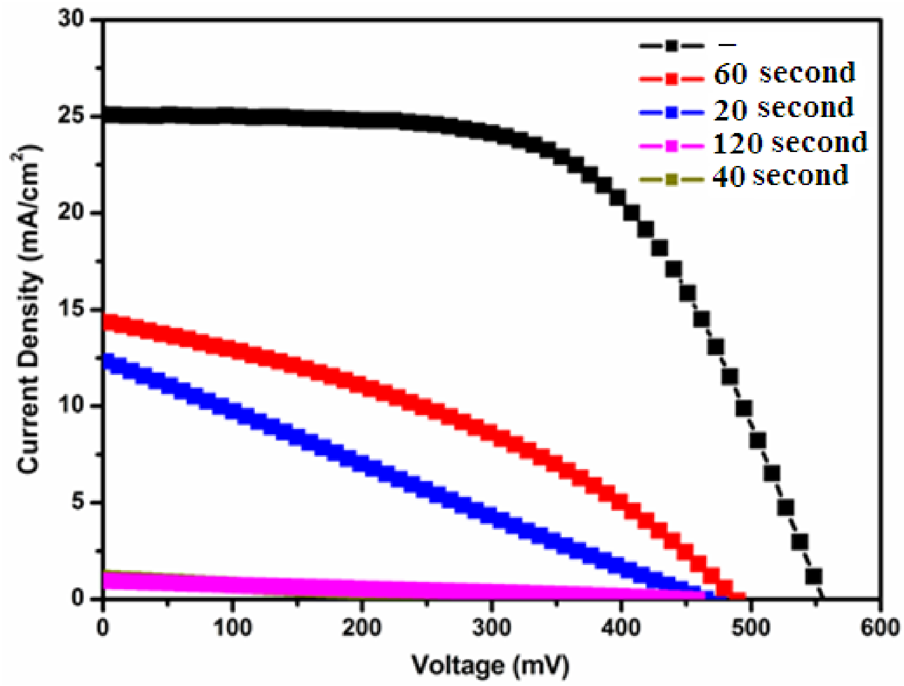

Fig. 5.21 J-V curves of oxide passivation study

From Table 5.22, it was clearly understood that the oxidation has failed as a passivation process. Figure 5.21 showed the resistivity of the films are getting higher as the film gets thicker. Thus, silicon oxide is not a proper material for heterojunction under the circumstances.

5.2.5.2 Nitride Passivation

a-SiN_x layer was deposited on 125 x 125 mm^2 p-type c-Si wafer on both sides under 1 Torr pressure, 300 sccm SiH_4 and 1200 sccm NH_3 flow rates, 380 ºC for several thicknesses by PECVD (SEMCO). After nitridation, samples were prepared in 3 x 3 cm^2 size. Then, the a-Si:H and AZO layers were deposited in GÜNER. Silver contacts were thermally evaporated. In Figure 5.22, the final stack is sketched.

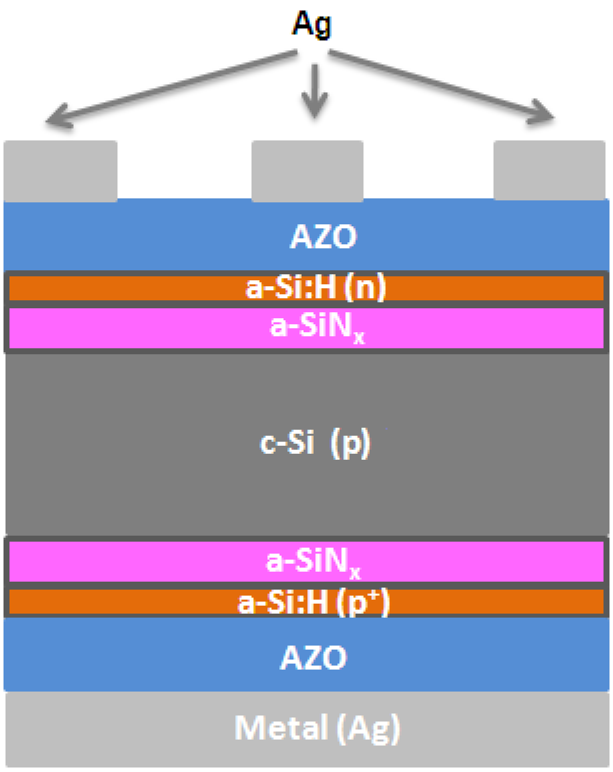

Fig. 5.22 Nitride passivated heterojunction stack

Table 5.23 Nitride passivation results with respect to deposition time

a-SiN$_x$ deposition time (s)	**Efficiency (%)**	**Fill Factor (%)**	**V$_{oc}$ (mV)**	**J$_{sc}$ (mA/cm^2)**
-	9.66	58.96	559.72	24.88
10	0	0	0	0
30	0	0	0	0
60	0	0	0	0

It was clearly understood that silicon nitride deposition on the surfaces completely prevented junction formation. Therefore, under these conditions silicon nitride is not an alternative passivation material.

5.2.5.3 Hydrogen Plasma Passivation

Lastly, hydrogen plasma treatment of p-type c-Si wafer was considered. Hydrogen was assumed to be break into radicals in the plasma and fill the dangling bonds on the surface. The stack is plotted in Figure 5.23. Hydrogen plasma ignition conditions were listed in Table 5.24.

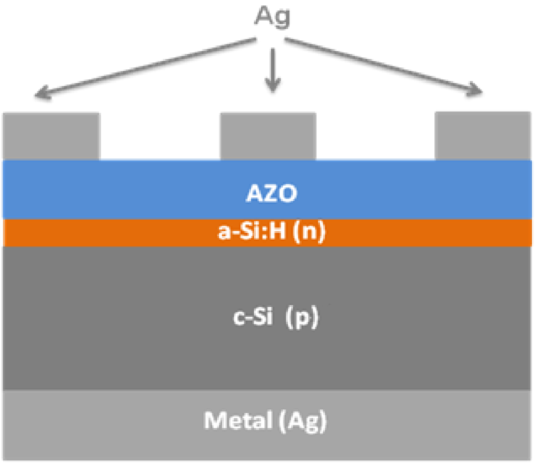

Fig. 5.23 Hydrogen plasma treated heterojunction stack

Table 5.24 Hydrogen plasma properties

F_{H2} (sccm)	Pressure (Torr)	Power (W)	T (ºC)
160	1.0	50	RT

Table 5.25 Photovoltaic properties with respect to hydrogen plasma treatment duration

H_2 plasma treatment time (s)	Efficiency (%)	Fill Factor (%)	V_{oc} (mV)	J_{sc} (mA/cm^2)
-	10.38	62.41	550.33	25.80
15	2.73	26.52	379.05	24.45
60	1.48	19.71	404	16.66

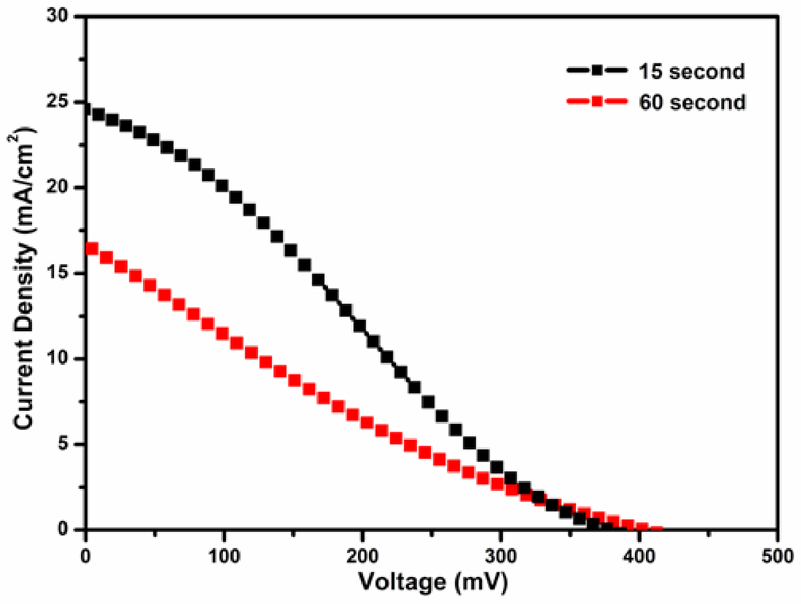

Fig. 5.24 J-V curves of hydrogen plasma passivation study

It is obvious from Table 5.25 and Figure 5.24, hydrogen plasma damaged the surface. In this ignition conditions, hydrogen plasma is not a suitable passivation method either.

5.2.6 Intrinsic a-Si:H Layer Optimization in HIT Structure

Earlier experience on a-Si:H passivation was showed that wafer cleaning is one of the most important steps in HIT solar cell production. Therefore, before beginning to optimization of intrinsic a-Si:H layer, RCA cleaning recipe and pyramid rounding step was included to the cleaning procedure. The best cleaning and rounding parameters were obtained without intrinsic layer. Then they were applied to the intrinsic a-Si:H optimization study. In this part, p-type c-Si wafers were used as the substrate.

5.2.6.1 Effects of Power and Pressure

It was shown that deposition pressure and applied RF power mostly affect the thickness uniformity. However, in HIT structure intrinsic layer is as thin as 3 nm [21,45,46]. So, power and pressure were also considered as parameters.

In the power optimization study, deposition pressure, substrate temperature and silane flow rate were kept constant at 1 Torr, 200 °C and 350 sccm, respectively. In each deposition at least four cells were produced. In Table 5.26, the photovoltaic properties were taken as the average of those cells. Each property was reported as before and after annealing of samples at 180 °C under air atmosphere for 20 minutes. Reference cell was the best cell (a-Si:H(n) / c-Si(p)) without intrinsic layer deposited at 1 Torr, 50 W, 180 °C, 288 sccm silane and 72 sccm phosphine flow rates.

Table 5.26 Photovoltaic properties with respect to power levels at 1 Torr

Power (W)	**V_{oc}(mV)**		**J_{sc}(mA/cm2)**		**FF(%)**		**Series res.**		**Shunt res.**		**Efficiency(%)**	
	Bef.	**Aft**	**Bef.**	**Aft**	**Bef.**	**Aft**	**Bef.**	**Aft**	**Bef.**	**Aft**	**Before**	**After**
No intrinsic	520	547	27,07	28,03	58,33	61,22	1,75	1,35	192,01	576,96	10,26	11,73
15 W	416	481	29,50	29,82	36,20	40,62	3,37	3,56	24,86	27,10	5,55	7,28
30 W	442	520,2	28,89	29,52	49,66	56,01	1,80	1,48	180,27	164,38	7,91	10,74
50 W	428	499	29,77	30,24	43,21	45,40	2,20	2,32	44,59	42,08	6,87	8,65
100 W	448	492	27,75	28,30	46,64	54,23	2,41	1,52	85,42	123,74	7,00	9,10

As understood from Table 5.25, 1 Torr may not be a suitable working regime. V_{oc} values could not exceed the reference value of 547 mV. At this pressure regime there might be so many reactive radicals in the chamber, which might lead to a less quality film in terms of defects.

The next step was to figure out a proper pressure-power regime. So the deposition pressure was lowered to 0.6 Torr. At lower pressures with constant flow rate, the residence times of the molecules are less. At low powers, although deposition rates are low, the film quality is better in terms of defect density. So both lowering power and pressure was expected to lead to a better performance of the cell. The corresponding results were tabulated in Table 5.27. Substrate temperature and silane flow rate were kept constant at 200 °C and 350 sccm, respectively.

A parameter set of 20 W and 0.6 Torr reached the reference cell as seen in Table 5.26. Only series resistance value is slightly higher, which is probably due to thicker a-Si:H. J-V curve of the best cell with an active area of 0.9 cm^2 is plotted in Figure 5.25.

Table 5.27 Photovoltaic properties with respect to power levels at 0.6 Torr

Power (W)	**Voc(mV)**		**Jsc(mA/cm2)**		**FF(%)**		**Series res.**		**Shunt res.**		**Efficiency(%)**	
	Bef.	**Aft**	**Bef.**	**Aft**	**Bef.**	**Aft**	**Bef.**	**Aft**	**Bef.**	**Aft**	**Before**	**After**
No intrinsic	520	547	27,07	28,03	58,33	61,22	1,75	1,35	192,01	576,96	10,26	11,73
20 W	422	541	28,55	28,29	45,36	57,51	2,18	1,68	56,23	549,2	6,82	10,99
25 W	377,2	514,4	28,37	30,14	36,15	47,39	3,04	2,31	29,39	94,65	4,86	9,17

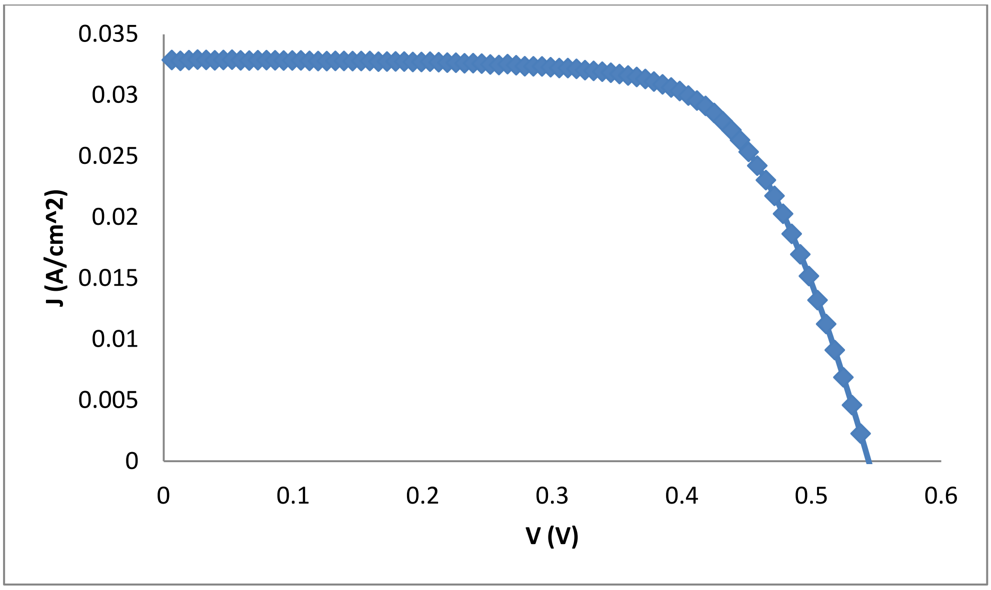

Fig. 5.25 J-V curve of 0.9 cm^2 cell deposited at 0.6 Torr, 20 W

Lowering the deposition pressure to 0.3 Torr while keeping the power at 15 W was also studied. Plasma ignition is not possible under 15 W in GÜNER. Substrate temperature and silane flow were also fixed at 200 °C and 350 sccm, respectively. The results were averaged and given in Table 5.28. The reference cannot be reached at this pressure.

Table 5.28 Photovoltaic properties with respect to power levels at 0.3 Torr

Power (W)	**Voc(mV)**		**Jsc(mA/cm2)**		**FF(%)**		**R$_s$**		**R$_{sh}$**		**η(%)**	
	Bef.	**Aft.**	**Bef.**	**Aft.**	**Bef.**	**Aft.**	**Bef.**	**Aft.**	**Bef.**	**Aft**	**Bef**	**Aft.**
No intrinsic	520	547	27,07	28,03	58,33	61,22	1,75	1,35	192,01	576,96	10,26	11,73
15 W	402,5	522,6	28,31	28,88	37,43	42,36	3,22	3,70	31,12	46,01	5,35	8,01

Effects of power and pressure studies were simply plotted in Figure 5.26 with respect to V_{oc}. If there was a proper passivation V_{oc}'s should be around 600 mV's [ref]. However, none of the results could exceed the reference.

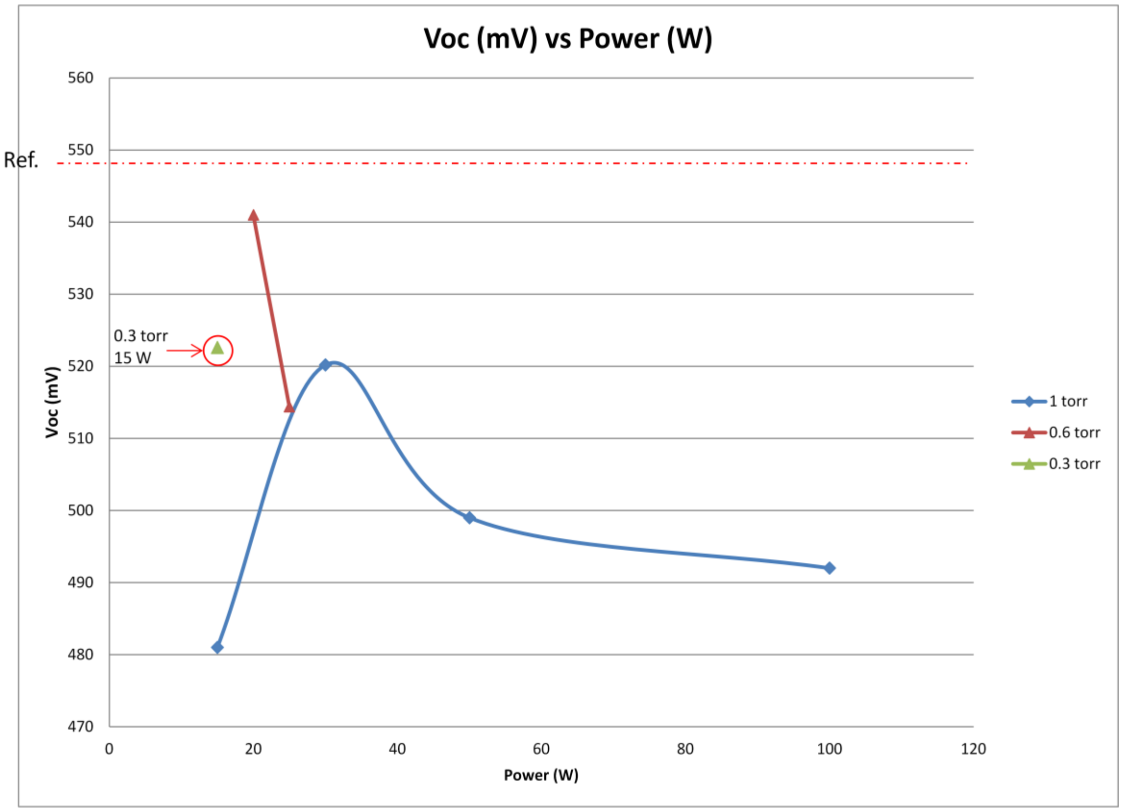

Fig. 5.26 V_{oc} with respect to several pressure and power levels

5.2.6.2 Effects of Substrate Temperature

Substrate temperature is another important parameter in HIT structure layer depositions. At high temperatures epitaxial growth is possible. If that is the case, there will be no passivation by intrinsic a-Si:H. Generally this layer is deposited below 200 °C to avoid epitaxial growth.

120-200 °C range was investigated for this study while keeping the applied RF power, deposition pressure and silane flow rate at constant values of 20 W, 0.6 Torr and 350 sccm, respectively. In Table 5.29, photovoltaic properties with respect to temperature variation can be seen. The most efficient temperature was found to be 120 °C. At last, this sample exceeded the reference cell's photovoltaic properties.

Table 5.29 Photovoltaic properties with respect to substrate temperature

Substrate Temp.	Voc(mV)		Jsc(mA/cm^2)		FF(%)		Series res.		Shunt res.		Efficiency(%)	
	Bef.	**Aft**	**Bef.**	**Aft**	**Bef.**	**Aft**	**Bef.**	**Afr**	**Bef.**	**Aft**	**Before**	**After**
200 °C	422	541	28,55	28,29	45,36	57,51	2,18	1,68	56,23	549,2	6,82	10,99
150 °C	389	514,75	26,71	29,78	26,89	41,53	6,39	2,95	11,42	30,05	3,45	7,83
120 °C	409,8	550,7	29,39	29,12	50,55	61,50	1,82	1,28	285,64	1463,6	7,87	12,55

5.2.6.3 Effects of Post-annealing

The most efficient cell was deposited under 120 °C substrate temperature, 0.6 Torr deposition pressure, 20 W power, and 350 sccm SiH_4 flow rate. Therefore, the post-annealing study was done for this sample. Two annealing sets were conducted. First, temperature was kept constant at 220 °C and annealing times were varied. Second, annealing duration kept constant at 20 minutes and annealing temperature was varied from 180-260 °C.

First, annealing duration was optimized while keeping the annealing temperature constant at 220 °C. Annealing was done under air atmosphere. The photovoltaic properties of the cells increased up to 20 minutes and after exceeding this duration cells got worsened as seen in Figure 5.27 and Table 5.30. Therefore, 20 minutes of annealing duration was decided to be the time limit for ongoing studies.

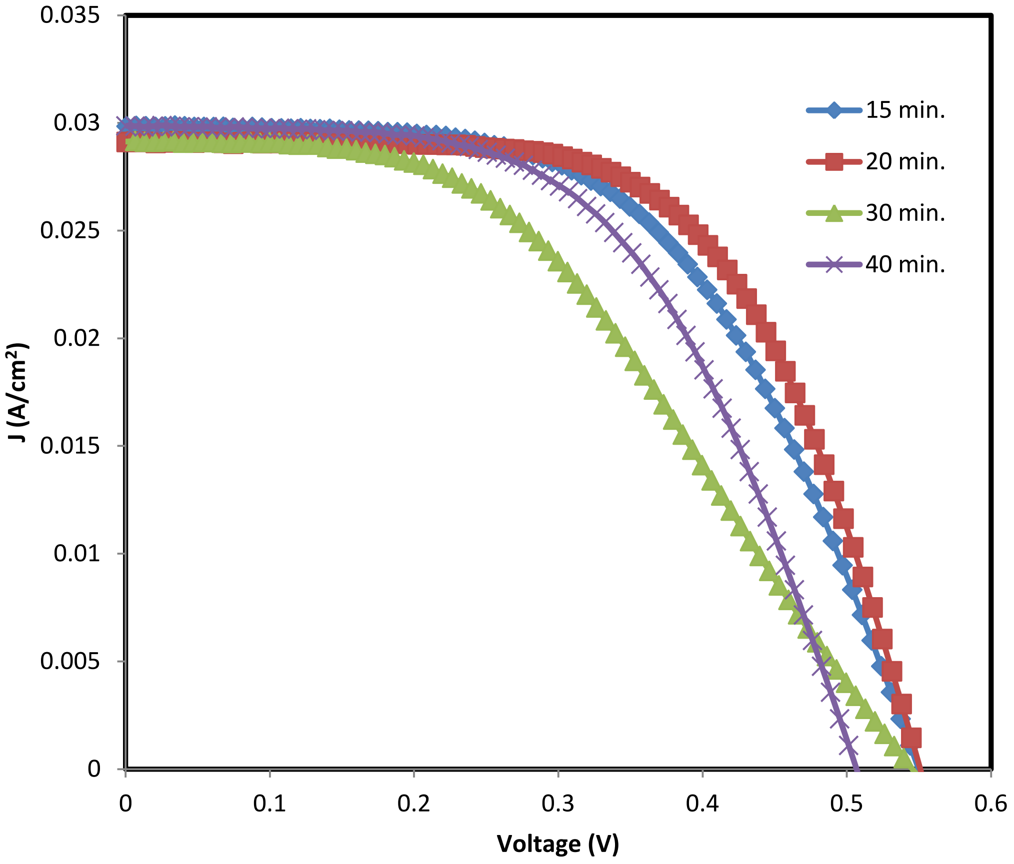

Fig. 5.27 J-V curve for post-annealing study at 220 °C for several annealing durations

Table 5.30 Photovoltaic properties with respect to post-annealing duration at 220 °C

Annealing Time	Voc(mV)		Jsc(mA/cm^2)		FF(%)		Series res.		Shunt res.		Efficiency(%)	
	Bef.	Aft.	Bef.	Aft.	Bef.	Aft.	Bef.	Aft.	Bef.	Aft.	Before	After
15 min	416,8	549,7	29,20	29,84	49,09	56,16	1,96	1,63	193,19	346,0	7,47	11,52
20 min	409,8	550,7	29,39	29,12	50,55	61,50	1,82	1,28	285,64	1463,6	7,87	12,55
30 min	410,5	545,3	29,62	29,12	47,64	51,73	1,98	2,21	141,74	1015,3	7,24	9,46
40 min	402,0	507,2	29,44	28,84	45,81	44,53	2,18	3,48	93,54	267,6	6,78	8,84

Second, annealing temperature was optimized while keeping the annealing duration constant at 20 minutes. Annealing was again done under air atmosphere. The photovoltaic properties of the cells increased up to 220 °C and after exceeding this temperature cells got worsened as seen in Figure 5.28 and Table 5.31. This phenomenon was explained by the degradation of AZO layer at higher temperatures than 240 °C. Therefore, annealing temperature of 220 °C was decided to be the optimum temperature for ongoing studies.

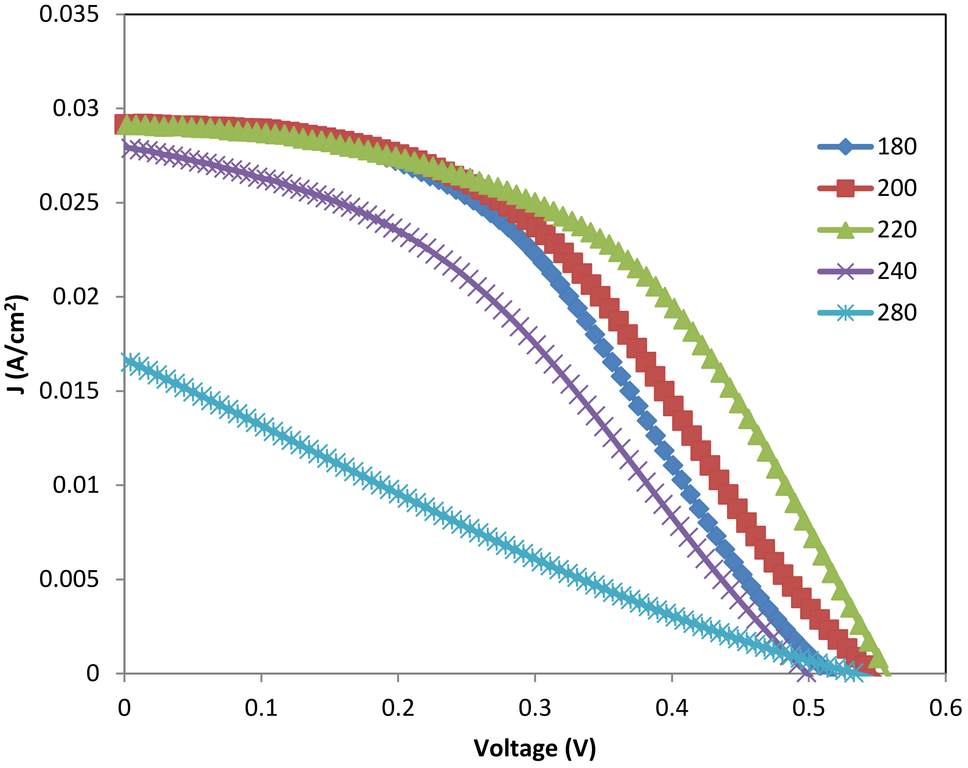

Fig. 5.28 J-V curve for post-annealing study for several temperatures last for 20 minutes

Table 5.31 Photovoltaic properties with respect to post-annealing temperatures for 20 minutes

Temp (°C)	**Voc (mV)**	**Jsc (mA/cm2)**	**FF (%)**	**Series res.**	**Shunt res.**	**Efficiency (%)**
180	514,8	29,07	44,66	3,99	88,83	8,36
200	547,7	29,21	51,22	2,29	124,76	10,24
220	557,5	29,03	49,93	2,31	74,58	10,10
240	540,9	27,79	38,45	3,98	25,22	6,66
260	534,5	16,67	21,87	15,23	8,93	2,44

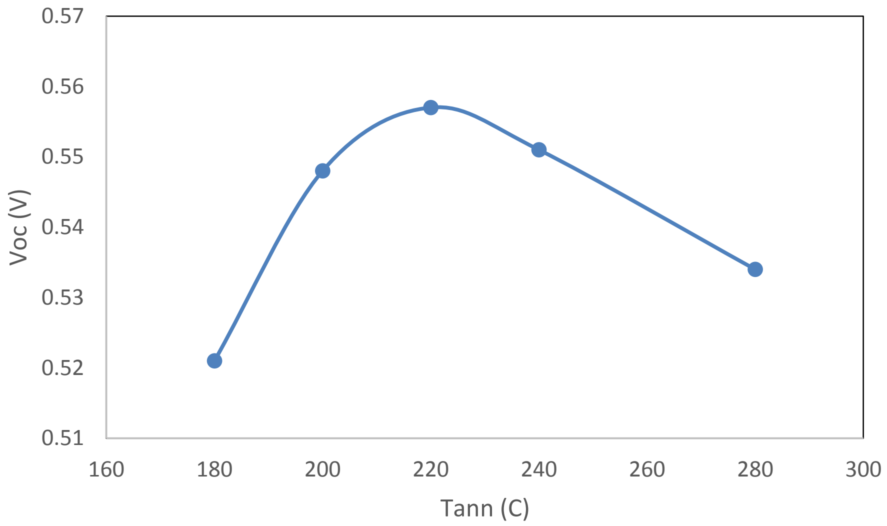

Fig. 5.29 V_{oc} variation with respect to annealing temperature

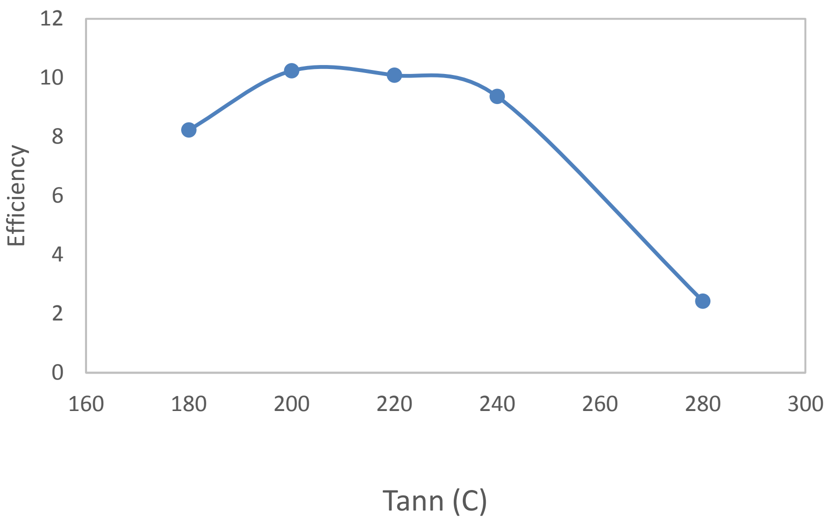

Fig. 5.30 Efficiency variation with respect to annealing temperature

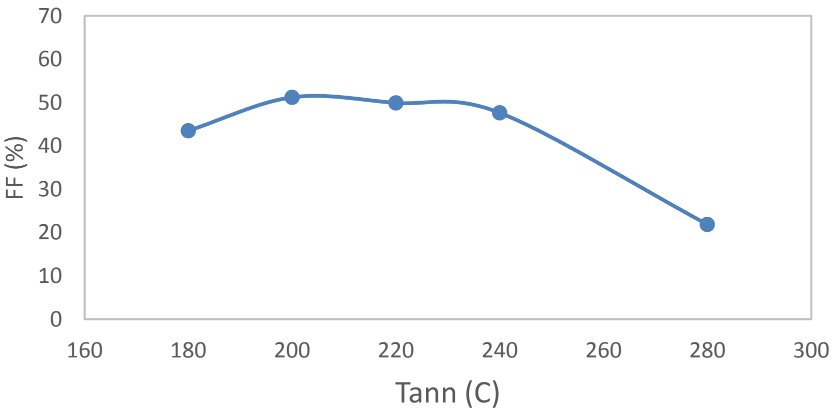

Fig. 5.31 Fill factor variation with respect to annealing temperature

In figures 5.29 to 5.31, V_{oc}, efficiency and fill factor variation with respect to annealing temperature was plotted. In terms of passivation (V_{oc}), it makes a peak at 220 °C as seen from Figure 5.29. Efficiency and fill factor did not affected by annealing temperature up to 240 °C, but exceeding this limit lowered these properties. Exceeding this limit might lead to breaking of hydrogen bonds in the amorphous silicon structure. Thus the defect density in amorphous phase may increase.

5.2.6.4 Effects of Hydrogen Dilution

The less defective a-Si:H material is deposited under hydrogen dilution and at low powers, at which phase transition from amorphous to micro-crystalline silicon nearly occurs. The silane gas used in GÜNAM is 10 % diluted in hydrogen, so silane ratio is already 10 %. Phase transition study was conducted earlier (see Chapter 4). When this ratio was around 4 %, phase transition occurs in GÜNER CCP chambers. Therefore extra hydrogen addition to the gas mixture should be low. For this study, 15 and 40 sccm hydrogen flow was added to the gas mixture and the results were tabulated below in Table 5.32. 15 sccm H_2 addition increased the photovoltaic properties tremendously.

Table 5.32 Photovoltaic properties with respect to hydrogen dilution

SiH_4 Flow Rate (sccm)	**H_2 Flow Rate (sccm)**	**Voc (mV)**		**Jsc (mA/cm2)**		**FF (%)**		**Series res.**		**Shunt res.**		**Efficiency (%)**	
		Bef.	**Aft**	**Bef.**	**Aft**	**Bef.**	**Aft**	**Bef.**	**Aft**	**Bef.**	**Aft**	**Before**	**After**
350	0	472,6	509,3	29,05	30,12	27,63	32,86	7,01	5,17	21,89	34,79	4,68	6,20
350	15	424,3	550,7	29,38	29,12	50,54	61,50	1,81	1,28	285,64	1358	7,87	12,55
310	40	329,7	455,6	22,3	29,4	19,3	28,39	9,12	5,28	3,93	20,77	1,75	4,72

CHAPTER 6

MODELING OF PECVD SYSYEM

6.1. Current Design of CCP Chamber

GÜNER was installed in 2010. Afterwards, the first temperature calibration studies were started. From the first studies, it was understood that the anode design must be changed in order to reach the desired temperature levels and uniformities. It took one and a half year to modulate this design without changing the system geometry. Modulations included removal of cooling water lines, changing the positions of heaters and addition of heat reflectors under heaters.

A schematic illustration of one of the capacitively coupled plasma (CCP) chambers of GÜNER is shown in Figure 6.1. In order to visualize the position of heaters, front wall was made transparent. The heaters shown in orange color are embedded in anode. Anode walls are made of aluminum, thus a severe pressure difference may deform the anode. Therefore it is pumped individually by a mechanical pump to nearly equalize the pressure inside the anode and the chamber. Each heater has a power of 1000 W and they are connected in parallel. Thus if one collapses, the others keep working. In Figure 6.2, electrodes were made transparent to visualize the ceramic heaters.

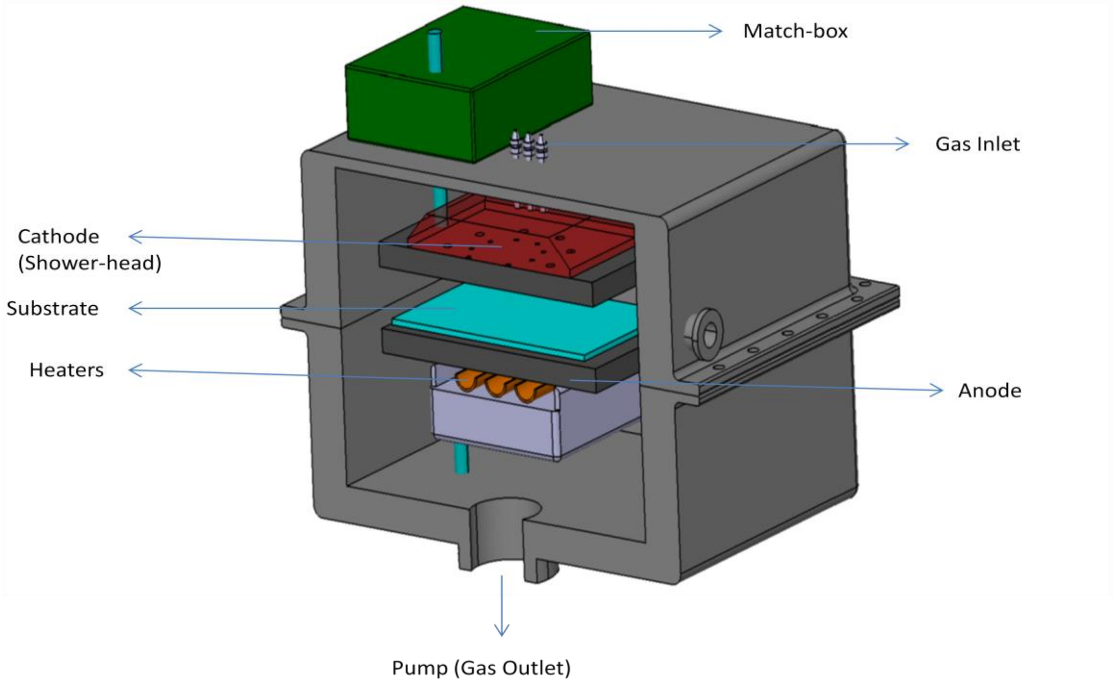

Fig. 6.1 Schematic drawing of a CCP chamber

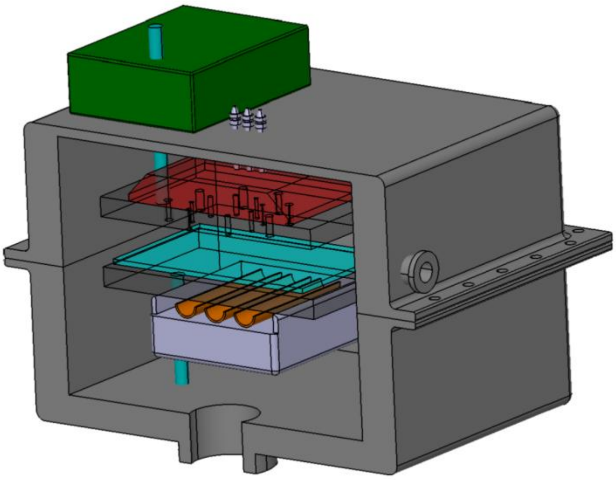

Fig. 6.2 Transparent electrode drawing of a CCP chamber

The heat transfer from the heaters to the electrode's inner walls are by surface to surface radiation. Substrate that is painted in turquoise color, is in direct contact with the electrode, so the heat transfer mechanism is conduction. Substrate loses heat from its surface by radiation to the chamber walls. Outside the chamber, the clean room is kept constant at 20 °C via air conditioner.

In order to simplify the heat transfer mechanism, two dimensional drawing of the chamber is shown in Figure 6.3.

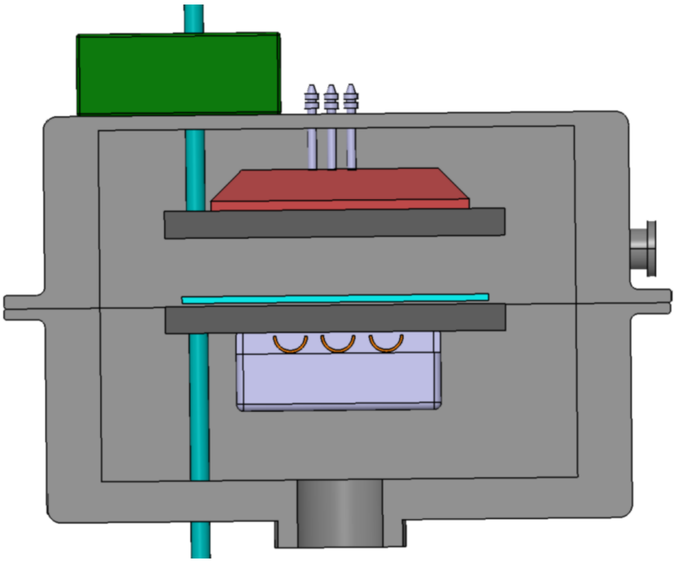

Fig. 6.3 2-D drawing of a CCP chamber

Heat transfer mechanisms starting from heaters are as follows;

1. Describe the heaters as heat sources.

2. Heat transfer from heaters and from heat reflectors to the inner walls of the anode by surface to surface radiation.

3. Conductive heat transfer in the electrode walls.

4. Conductive heat transfer in the substrate.

5. Heat loss through the substrate and the side walls of the anode to chamber walls by surface to surface radiation.

6. Conductive heat transfer inside the outer chamber walls.

7. Heat loss through the outer chamber walls to air by convective heat transfer.

Each term is described and explained mathematically in Appendix A. The resulting equation to be solved is;

$$\rho c_p \frac{\partial T}{\partial t} + \rho c_p u . \nabla T = \nabla . (k \nabla T) + Q_r \qquad \text{Eqn (6.1)}$$

where is the radiative heat transfer term and it can be formulized for all of the radiation surfaces as;

$$Q_r = \sigma A_i \sum_{j=1}^{n} F_{ij} \left(T_i^4 - T_j^4 \right) \quad i = 1,2, \dots , n \qquad \text{Eqn (6.2)}$$

where F_{ij} is the view factor that is explained in details in Appendix A, σ is the Stefan-Boltzmann constant that has the value of 5.67 x 10^{-8} W/m^2K^4.

It is clearly seen that these equations are so difficult to solve analytically. A numerical method should be used to investigate the temperature distributions on different nodes of the system.

6.2 Simulation of Current Design by COMSOL

First assumption while simulating the current system was to describe a simpler geometry that is mainly based on rectangular shapes. Then every parameter was described in the system in order to change the geometry just with changing these parameters which are tabulated in Table 6.1 below in units of cm.

After defining the parameters, the resulting geometry was obtained as seen in Figure 6.4. The enclosure or the chamber walls and the shaft were defined as stainless steel; anode, cathode and heat reflectors as aluminum; heaters as alumina and substrate as silica glass. All of these materials with their physical properties are available in COMSOL's material library.

Table 6.1 Geometrical parameters of current CCP system

Name	Expression	Value	Description
La	26	26.000	length of anode
ta	0.5	0.500	thickness of anode
taw	1	1.000	thickness of anode wall
ha	6	6.000	height of anode wall
tar	1.5	1.500	thickness of anode reflector
Lh	5	5.000	length of heater
th	0.75	0.750	thickness of heater
hs	2	2.000	height of sheath between heaters
ts	0.5	0.500	thickness of sheath between heaters
dw	1.25	1.250	distance of heater from wall
duw	0.25	0.250	distance of heater to the upper wall
tg	0.11	0.110	thickness of glass substrate
tr	0.25	0.250	thickness of reflector
wr	7	7.000	width of the reflector
dr	1.5	1.500	distance between reflectors
wsh	La/4	6.500	width of shaft
hsh	5	5.000	height of shaft
wch	67	67.000	width of chamber
tch	2	2.000	thickness of chamber
hch	23.5	23.500	height of chamber
wcat	35	35.000	width of cathode
hcat	8	8.000	height of cathode
wg	25	25.000	width of glass substrate

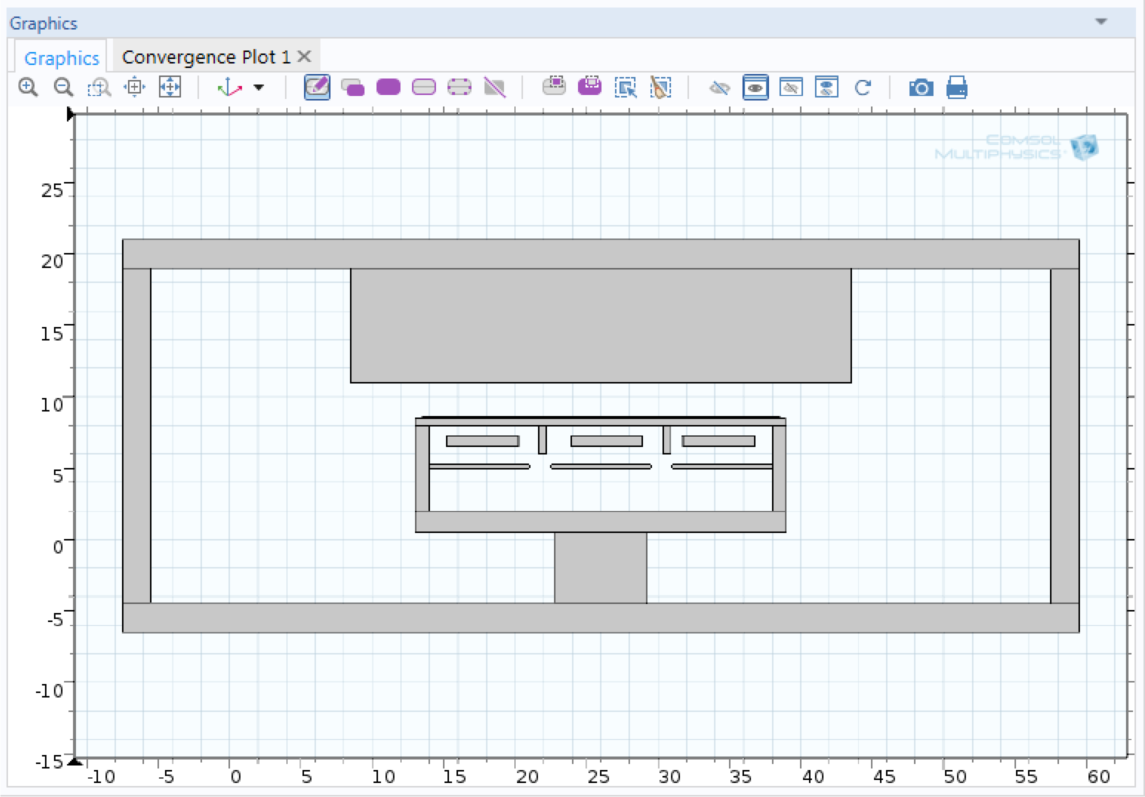

Fig. 6.4 Geometry for current CCP system

6.2.1 Simulation vs Empirical Data

For the simulation, heat transfer module of COMSOL was used with surface to surface radiation mode. All the interior surfaces of both anode and chamber were defined as surface to surface radiation boundary condition. Although the pressure in chamber reaches 10^{-6} Torr and pressure inside the anode was always maintained at 10^{-3} Torr, convection term was neglected in these regions. It is taken account for the outer sides of the chamber walls since the cleanroom is always kept at 20 °C via air conditioner. Substrate was assumed to be in full contact with anode, in other words no vacuum left between anode surface and substrate which may decrease heat transfer rate.

It is written in technical specification sheet of GÜNER that the substrate temperature can be risen up to 400 °C. As a first trial, the model was computed in steady-state that is independent of time. In this case, the maximum temperature values that can be obtained was modeled. The temperature distribution in thermally colored geometry can be seen in Figure 6.5.

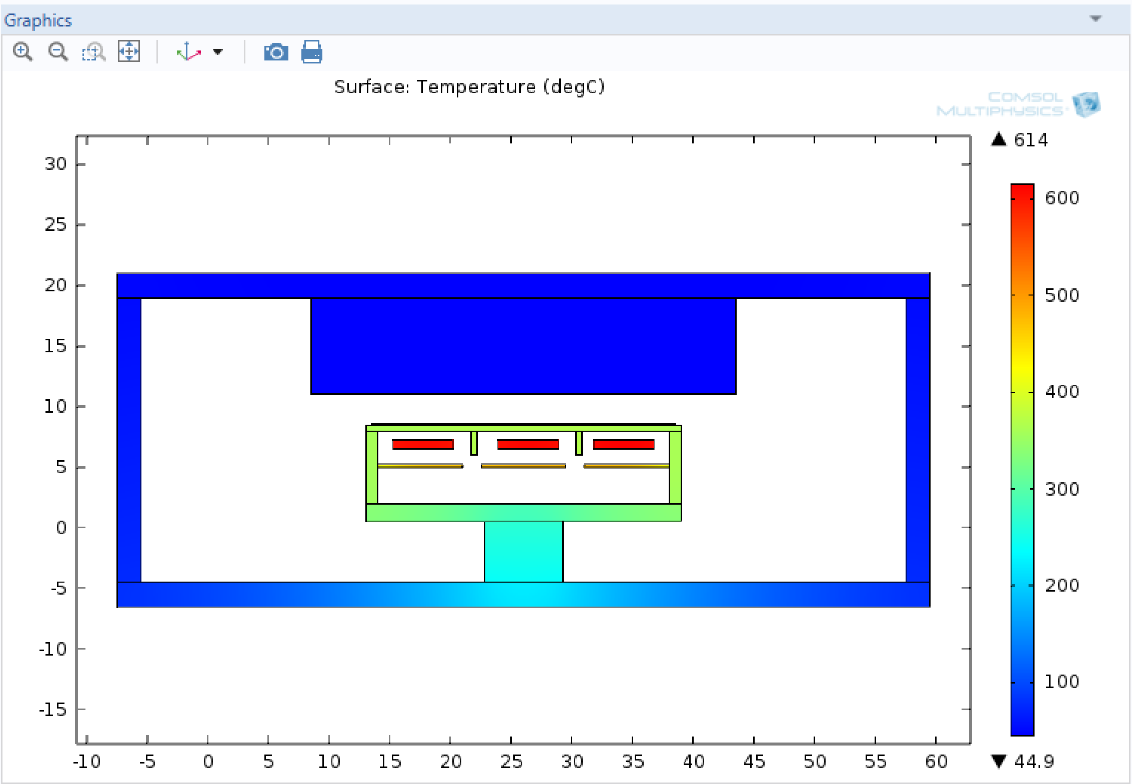

Fig. 6.5 Thermally colored CCP system at steady-state conditions

To realize the time necessary to reach steady-state was also modeled for a duration of 20 hours. As seen in Figure 6.6, the necessary time to thermal stabilization was found to be 390 minutes.

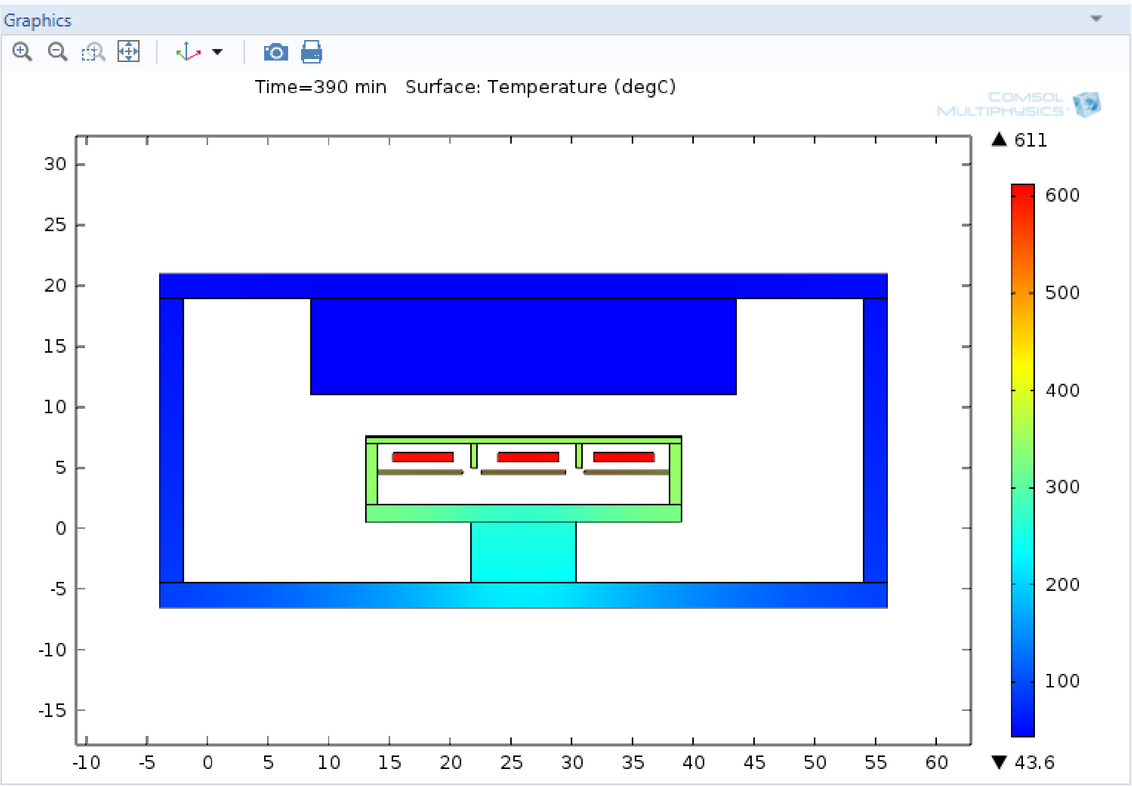

Fig. 6.6 Thermally colored CCP system after 390 minutes to reach steady-state conditions

The temperature distribution on the substrate surface at steady-state conditions was illustrated in Figure 6.7. It was found that the temperature at the center rises to 356 °C and the temperature at the edge is 324 °C. The temperature difference on the substrate surface is 32 °C, which is quite high. Another undesired result is that the substrate surface cannot reach 400 °C as written in the technical specification sheet provided, which was also empirically proven.

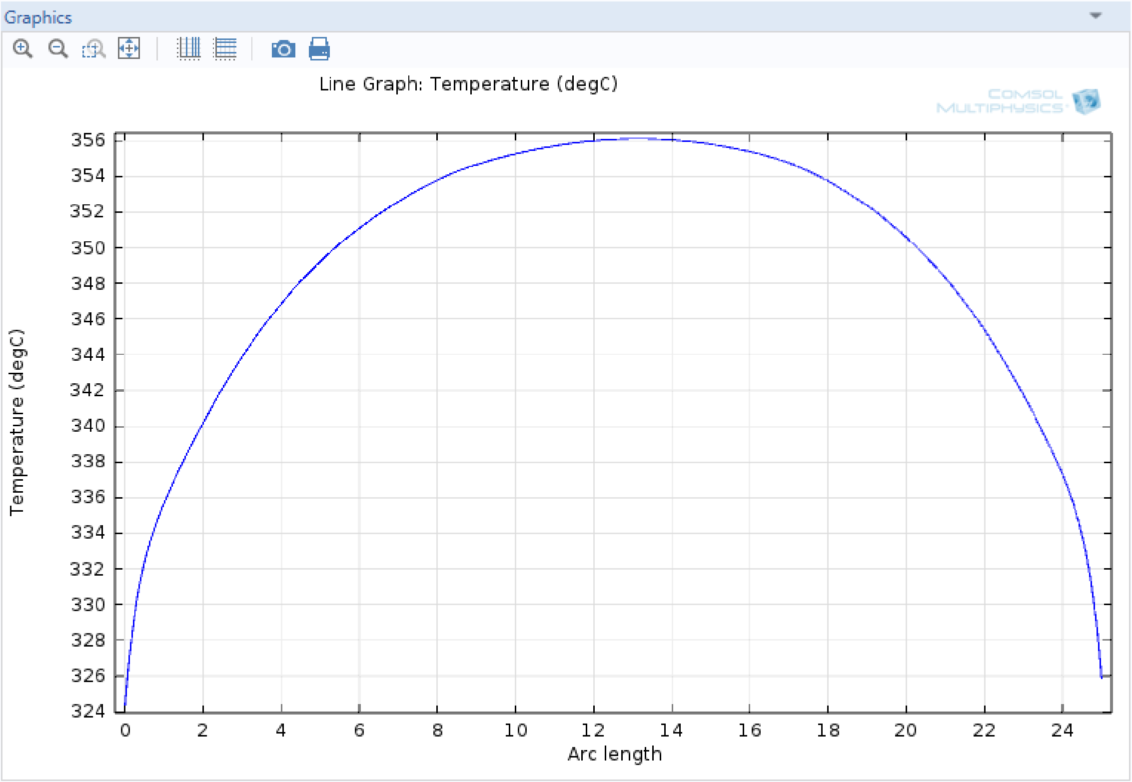

Fig. 6.7 The temperature distribution on the substrate surface

Substrate temperature with respect to time was illustrated in Figure 6.8 below. As expected, as time reaches 390 minutes, temperature on the surface increases to maximum and stabilizes.

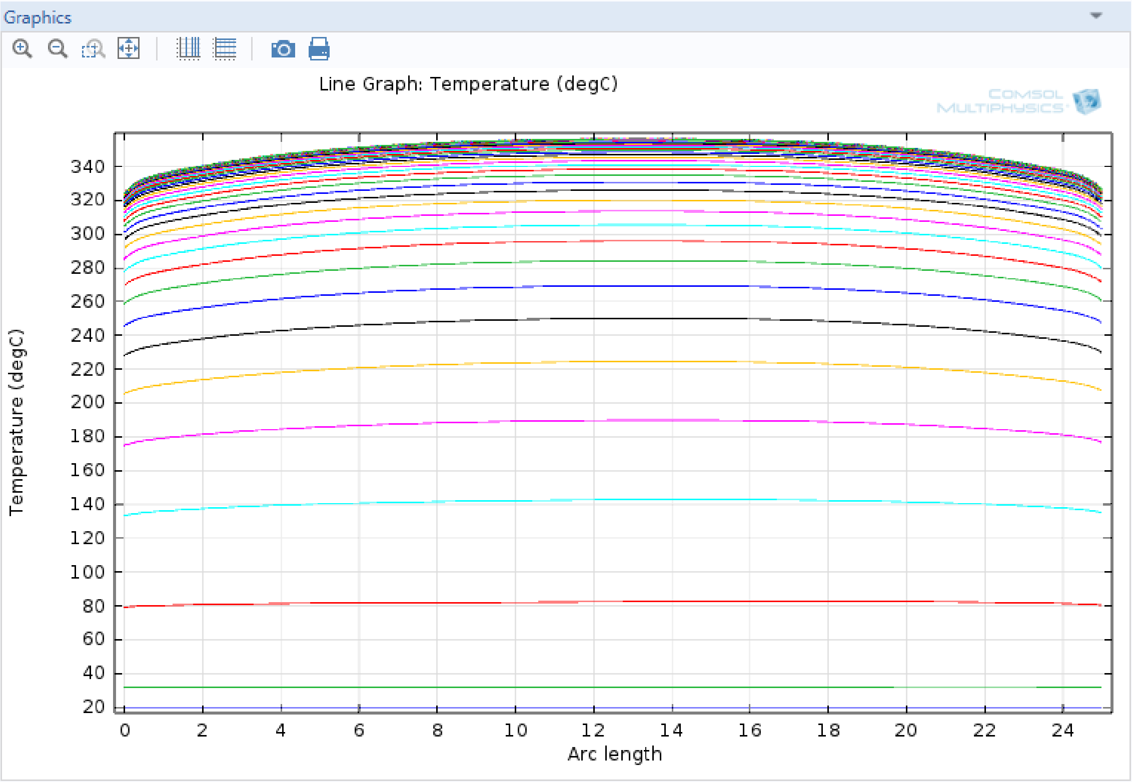

Fig. 6.8 Temperature distribution on the substrate surface with respect to time

Another limiting case in the current design is that the heaters cannot exceed 400 °C. Therefore, the case described above is ideal and is not realistic. Thus, in the next configuration, heaters were kept constant at 400 °C. The resulting illustration for steady-state is given in Figure 6.9. A time dependent model was also constructed and the same temperature levels were obtained after 280 minutes. In Figure 6.10, temperature distribution on the substrate surface is plotted. It was found that center has a value of approximately 193 °C whereas the edge was 180 °C. According to the model, substrate temperature cannot reach even 200 °C.

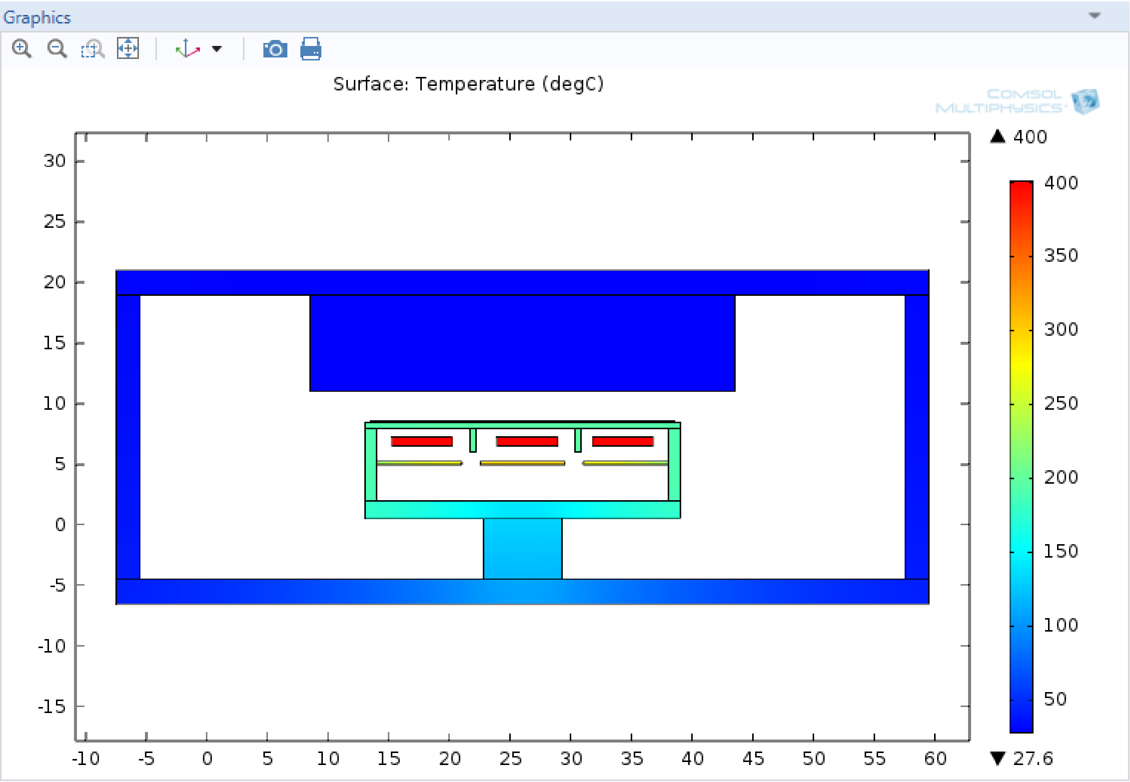

Fig. 6.9 Thermally colored CCP system at steady-state conditions when heaters were kept constant at 400 °C

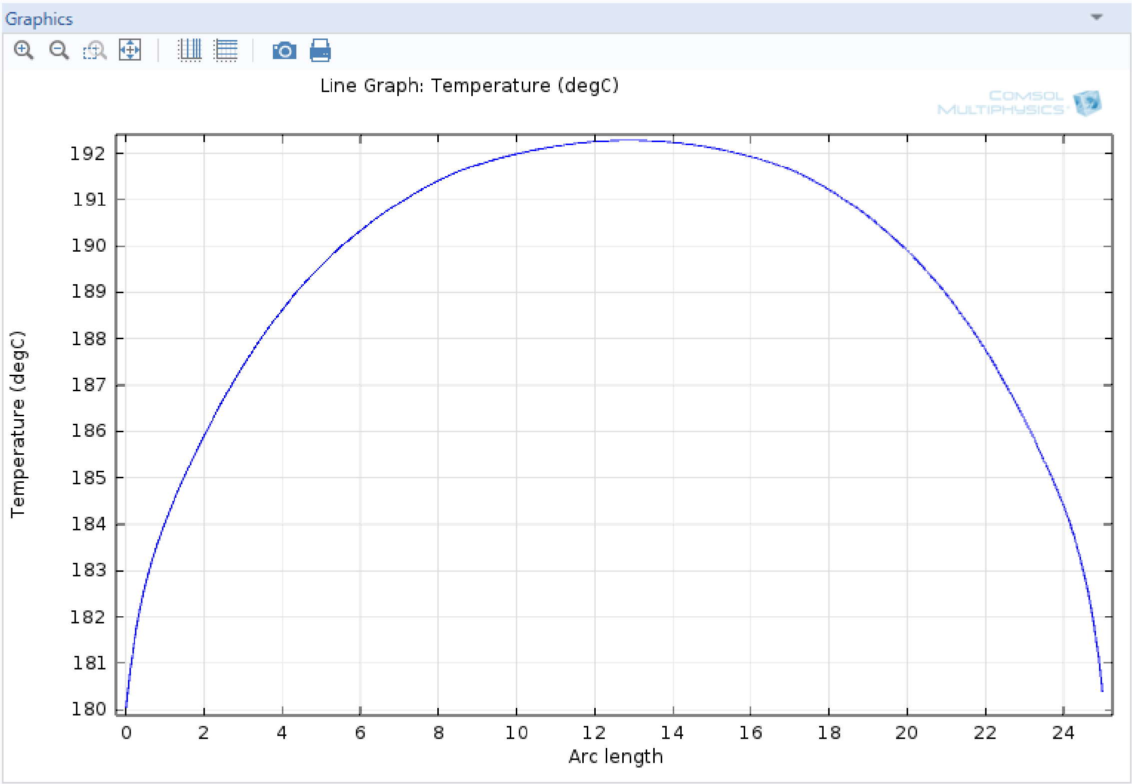

Fig. 6.10 Temperature distribution on the substrate surface when heaters were kept constant at 400 °C

Substrate temperature with respect to time was illustrated in Figure 6.11 below. As expected as time reaches 280 minutes, temperature on the surface increases and stabilizes.

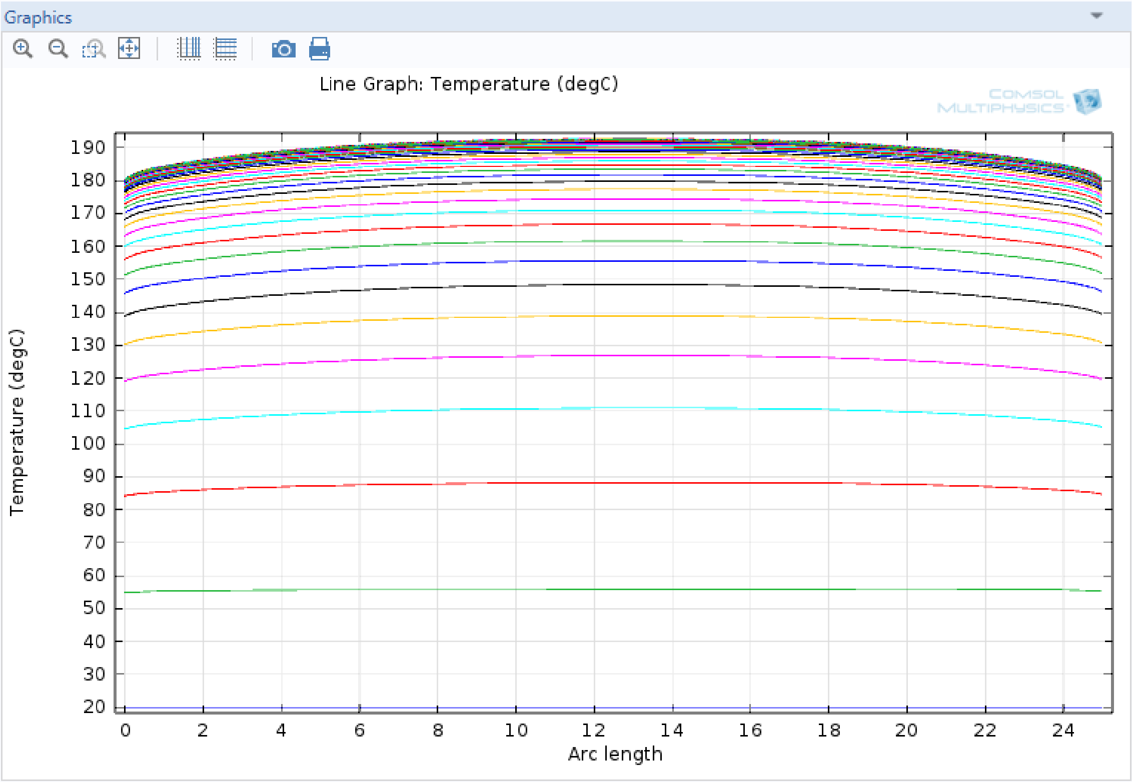

Fig. 6.11 Temperature distribution on the substrate surface with respect to time when heaters were kept constant at 400 °C

Previously, temperature calibrations were made empirically. For this calibration studies, one thermocouple was attached at the center and the other one was attached at the edge of the substrate surface via silver paste. In order not to detach from the surface, metallic weights were placed on top of these thermocouples. The earlier calibrations yielded in 217 and 198 °C when the heater temperatures were set to 400 °C for center and edge of the substrate, respectively. The comparison of empirical data and modeling results were tabulated in Table 6.2, below. Deviation was defined as the temperature difference from center to edge divided by maximum temperature on the surface.

Table 6.2 Temperature comparison of empirical data and modeling results

	T_{set} (°C)	T_{center} (°C)	T_{edge} (°C)	ΔT (°C)	Deviation
empirical	400	217	198	19	0.088
model	400	193	180	13	0.067

Approximately 20 °C difference in model and empirical data was observed. One of the reasons for higher observed temperatures was the local heating of silver paste with conduction. Silver paste might reduce the heat loss by direct radiation. In model, only assumed heat transfer mechanism was radiation. The second reason was the metallic weights, which might act as heat reflectors. The model gave quite reliable results while considering these reasons and also deviation values are similar.

6.2.2 Malfunction of Side Heater Case

The heaters are connected in parallel, which means if one collapses the others will still work. To illustrate substrate temperature distribution in different cases, firstly the heater at the right side has been turned off. The resulting thermal image of the chamber and the temperature distribution at the substrate surface at steady-state conditions were illustrated in figures 6.12 and 6.13, respectively.

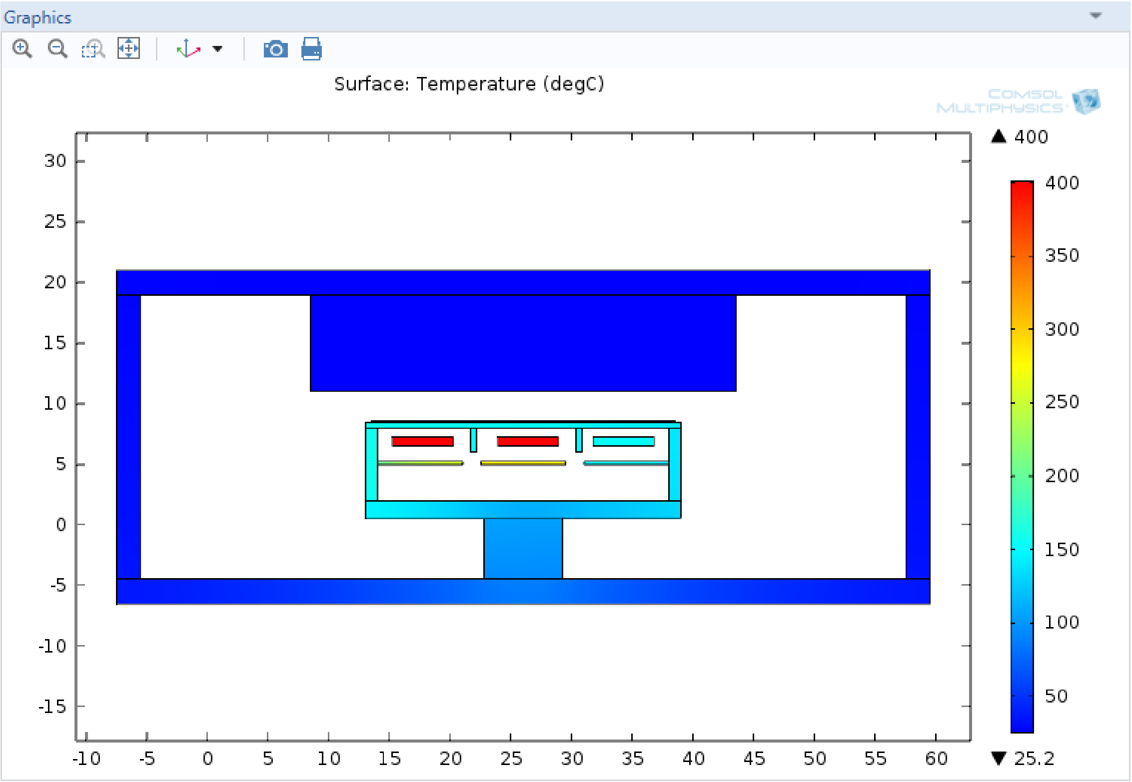

Fig. 6.12 Thermally colored CCP system at steady-state conditions when the heater at the right turned off

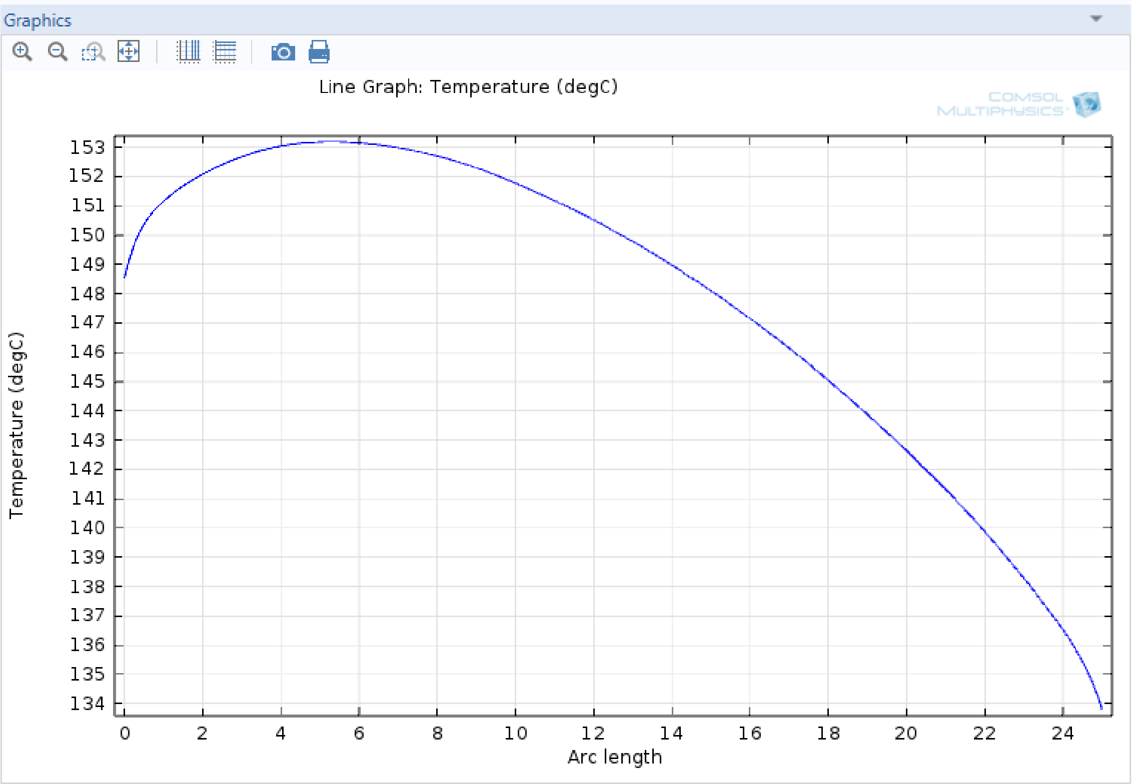

Fig. 6.13 Temperature distribution on the substrate surface when the heater at right side has turned off

6.2.3 Malfunction of Both Side Heaters Case

The second collapsing case was modeled with turning off both the side heaters at the same time. Only the center heater was working in this case. The resulting thermal image of the chamber and the temperature distribution at the substrate surface at steady-state conditions were illustrated in figures 6.14 and 6.15, respectively.

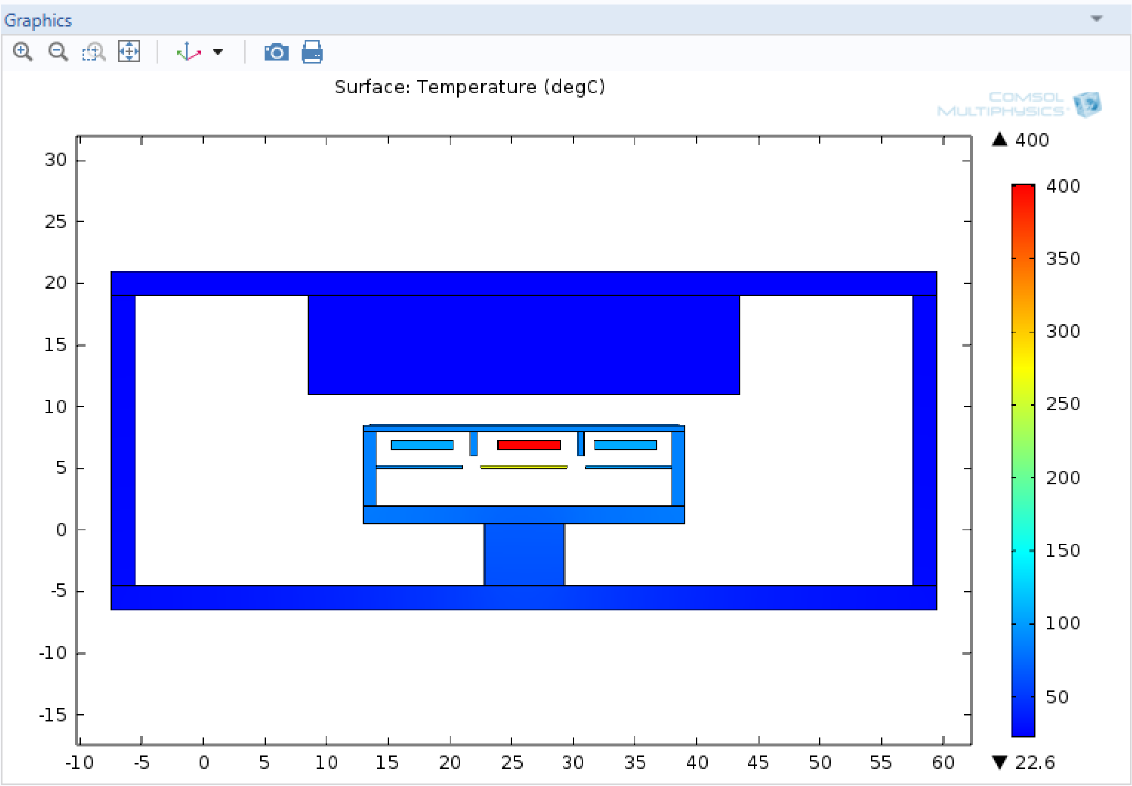

Fig. 6.14 Thermally colored CCP system at steady-state conditions when side heaters have turned off

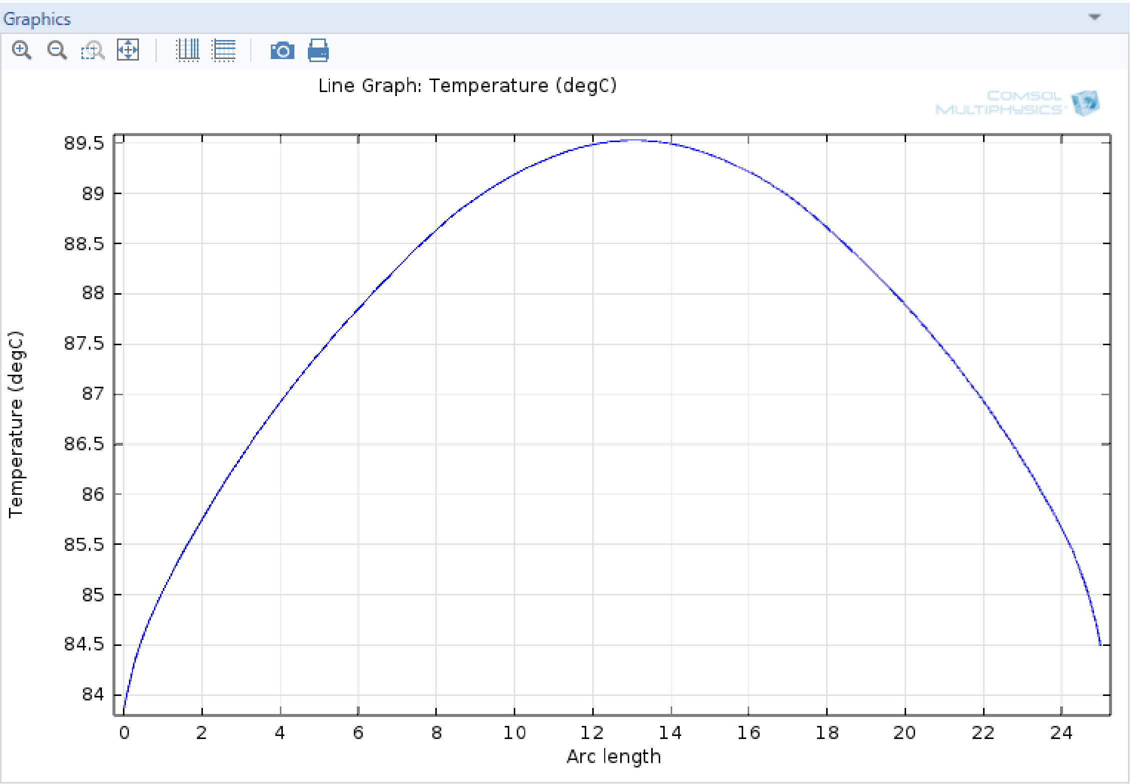

Fig. 6.15 Temperature distribution on the substrate surface when side heaters have turned off

6.2.4 Malfunction of Center Heater Case

The third and the last collapsing case was modeled with turning off only the center heater. The side heaters were working in this case. The resulting thermal image of the chamber and the temperature distribution at the substrate surface at steady-state conditions were illustrated in figures 6.16 and 6.17, respectively.

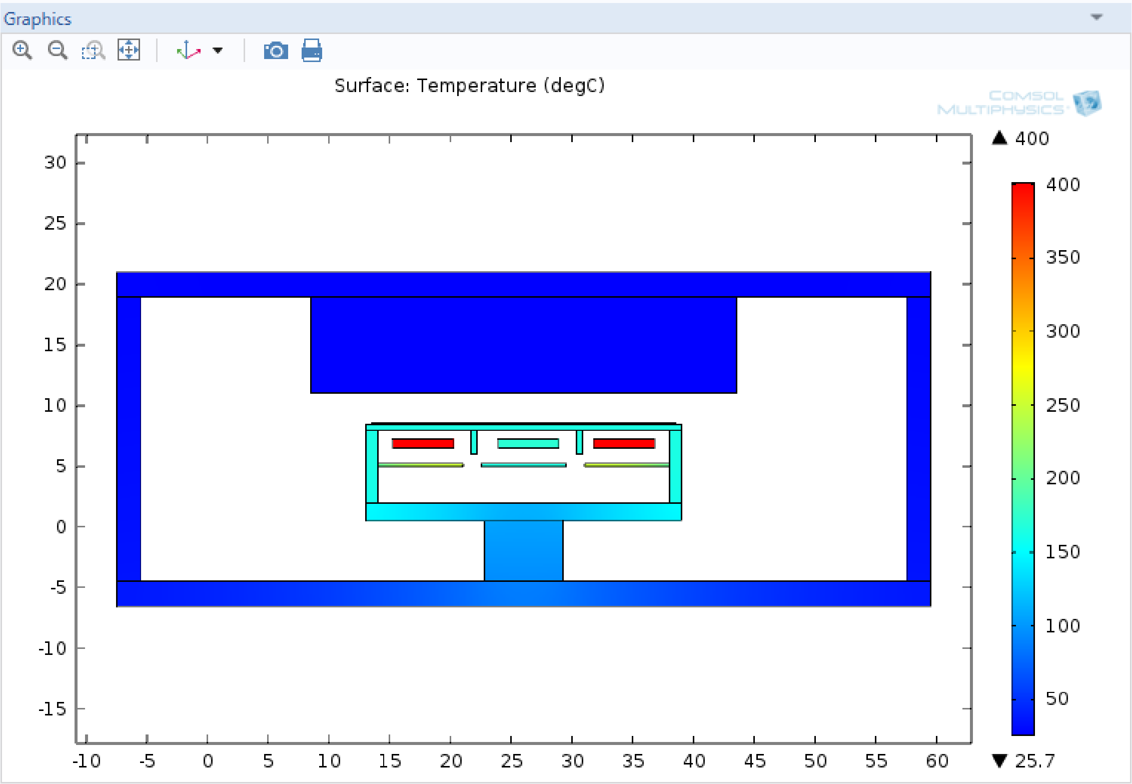

Fig. 6.16 Thermally colored CCP system at steady-state conditions when center heater has turned off

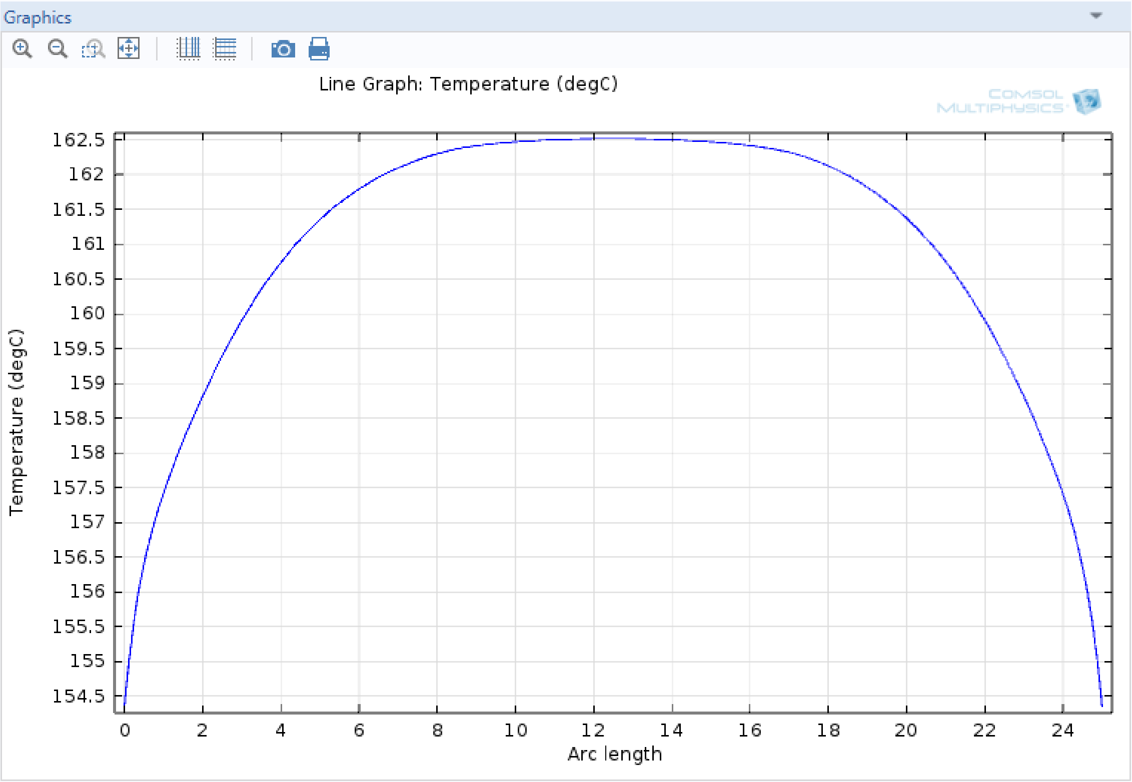

Fig. 6.17 Temperature distribution on the substrate surface when center heater has turned off

As a conclusion from the current CCP chamber analyses, it is obvious that the system cannot reach its technical specifications. Even reaching desired temperatures such as 200 °C is problematic at perfectly operating conditions. Therefore an improved design is necessary.

6.3 Proposed Design

In order to reach the required temperature levels, uniform substrate temperature and also 'hot wall' condition for the reactor, a new design is a necessity. For the proposed design, so-called plasma box concept and new heater specifications were taken into account. Moreover, change of the chamber geometry was minimized not to increase the investment cost.

6.3.1 Plasma Box

Contamination is one of the most vital problems in thin film depositions. Via ultra high vacuum (UHV) technologies that has a pressure value lower than 10^{-9} Torr, this problem is overcome. However, the production and operating costs of these machinery are so high. Another approach to eliminate contamination is the plasma box concept.

Plasma box is a small gas-tight enclosure in the reactor chamber. The process gases are only admitted to this box and they are separately pumped out. Outside of the plasma box is maintained at lower pressures. Due to this pressure gradient, plasma volume is not contaminated by impurities that are desorbed from reactor walls [2]. Another main advantage is by this box isothermal conditions on every wall can be reached easily, which lead to deposition uniformity and avoiding powder formation. The last but not the least advantage is reduction in the process gas consumption by decreasing the necessary plasma volume.

The comparison of a standard PECVD and plasma box can be found elsewhere [47,48] and schematically understood from Figure 6.18.

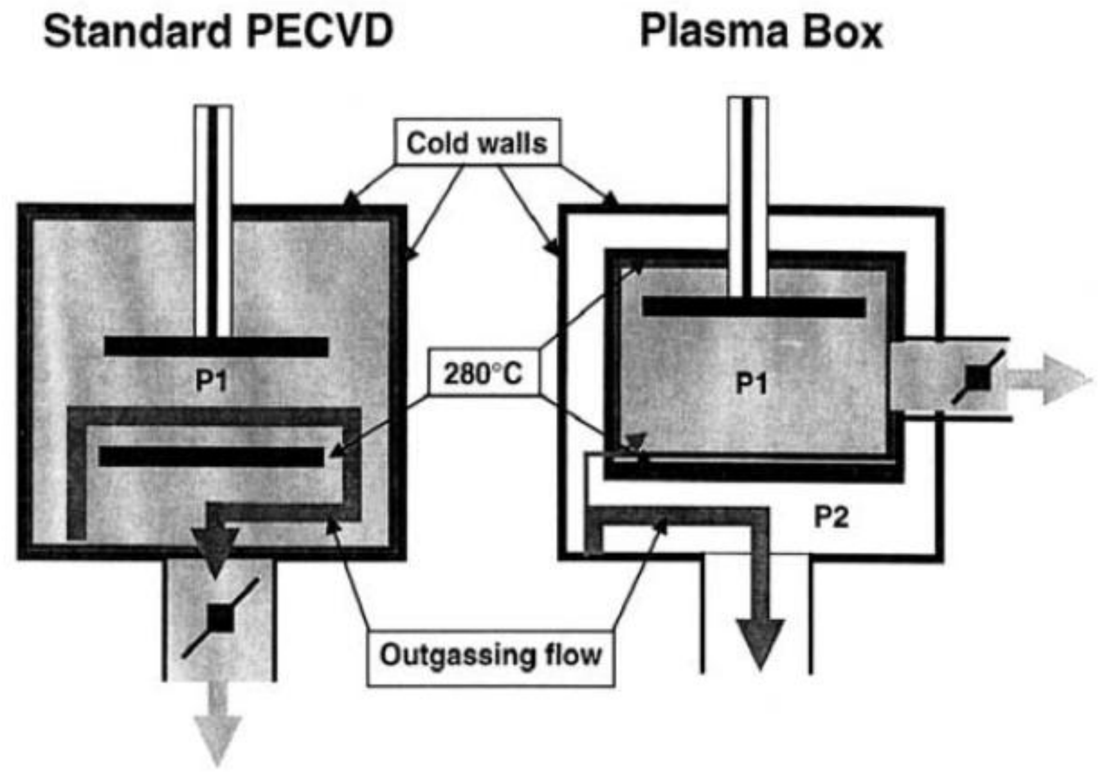

Fig. 6.18 Comparison of standard PECVD and Plasma Box in an illustrative manner [47]

6.3.2 Simulation of Proposed Design by COMSOL

The proposed design consists of extension of cathode sheath walls as a plasma box. The anode will be made mobile vertically. After the transfer of sample to the chamber, anode will place the sample inside of this proposed plasma box. Moreover, there will be two heaters; one placed on the anode in touch with substrate, one at the outer walls of plasma box. Thus heat transfer will be easier, faster and more uniform. However, not to interrupt the current sample transfer mechanism (i.e. transfer chamber, transfer gate valves, etc...), the chamber should be enlarged vertically around 10 cm.

First assumption while simulating the current system was to describe a simpler geometry that is mainly based on rectangular shapes. Then every parameter was described in the system in order to change the geometry just with changing these parameters which are tabulated in Table 6.3 below in units of cm.

Table 6.3 Geometrical parameters of proposed CCP system

Name	Expression	Value	Description
ts	0.11	0.110	thickness of substrate
ws	25	25.000	width of substrate
ha	3	3.000	height of anode
wa	ws+2	27.000	width of anode
hsh	22	22.000	height of shaft
wsh	4	4.000	width of shaft
hw	ha+1	4.000	height of wall
ww	0.3	0.300	width of wall
op	0.2	0.200	opening of box
wh	1	1.000	width of heater
hh	hw	4.000	height of heater
hc	6	6.000	height of cathode
wc	wa+2*op+2*ww	28.000	width of cathode
hup	2	2.000	height of upper wall
wup	50	50.000	width of upper wall
hsw	hc+hw+hsh	32.000	height of side wall
wsw	2	2.000	width of side wall
wah	1	1.000	width of anode heater
hah	1	1.000	height of anode heater
ope	(ws-8*wah)/9	1.889	opening between anode heaters
Qs	1500	1500.000	power of side wall heater
Qh	1000	1000.000	power of anode heater

After defining the parameters, the resulting geometry was obtained as seen in Figure 6.19. The enclosure or the chamber walls and the shaft were defined as stainless steel; anode, cathode and heat reflectors as aluminum; heaters as alumina and substrate as silica glass. These materials are available in COMSOL's material library.

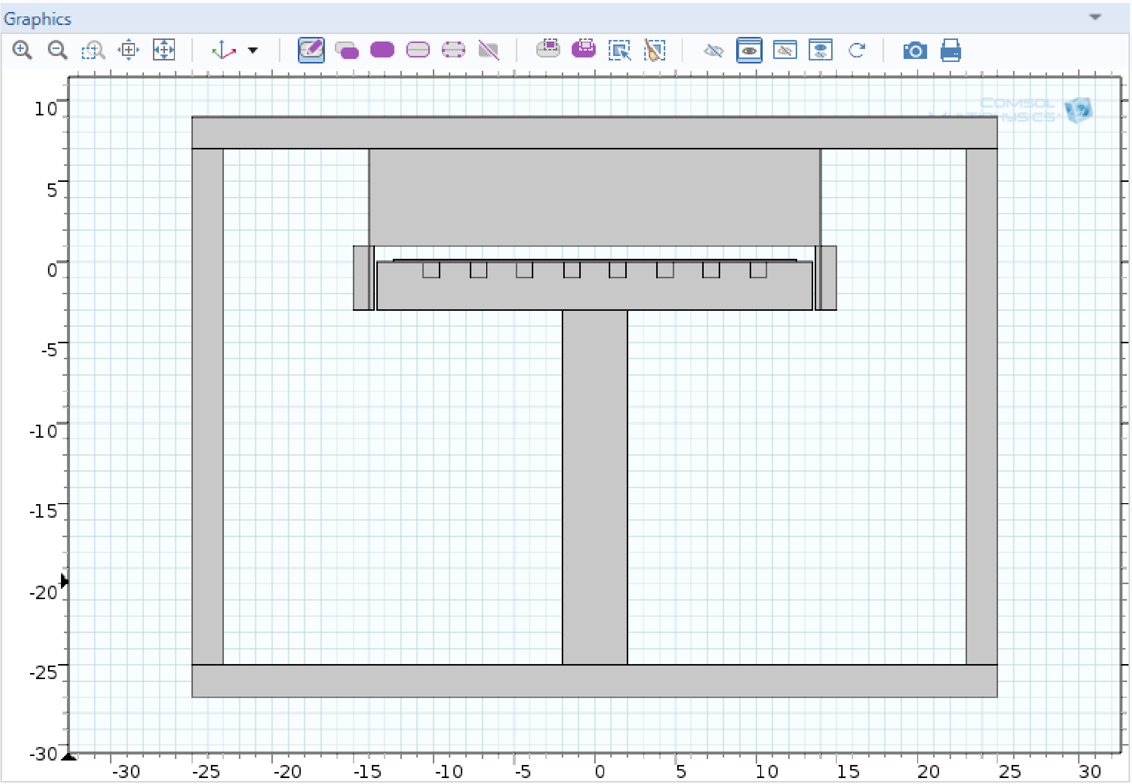

Fig. 6.19 Geometry for proposed CCP system

6.3.2.1 High Power Anode & Moderate Power Plasma Box Heater Case

In order to figure out the optimum heater power conditions in terms of uniform heating of every wall and substrate, desired temperature levels and minimum heating times; firstly anode heater and plasma box wall heater powers were set to 3000 and 1000 W, respectively.

First conclusion was that there was no convergence for steady state, which means the temperature gets as high as possible with time. Therefore a time dependent study was computed. It was observed that substrate reaches 400 °C in 45 minutes. However, as seen from Figure 6.20, the walls of the plasma box and cathode did not heat up as fast for this configuration.

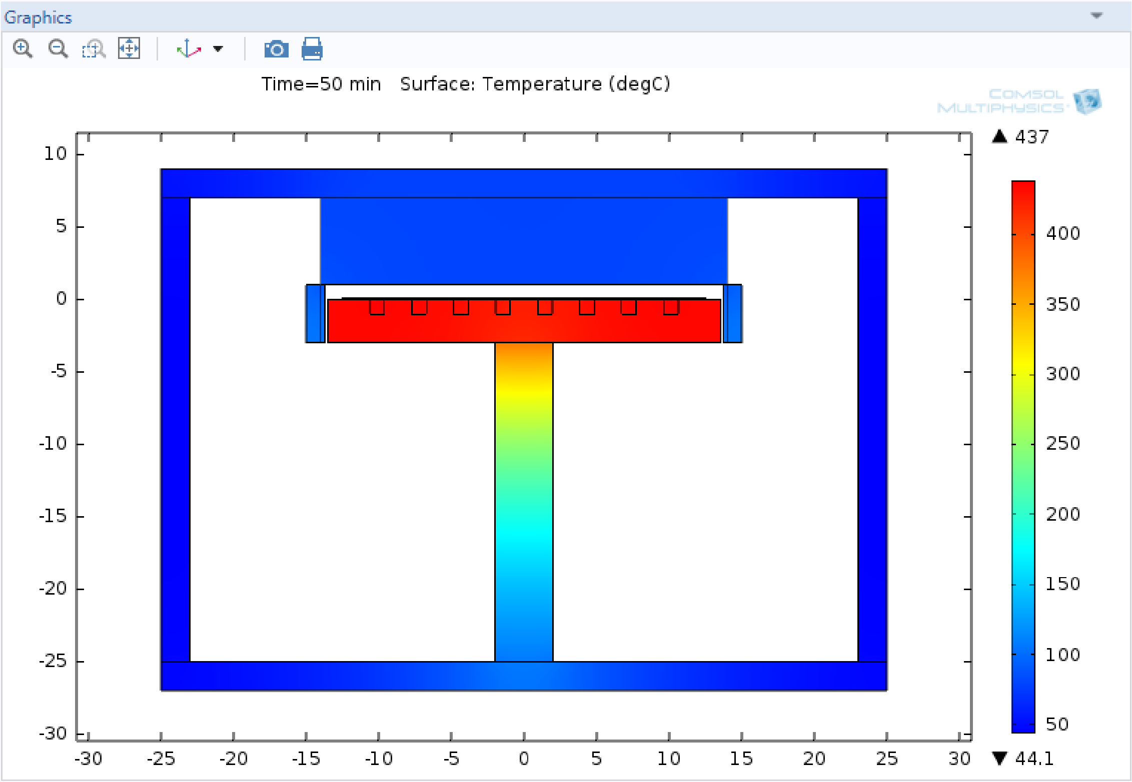

Fig. 6.20 Thermally colored proposed CCP system after 50 min for high power anode heater case

Substrate temperature distribution for the first 50 minutes were plotted in Figure 6.21. As seen from the plot, in each 10 minute interval, surface temperature increases approximately 50 °C.

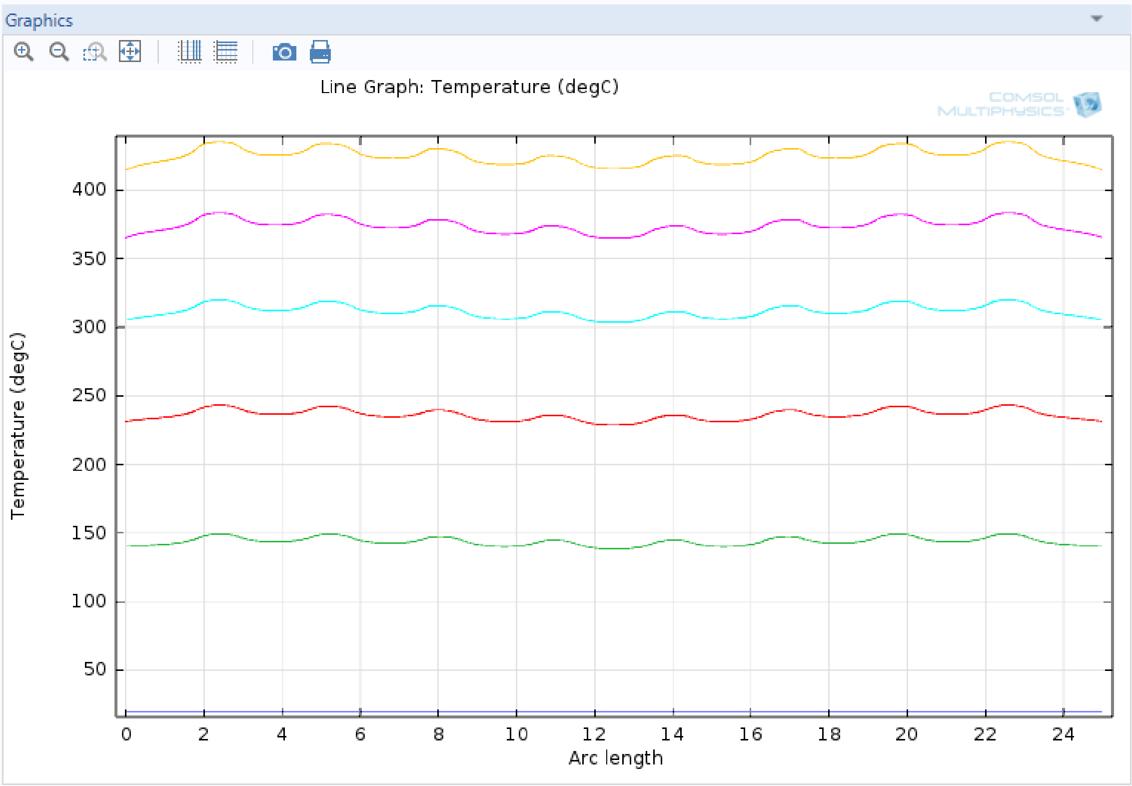

Fig. 6.21 Temperature distribution on the substrate surface with respect to time of proposed design for high power anode heater case

6.3.2.2 Moderate Power Anode & High Power Plasma Box Heater Case

As a second case, just the opposite power configuration was studied. Anode heater and plasma box wall heater powers were set to 1000 and 3000 W, respectively. From Figure 6.22, it is obvious that at high wall heater power levels, overheating of the chamber takes place. Especially, over heating of the cathode may cause problems due to rubber connections (i.e. o-rings) on top of the cathode. Therefore, as a conclusion, wall heaters should be low in terms of power.

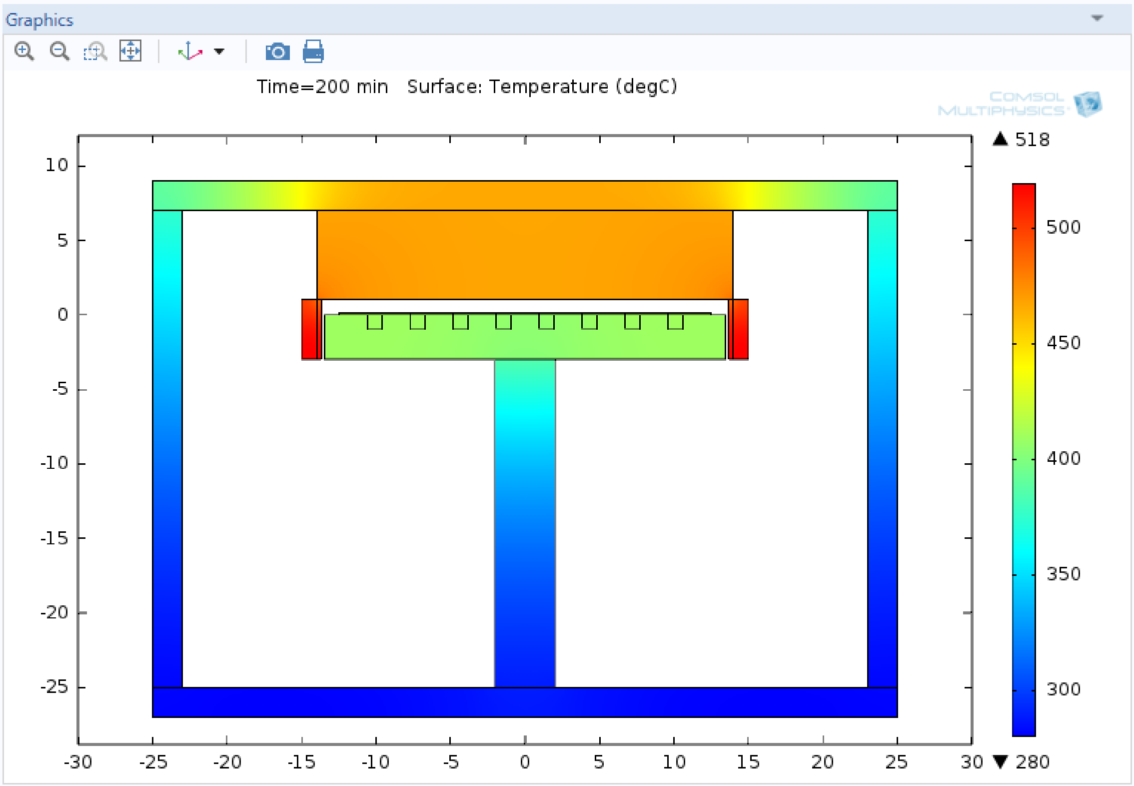

Fig. 6.22 Thermally colored proposed CCP system after 200 min for high power plasma box heater case

400 °C levels on the substrate was observed after 200 minutes as plotted in Figure 6.23. The temperature uniformity for this case is so fine. The temperature difference from edge to center is just 10 °C.

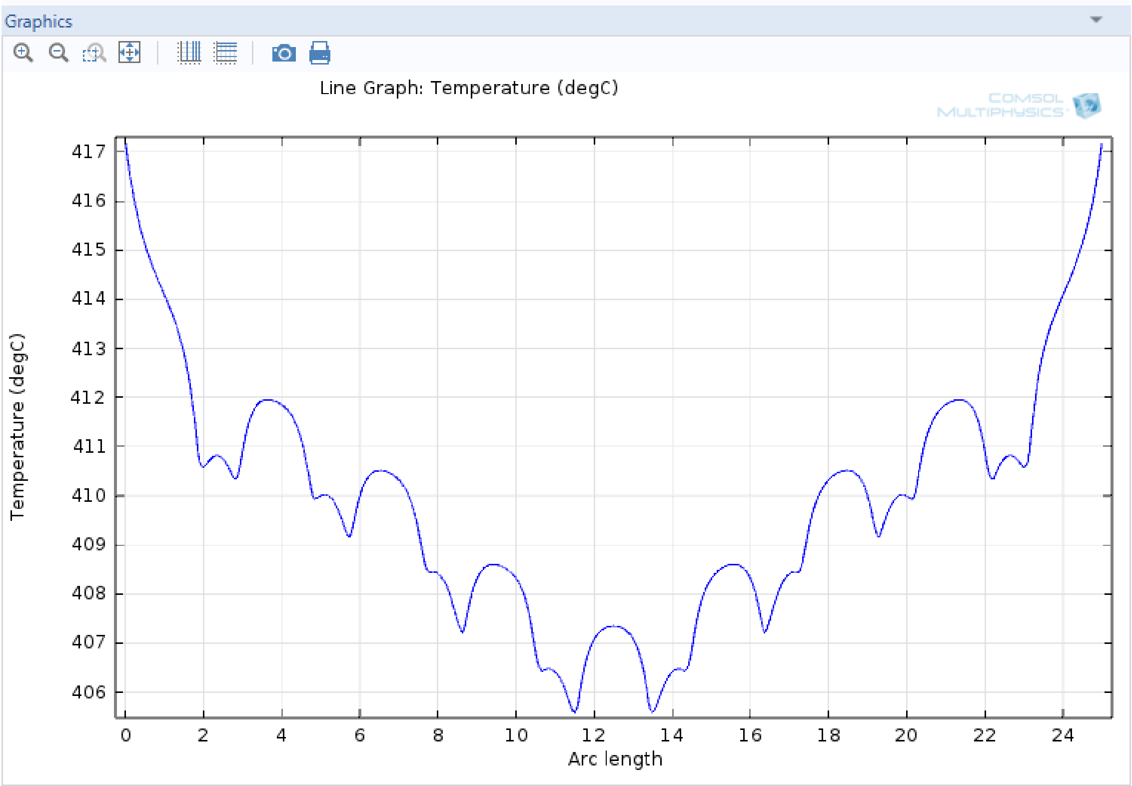

Fig. 6.23 Temperature distribution on the substrate surface of proposed design for high power plasma box heater case

6.3.2.3 Optimum Heater Powers in Terms of Uniform Temperature Distribution and Heating Duration

As a third configuration plasma box wall heater power was decreased to 2000 W, whereas anode heater power was kept constant at 1000 W. However, the substrate reached 400 °C after 4 hours. Therefore both powers were multiplied by 1.5 to have 1500 W for anode heater and 3000 W for plasma box heaters. 400 °C of substrate temperature was reached after 130 minutes. Typically, the deposition temperatures for photovoltaic applications are around 200 °C that could be obtained in 40 minutes as seen in Figure 6.24. However, again excessive heating of cathode problem has been encountered.

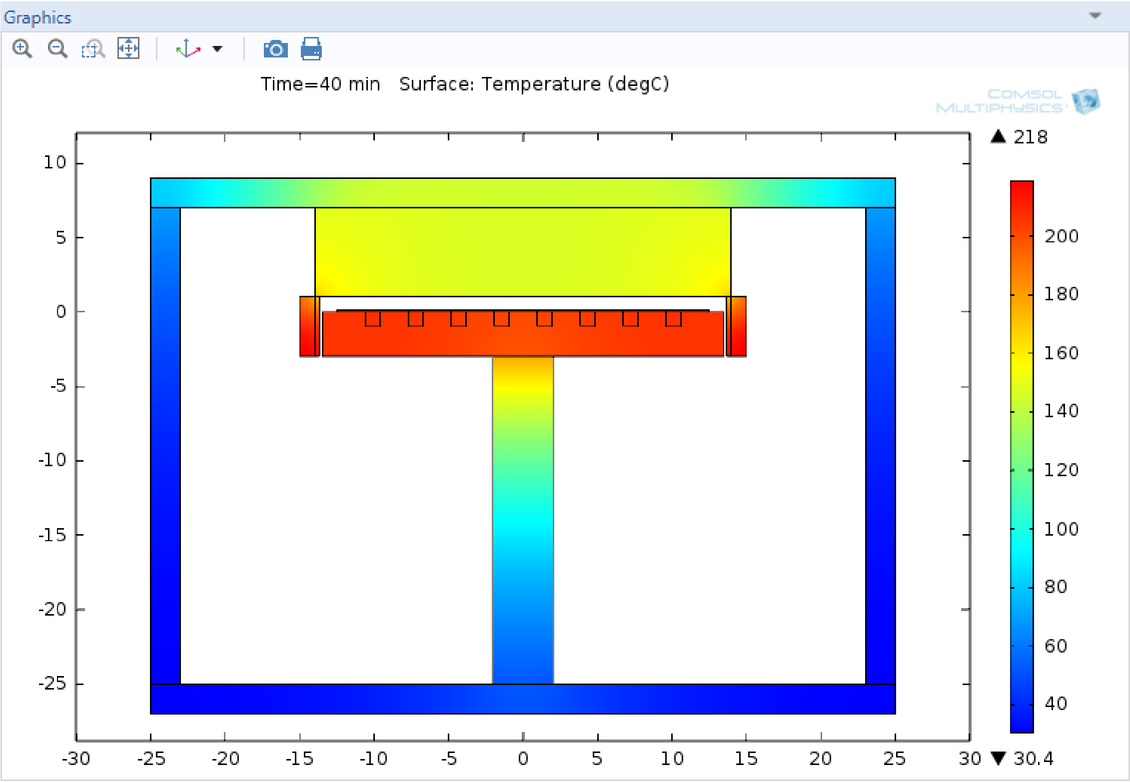

Fig. 6.24 Thermally colored proposed CCP system after 40 min for optimum case

Temperature distribution on the surface for this case after 40 minutes can be visualized from Figure 6.25. The temperature uniformity for this case is so fine even without stabilization of temperature. The temperature difference from edge to the center is only 8 °C.

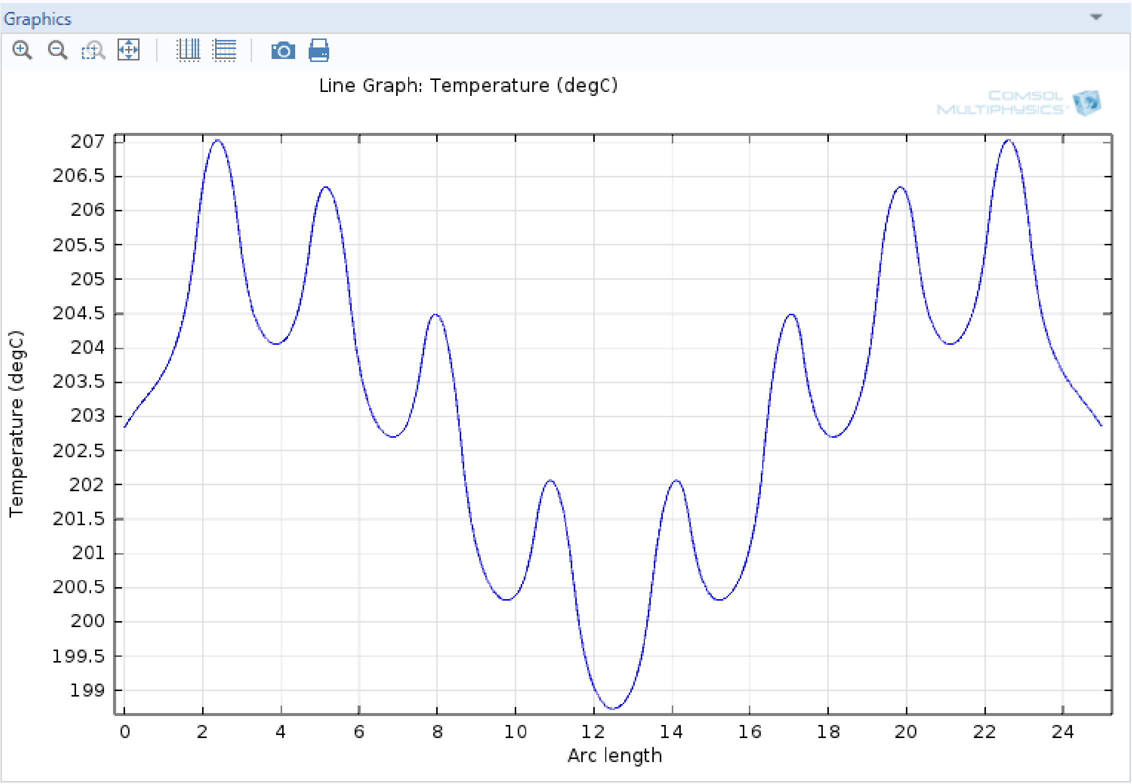

Fig. 6.25 Temperature distribution on the substrate surface of proposed design for case 3 after 40 minutes

The temperature distribution of cathode wall facing vacuum after 40 minutes was plotted in Figure 6.26. It is clearly seen that the temperatures cannot reach 200 °C levels as fast as substrate. Setting the heaters to fixed values and a little more time is necessary for the complete thermal equilibrium.

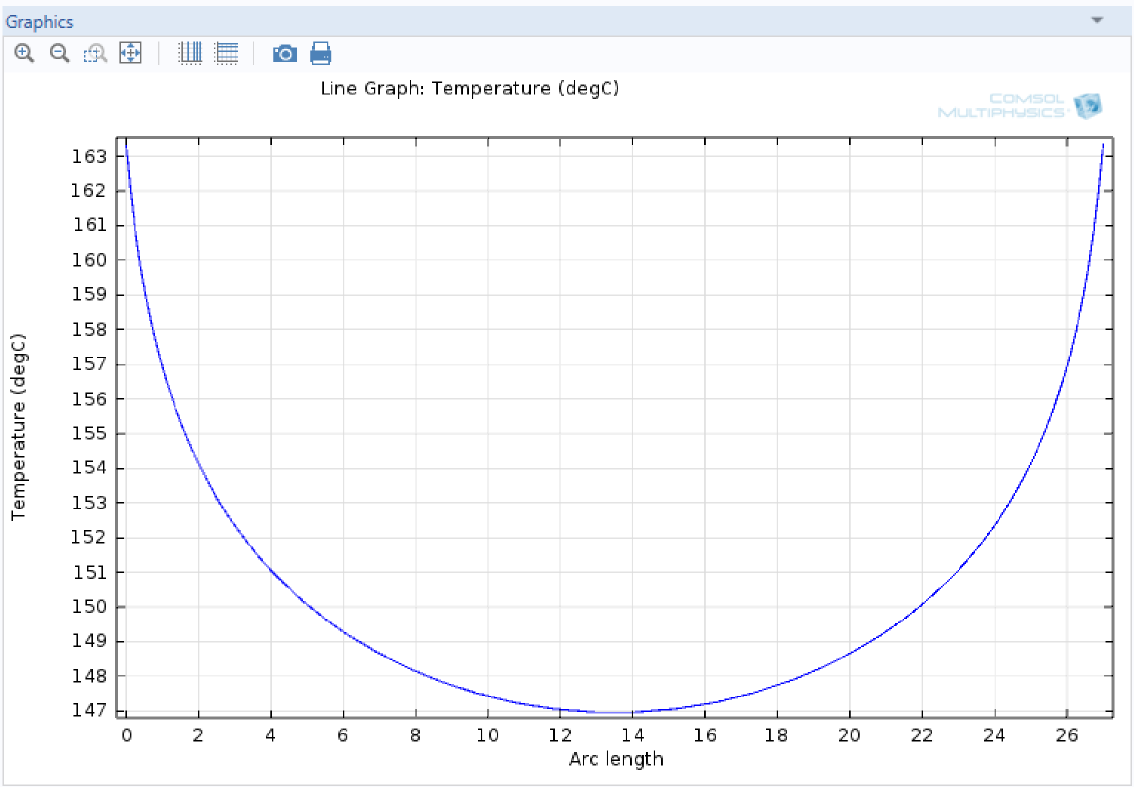

Fig. 6.26 Temperature distribution on the cathode wall of proposed design for optimum case after 40 minutes

If both heater temperatures were kept constant at 200 °C, cathode wall temperature increased rapidly from 10 to 50 minutes as seen from Figure 6.27. While heaters reach 200 °C, the cathode wall already reach values around 160 °C, so 10 minutes of duration will be enough for thermal equilibrium on every wall of the so-called plasma box.

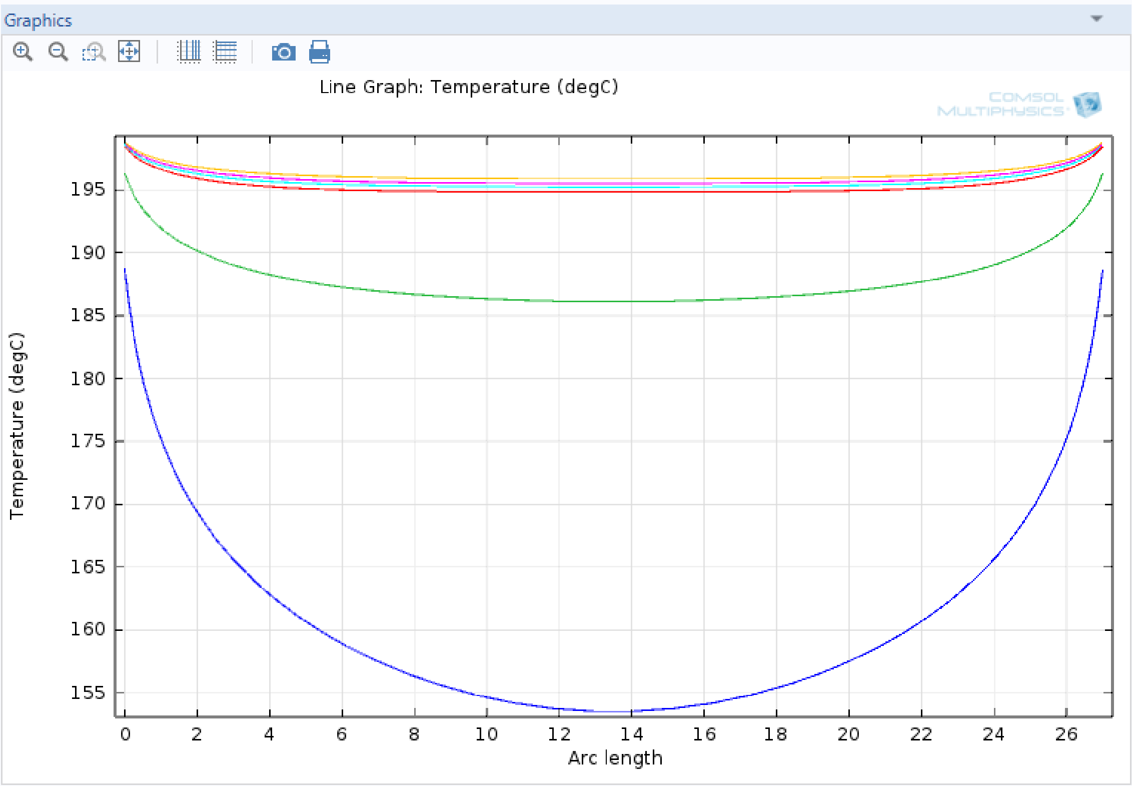

Fig. 6.27 Temperature distribution on the cathode wall of proposed design when heaters were kept constant at 200 °C for 40 minutes

Another approach for this case was to heat up the plasma box before placing the sample inside of the chamber. Idle times will be reduced with this approach. If heaters were kept constant at 200 °C and substrate placed on top of anode initially at 20 °C, thermal equilibrium is reached in 10 minutes. The temperature distribution on the substrate surface can be seen in Figure 6.28. It is clear that the uniformity is perfect.

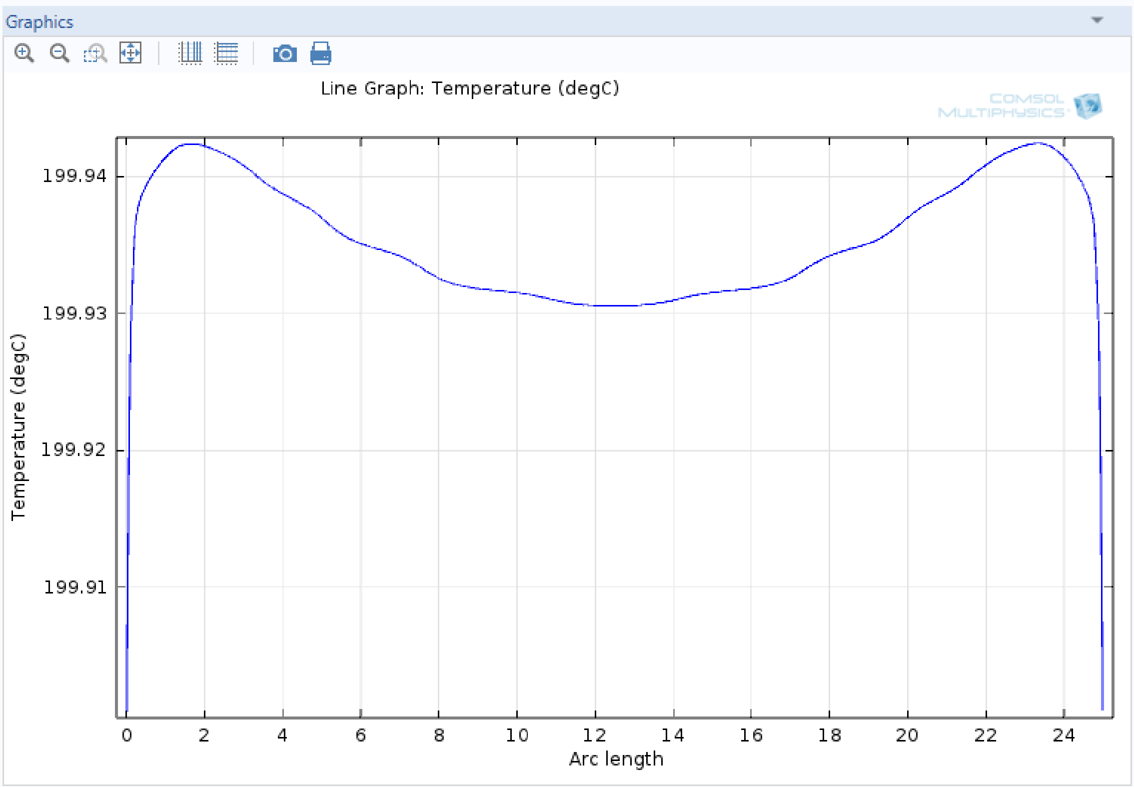

Fig. 6.28 Temperature distribution on the substrate surface of proposed design when substrate was initially at room temperature and then heated for 10 minutes

6.3.2.4 Thermal Insulator Addition to The Optimum Design

Proposed design in previous case computed to work properly in terms of high temperature levels, uniform temperature distribution and low heating periods. However, excessive heating of cathode cannot be avoided. Therefore a thermal insulating plate was also placed on top of cathode in that design. Selection of the insulating material takes the most important role in this design. First, alumina that has 27 W/m.K thermal conductivity was considered. However, its thermal conductivity was not low enough for this system. Silica glass that has a thermal conductivity of 1.38 W/m.K was found out to be a more proper material. The only problem of silica is that its softening point is around 500-600 °C. Therefore careful heating should be done. Processing and availability of both materials are easy, so silica was selected as the thermal insulating layer.

Placing a 1 cm thick silica on top of the cathode overcome the problem as seen in figures 6.29 and 6.32. In Figure 6.29, time limit to reach 200 °C was confirmed to be 40 minutes again. The insulator has no negative effect on heating duration. However, the temperature uniformity of the plasma box has slightly deterioted for immediate heating up.

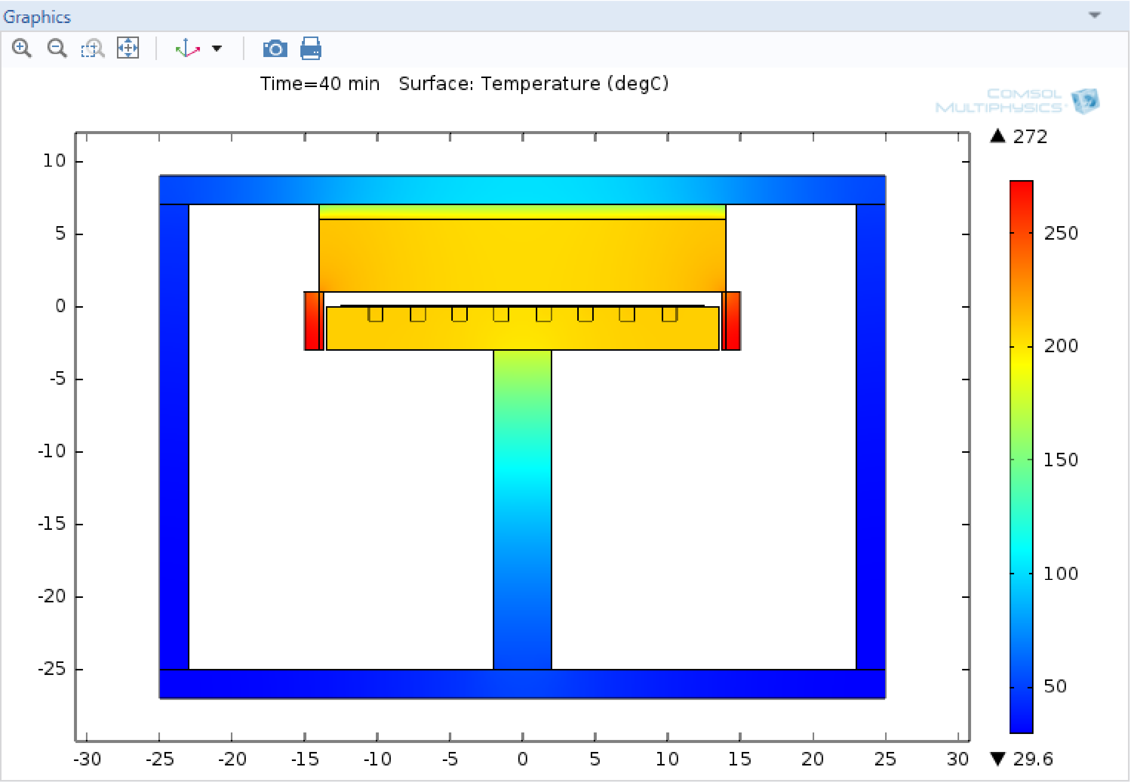

Fig. 6.29 Thermally colored proposed CCP system with thermally insulating layer after 40 minutes

The temperature distribution on the substrate surface after 40 minutes of heating up is plotted in Figure 6.30, below. As all of the proposed cases, the temperature uniformity is so fine.

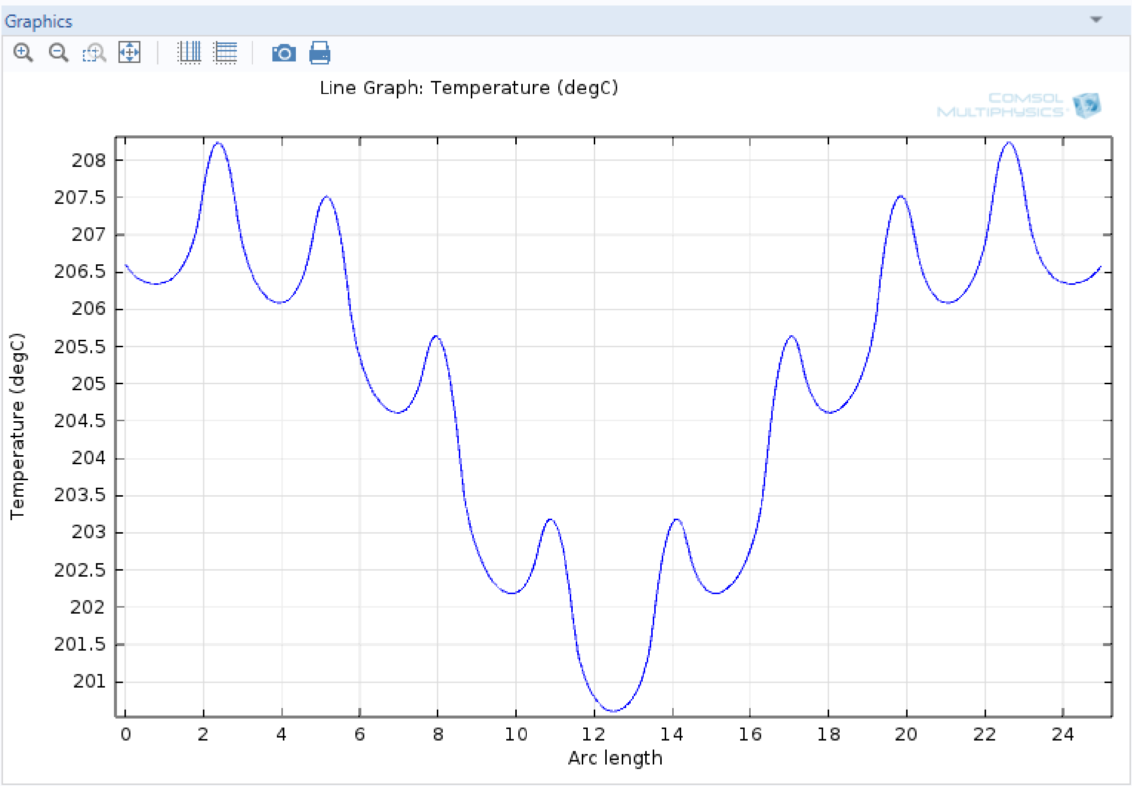

Fig. 6.30 Temperature distribution on the substrate surface of proposed design with addition of insulating layer after 40 minutes

In Figure 6.31, the temperature distribution at the cathode wall facing the vacuum was plotted. It was computed to be slightly higher than the case without thermal insulator as expected.

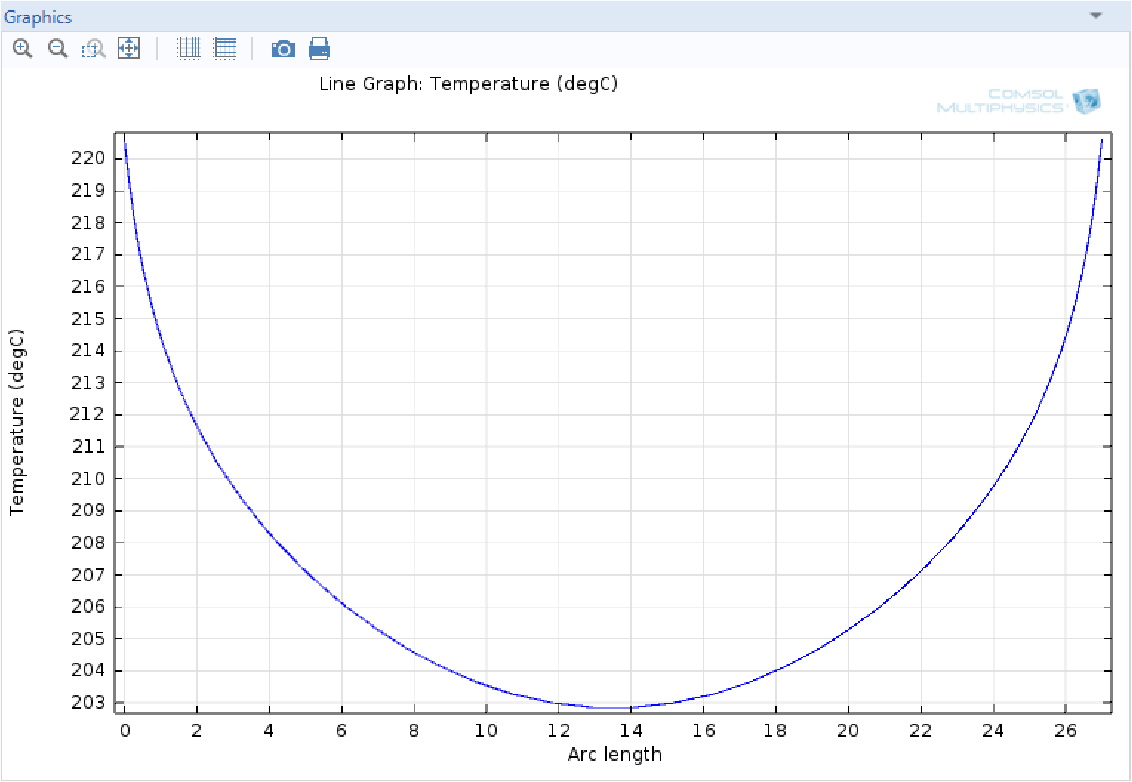

Fig. 6.31 Temperature distribution on the cathode wall of proposed design with addition of insulating layer after 40 minutes

If both heaters were set to 200 °C, the resulting thermal image of Figure 6.32 was observed. It can be concluded from this figure that the temperature uniformity of the plasma box is so fine after 10 minutes. Moreover, thermal insulator avoids excessive heating of upper parts of cathode.

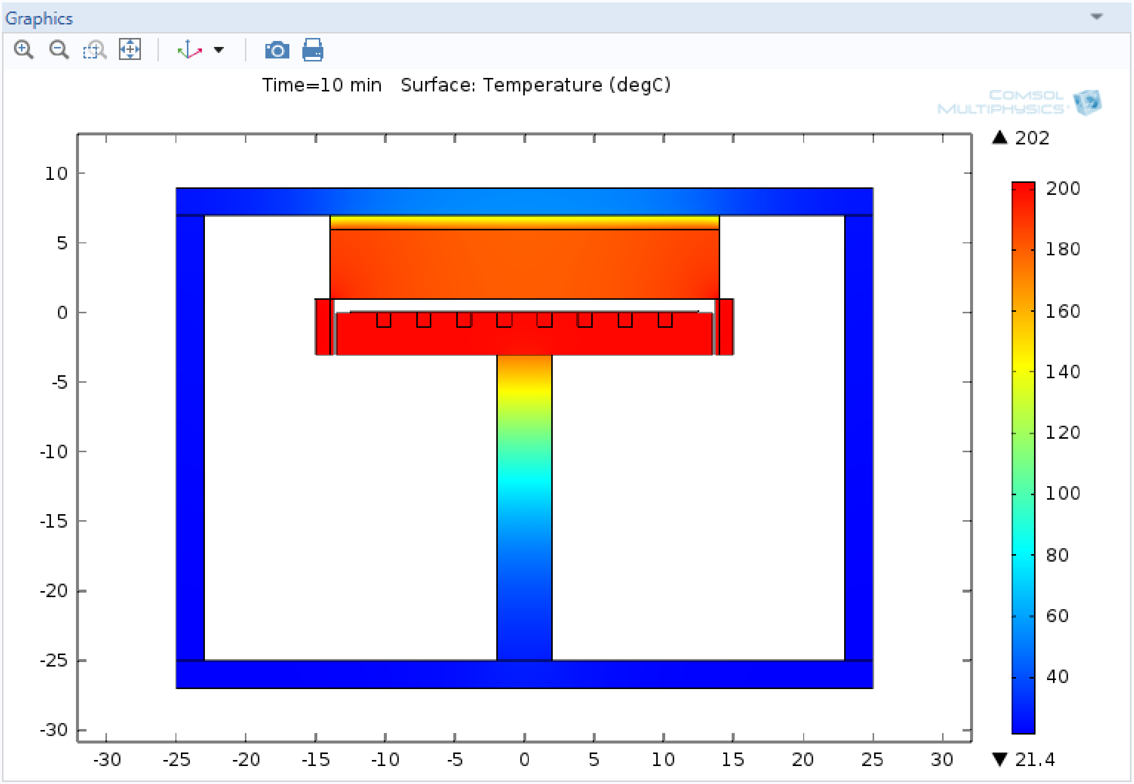

Fig. 6.32 Thermally colored proposed CCP system with thermally insulating layer after 10 minutes when both heaters were kept constant at 200 °C

The temperature distribution on the substrate surface when heaters were kept constant at 200 °C is plotted in Figure 6.33. It is clearly seen that there is no temperature gradient on the surface.

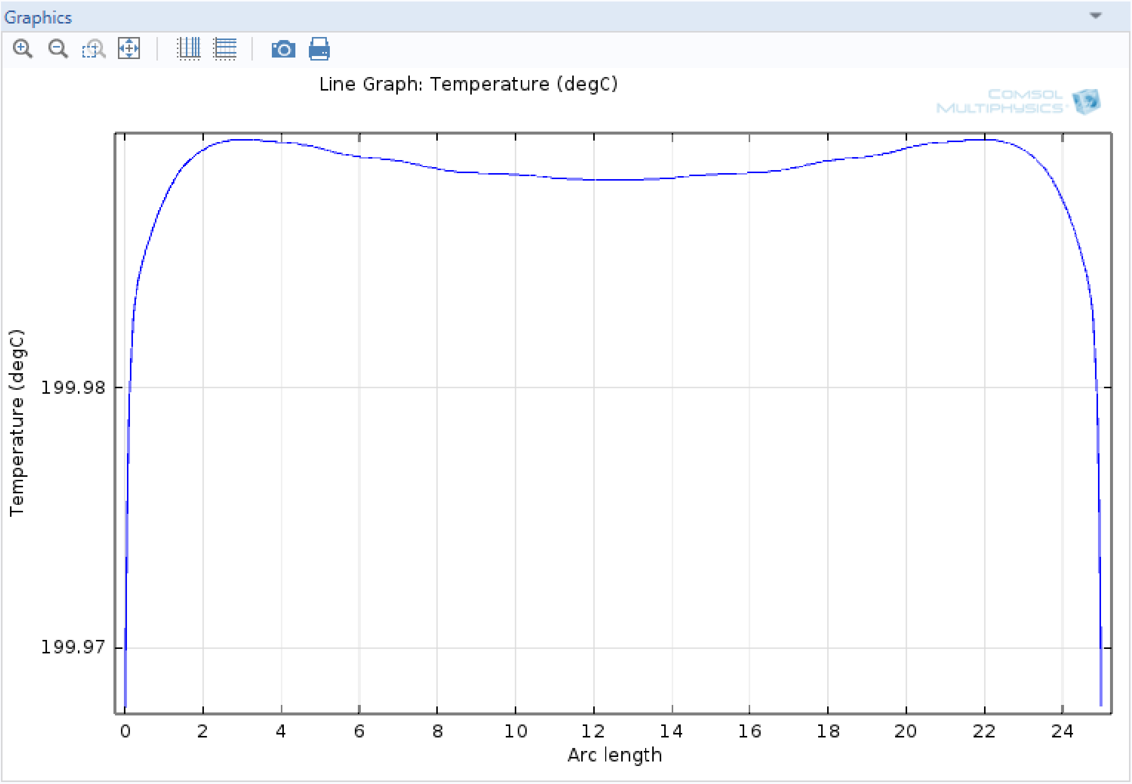

Fig. 6.33 Temperature distribution on the substrate surface of proposed design with thermally insulating layer after 10 minutes when both heaters were kept constant at 200 °C

The temperature distribution on the cathode wall facing vacuum when heaters were kept constant at 200 °C was plotted in Figure 6.34 with respect to time. The interval between curves is 10 minutes. It is clearly seen that the temperature uniformity gets finer with increasing duration. On the other hand 20 minutes seems to be fine enough.

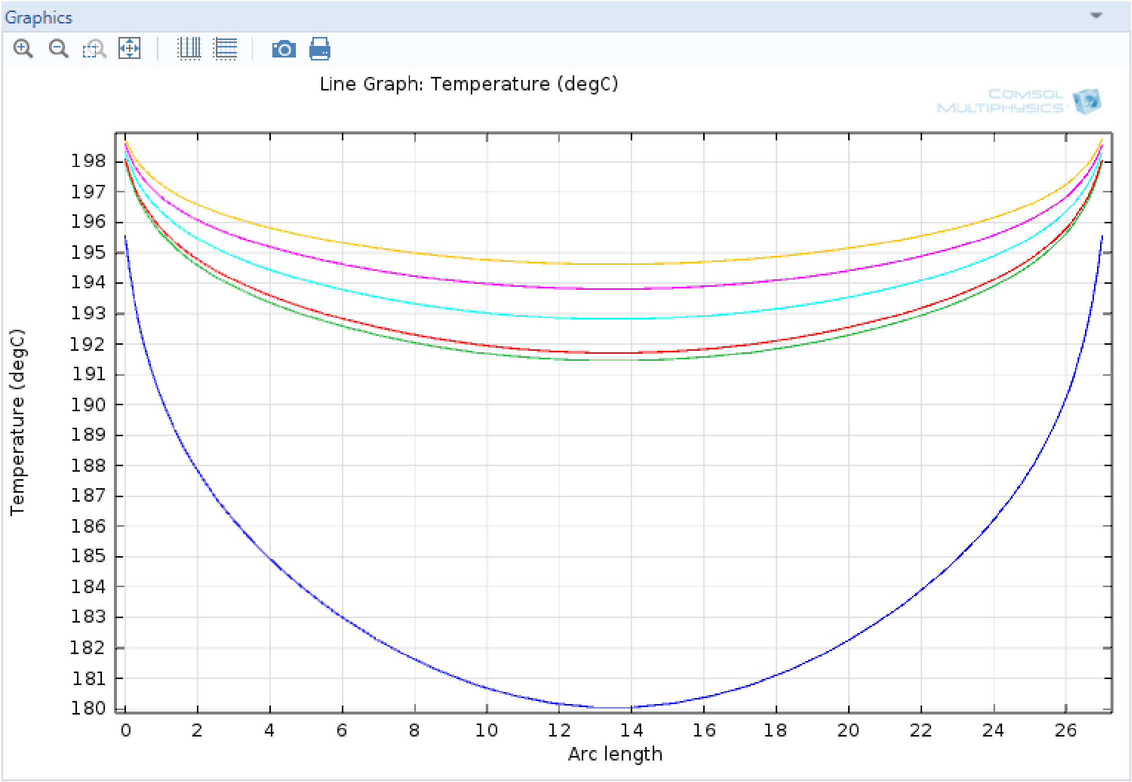

Fig. 6.34 Temperature distribution on the cathode wall of proposed design with thermally insulating layer when both heaters were kept constant at 200 °C with respect to time

6.3.2.5 Conclusion

To conclude, the proposed design will include a so-called plasma box. This box will be heated with 3 kW capacity heater from side walls. Another heater will be placed on top of anode that is in contact with the substrate and has a power capacity of 1500 W. To overcome excessive heating of RF power connectors, gas lines and etc. 1 cm thick silica will be attached at the top side of cathode. However, the current geometry should be changed. To avoid changes in transfer mechanisms, the chambers should be 10 cm higher and the anode part should be mobile.

CHAPTER 7

CONCLUSION

In 2010, GÜNER system was started to be installed into GÜNAM laboratories. In 2011, GÜNER system was completely handed over to GÜNAM engineers. Since then personnel trainings were completed. Each chamber's operation conditions were optimized in terms of deposited material qualities, temperature calibrations, substrate heating standards, plasma cleaning procedures and interactions with other systems such as hydraulic oxidation system, gas lines and cabinet, compressors, DI water production unit, and etc.

In GÜNER, the growth of silicon thin films in amorphous, nano-crystalline and micro-crystalline phases with intrinsic, n- and p- doping types, amorphous silicon nitride (SiN_x) thin films with tunable silicon and nitrogen concentration, silver thin films with controlled thickness profile down to nm scale, aluminum doped zinc oxide (AZO) thin films with repeatable uniform conductivity were achieved successfully.

The main purpose of GÜNER is to produce photovoltaic devices composed of mainly amorphous and microcrystalline p-i-n structured homojunction and heterojunction solar cells. The efficiency values of 2.9 % (initial) for a-Si:H p-i-n structured solar cells, 15.9 % for heterojunction solar cells and 12.5 % for one sided HIT structured solar cells were achieved.

In this work, a first principles based thermal model of the PECVD system was constructed, guiding the design of an improved chamber delivering better substrate temperature levels and uniformity.

Also, owing to the suitable design of GÜNER, silver nano-particle deposition for plasmonic effect studies, silicon solar cells on flexible substrates, silicon nitride for electrical passivation and buffer layer applications are within the scope of GÜNAM.

REFERENCES

[1] Nelson, J., The Physics Of Solar Cells, Imperial College Press, London, (2003).

[2] Shah, A., Thin-Film Silicon Solar Cells, EPFL Press, Italy, (2010).

[3] Kazmerski L.L., Solar photovoltaics R&D at the tipping point; A 2005 technology overview, Journal of Electron Spectroscopy and Related Phenomena, 150, 105-135, (2006).

[4] Fahrner W. R., Amorphous Silicon / Crystalline Silicon Heterojunction Solar Cells, Springer, Chemical Industry Press, 2013, Beijing

[5] Konuma, M., Film Deposition by Plasma Techniques, Springer-Verlag, New York , (1992).

[6] Carlson D.E., Wronski C.R., Appl. Phys. Lett. 28 (1976) p. 671-673.

[7] Staebler D.L., Wronski C.R., "Reversible conductivity changes in discharge-produced amorphous Si", Appl. Phys. Lett. 31, 292–294 (1977)

[8] Hamakawa Y., Okamoto H., Nitta Y., Appl. Phys. Lett. 35(2) (1979), p. 187-189.

[9] Kuwano Y., Imai T., Ohnishi M., Nakano S., in Proceedings of the 14th IEEE Photovoltaic Specialist Conference (1980), p. 1402.

[10] Tawada Y., Okamoto H., Hamakawa Y., *Appl. Phys. Lett.* **39**(3) (1981), p. 237-239

[11] Nakamura G., Sato K., Yukimoto Y., Shirahata K., in *Proceedings of the 3rd E.C. Photovoltaic Solar Energy Conference* (1980), p. 835.

[12] Deckman H.W., Wronski C.R., Witzke H., Yablonovitch E., *Appl. Phys. Lett.* **42**(11) (1983), p. 968.

[13] Meier J., Dubail S., Flückiger R., Fischer D., Keppner H., Shah A., in *Proceedings of the 1st World Conference on Photovoltaic Energy Conversion* (1994), p.409-412.

[14] J. Meier, S. Dubail, J. Cuperus, U. Kroll, R. Platz, P. Torres, J.A. Anna Selvan, P. Pernet, N. Beck, N. Pellaton Vaucher, Ch. Hof, D. Fischer, H. Keppner, A. Shah, *J. Non-Cryst. Solids* **227-230** (1998) 1250-1256.

[15] Yamamoto K., Yoshimi M., Tawada Y., Okamoto Y., Nakajima A., *J. Non-Cryst. Solids* **266-269** (2000) 1082-1087.

[16] Grigorovici R, Croitoru N, Teleman E, Marina M (1965) Rev Roum Phys 10:641–659

[17] Grigorovici R, Croitoru N, Marina M, Nastase L (1968) Heterojunctions between amorphous Si and Si single crystals. Rev Roum Phys 13:317–325

[18] Jayadevaiah T, Busmundrud O (1972) Amorphous-crystalline silicon junctions. Electron Lett 8:75–77

[19] Fuhs W, Niemann K, Stuke J (1974) Heterojunctions of amorphous silicon and silicon single crystals. Bull Am Phys Soc 19:345–350

[20] Nozagi H, Hatayama T, Ito H, Ide K, Nakagawa M (1984) Amorphous Si/ribbon Si tandem type solar cell. In: Proceedings of the PVSEC-1, Kobe

[21] Tanaka M, Taguchi M, Matsuyama T, Sawada T, Tsuda S, Nakano S, Hanafusa H, Kuwano Y (1992) Development of new a-Si/c-Si heterojunction solar cells: ACJ-HIT (artificially constructed junction-heterojunction with intrinsic thin-layer). Jpn J Appl Phys 31:3518–3522

[22] Green M.A., Emery K., Hishikawa Y., Warta W., Dunlop E.D., Solar Cell Efficiency Tables (version 45), Prog. Photovolt: Res. Appl. 2015; **23**: 01-09

[23] Panasonic Solar, http://eu-solar.panasonic.net/fileadmin/user_upload/downloads/technical_documents/VBHN245SJ25_PEWEU_EN.pdf, last visited on January 2015

[24]National Renewable Energy Laboratory (NREL), http://www.nrel.gov/ncpv/images/efficiency_chart.jpg, last visited on January 2015

[25] Roth, J.R., Industrial Plasma Engineering, Vol. I, IOP Publishing, London, (2000).

[26] Özkol, E., Production of Boron Nitride, Ms. Thesis (2008).

[27] Song G., Method for Cleaning Textured Silicon Wafers, US Patent 0 252 427, September 26, 2013.

[28] Janotti A., Van de Walle C. G., Fundamentals of zinc-oxide as a semiconductor, Reports on Progress in Physics, 72, 2009, 126501, (29pp)

[29] Barquinha P., Martins R., Pereira L., Fortunato E., Transparent Oxide Electronics, 2012, John Wiley & Sons, Ltd., West Sussex, UK, p.10

[30] Fortunato E., Nunes P., Costa D., Brida D., Ferreira I., Martins R., Characterization of aluminium doped zinc oxide thin films deposited on polymeric substrates, Vacuum 64, 2000, 233-236

[31] Jeong S. H., Lee J. W., Lee S. B., Boo J. H., Deposition of aluminum-doped zinc oxide films by RF magnetron sputtering and study of their structural, electrical and optical properties, Thin Solid Films, 435, 2003, 78-82

[32] Rath J. K., Liu Y., de Jong M. M., de Wild J., Schuttauf J. A., Brinza M., Schropp R.E.I., Transparent conducting oxide layers for thin film silicon solar cells, Thin Solid Films, 518, 2010, e129-e135

[33] Igasaki Y., Kanma H., Argon gas pressure dependence of the properties of transparent conducting ZnO:Al films deposited on glass substrates, Applied Surface Science, 2001, 169-170, 508-511

[34] Kim H., Pique A., Horwitz J. S., Murata H., Kafafi Z. H., Gilmore C. M., Chrisey D. B., Effect of aluminum doping on zinc oxide thin films grown by pulsed laser deposition for organic light-emitting devices, Thin Solid Films, 2000, 377-378, 798-802

[35] Kroll U., Meier J., Shah A., Mikhailov S., Weber J., Hydrogen in amorphous and microcrystalline silicon films prepared by hydrogen dilution, Journal of Applied Physics 80, issue 9, 4971-4975, 1996.

[36] Yang H., Wu C., Huang J., Ding R., Zhao Y., Geng X., Xiong S., Optical Emission Spectroscopy Investigation on Very High Frequency Plasma and Its Glow Discharge Mechanism During The Microcrystalline Silicon Deposition, Thin Solid Films 472 (2005) 125-129

[37] Michigan State University Organic Chemistry, http://www.cem.msu.edu/~reusch/OrgPage/bndenrgy.htm, last visited on January 2015.

[38] Nogay G., Özkol E., Ilday S., Turan R., Structural Peculiarities and Aging Effect in Hydrogenated a-Si Prepared by Inductively Coupled Plasma Chemical Vapor Deposition System (ICP-CVD), Vacuum, Volume 110, 2014, 114-120.

[39] Droz C., Vallat-Sauvain E., Bailat J., Feitknecht L., Meier J., Shah A., Solar Energy Materials and Solar Cells 81/1 (2004) 61.

[40] Song D., Cho E.-C., Conibeer G., Flynn C., Huang Y., Green M.A., Solar Energy Materials and Solar Cells 92/4 (2008) 474.

[41] Girginoudi D., Tsiarapas C., Georgoulas N, *Properties of a-Si:H films deposited by RF magnetron sputtering at 95 °C,* Applied Surface Science 257, (2011) 3898-3903

[42] Li S.B., Wu Z.M., Li W., Jiang Y.D., Liao N.M., *Influence of substrate temperature on the microstructure and optical properties of hydrogenated silicon thin film prepared with pure silane,* Physica B 403, (2008) 2282-2287

[43] Eygi Z. D., Das U., Hegedus S., Birkmire R., Optimizing Emitter-Buffer Layer Stack Thicknesses for p-type Silicon Heterojunction Solar Cells, J. Renewable Sustainable Energy 5, 013117 (2013)

[44] Es F., Fabrication and Characterization of Single Crystalline Solar Cells, Master Thesis, 2010

[45] Mishima T., Taguchi M., Sakata H., Maruyama E., Development Status of High-efficiency HIT Solar Cells, Solar Energy Materials & Solar Cells 95 (2011) 18-21

[46] Ge J., Ling Z.P., Wong J., Mueller T., Aberle A.G., Optimisation of INtrinsic a-Si:H Passivation Layers in Crystalline-amorphous Silicon Heterojunction Solar Cells, Energy Procedia 15 (2012) 107-117

[47] Dommann, A., Herres, N., Krink, M., Galiano, J. J., Stampfli, B., Internal Stresses and Lifetime Evaluation of PECVD Isolating Layers, Microsystem Technologies, 7, 2001, 161-164

[48] Perrin J., Schmitt J., Hollenstein C., Howling A., Sansonnens L., The Physics of Plasma-enhanced Chemical Vapour Deposition for Large-area Coating: Industrial Application for Flat Panel Displays and Solar Cells, Plasma Phys. Control. Fusion 42 (2000), B353-B363

APPENDIX A

HEAT TRANSFER RELATIONS

A1. Equations Embedded in COMSOL

For the modeling part of this study, COMSOL Heat Transfer with Surface to Surface Radiation Module was used. This module also includes heat transfer in solids (for conductive heat transfer), convective heat flux and surface to surface radiation sub-modules. The equations that COMSOL solves are given below for:

1. Heat transfer with surface to surface radiation;

$$\rho c_p \frac{\partial T}{\partial t} + \rho c_p u . \nabla T = \nabla . (k \nabla T) + Q_r \qquad \text{Eqn (A.1)}$$

2. Heat transfer in solids;

$$\rho c_p \frac{\partial T}{\partial t} = \nabla . (k \nabla T) \qquad \text{Eqn (A.2)}$$

3. Surface to surface radiation;

$$-n . (-k \nabla T) = \varepsilon (G - e_b(T)) \qquad \text{Eqn (A.3)}$$

$$(1 - \varepsilon) G = J - \varepsilon e_b(T) \qquad \text{Eqn (A.4)}$$

$$e_b(T) = n^2 \sigma T^4 \qquad \text{Eqn (A.5)}$$

$$G = G_m(J) + G_{amb} + G_{ext} \qquad \text{Eqn (A.6)}$$

$$G_{amb} = F_{amb} e_b(T_{amb}^4) \qquad \text{Eqn (A.7)}$$

4. Convective heat flux;

$$-n . (-k \nabla T) = h . (T_{ext} - T) \qquad \text{Eqn (A.8)}$$

The related boundary conditions are;

1. Thermal contact between anode and substrate, temperature equality.

$$T_i = T_j \qquad \text{Eqn (A.9)}$$

2. At the outer surface of chamber walls, flux equality.

$$k\nabla T = h.(T_{amb}-T) \qquad \text{Eqn (A.10)}$$

3. At every surface facing vacuum, flux equality.

$$k\nabla T = G(T) - \varepsilon e_b(T) \qquad \text{Eqn (A.11)}$$

The nomenclature for the symbols present in the equations above are tabulated in Table A.1.

Table A.1 Nomenclature of COMSOL Heat Transfer Module

Symbol	Definition	Unit
ρ	Density	kg/m^3
c_p	Heat capacity at constant pressure	j/(kg.K)
u	Velocity field	m/s
k	Thermal conductivity	W/(m.K)
Q_r	Radiative heat transfer term	W
n	Normal vector on the boundary	
ε	Emissivity	
G	Total arriving radiative flux	W/m^2
e_b	Blackbody emissive power	W
J	Total outgoing radiative flux, radiosity	W/m^2
σ	Stefan-Boltzmann constant (5.67 x 10^{-8})	W/m^{2}K^4
G_m(J)	Mutual irradiation arriving from other surfaces in the modeled geometry	W/m^2
G_{amb}	Ambient irradiation	W/m^2
G_{ext}	Irradiation from external sources	W/m^2
F_{amb}	Ambient view factor	
h	Heat transfer coefficient	W/(m^{2}K)
T_{amb}	Assumed far-away temperature in the directions included in F_{amb}	K

A2. The View Factor

The view factor, also called as configuration or shape factor, F_{ij}, is a geometrical quantity corresponding to the fraction of radiation leaving surface i that is intercepted by surface j.

$$F_{ij} = \frac{q_{i \to j}}{A_i J_i} \qquad \text{Eqn (A.9)}$$

The view factor integral provides an expression for F_{ij}, when considering an radiative heat exchange between differential areas dA_i and dA_j as seen in Figure A.1.

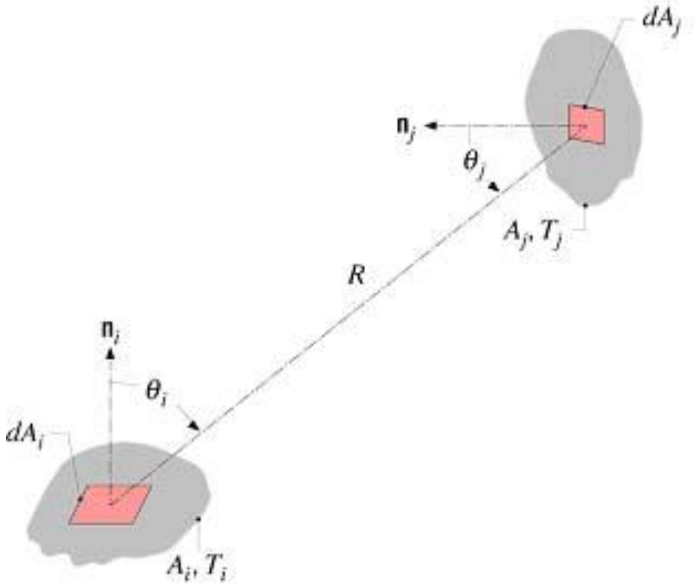

Fig. A.1 Radiative heat exchange between differential areas dA_i and dA_j

$$dq_{i\to j} = I_i cos\theta_i dA_i d\omega_{j-i} = J_i \frac{cos\theta_i cos\theta_j}{\pi R^2} dA_i dA_j \qquad \text{Eqn (A.10)}$$

$$F_{ij} = \frac{1}{A_i}\int_{A_i}\int_{A_j} \frac{cos\theta_i cos\theta_j}{\pi R^2} dA_i dA_j \qquad \text{Eqn (A.11)}$$

There are some common view factor relations, such as;

(i) reciprocity relation

$$A_i F_{ij} = A_j F_{ji} \qquad \text{Eqn (A.12)}$$

(ii) summation rule for enclosures

$$\sum_{j=1}^{N} F_{ij} = 1 \qquad \text{Eqn (A.13)}$$

Since view factors are not constant as emissivity or absorptivity, and calculation is not an easy task, there are several tables and approximations are available in the literature for identical geometries.

CURRICULUM VITAE

ENGİN ÖZKOL

Academic Affiliation:	Department of Chemical Engineering and Center for Solar Energy Research and Applications (GÜNAM), Middle East Technical University
Date/Place of Birth:	08.05.1983 / Aachen-Almanya
Postal Address:	ODTÜ, Fizik Bölümü, B-21, 06800, Ankara-Turkey
Phone:	+90-312-210-5090
E-mail:	ozkol@metu.edu.tr

EDUCATION

University	Subject of Study	Degree	Country	Graduation Year
Middle East Technical University	Chemical Engineering	Ph.D.	Turkey	2015
Middle East Technical University	Chemical Engineering	M.S.	Turkey	2008
Middle East Technical University	Chemical Engineering	B.S.	Turkey	2005

WORK EXPERIENCE

Institution	Title	Dates
METU, Physics Dept, GÜNAM	Project Specialist	2010-...
METU, Physics Dept, Solid State Lab.	Research Assistant	2006-2008
BOYKIMSAN Boya Sanayi ve Ticaret Ltd. Şti.	Intern Engineering Student	07-08/2004
TÜPRAŞ Petrokimya Ltd. A.Ş.	Intern Engineering Student	06-08/2003

AREAS OF EXPERTISE

Nanoscience; Advanced multifunctional materials; Material processing and characterization; Solid state electronic devices; Solar cells; Thin film silicon solar cells; Heterojunction solar cells; Semiconductor engineering;; Plasma science; Vacuum technology;

RESEARCH EXPERIENCE

Experience in thin-film deposition systems:

Physical vapor deposition (PVD), chemical vapor deposition (CVD), plasma-assisted chemical vapor deposition (PECVD), sputtering.

Experience in material characterization techniques:

Scanning electron microscope (SEM), energy-dispersive X-ray spectroscopy (EDX), atomic force microscopy (AFM), optical microscopes, spectroscopic ellipsometry, conductivity measurements, X-ray diffraction spectroscopy (XRD), grazing incidence X-ray diffraction spectroscopy (GIXRD), X-ray photoelectron spectroscopy (XPS), Fourier transform infrared spectroscopy (FTIR), grazing incidence reflection (FTIR-GIR), Raman spectroscopy, secondary ion mass spectroscopy (SIMS), ultraviolet-visible spectroscopy (UV-Vis), profilometry, mass spectroscopy (MS), optical emission spectroscopy (OES), electrical characterization of solar cells.

PUBLICATIONS IN JOURNALS

1. G. Nogay, **E. Ozkol**, S. Ilday, R. Turan. Structural Peculiarities and Aging Effect in Hydrogeneted a-Si Prepared by Inductively Coupled Plasma Chemical Vapor Deposition Technique, Vacuum, Volume 110, December 2014, pages 114-120.
2. Z.M. Saleh, H. Nasser, **E. Özkol**, M. Günöven, B. Altuntas, A. Bek, R. Turan, Enhanced Optical Absorption and Spectral Photocurrent in a-Si:H by Single- and Double-Layer Silver Plasmonic Interfaces, Plasmonics (2014) 9:357–365
3. Z. M. Saleh, G. Nogay, **E. Ozkol**, G. Yilmaz, M. Sagban, M. Gunes, R. Turan, Atmospheric aging and light-induced degradation of amorphous and nanostructured silicon using photoconductivity and electron spin resonance, Canadian Journal of Physics, **92**: 713–717 (2014)
4. H. Nasser, Z. M. Saleh, **E. Özkol**, M. Günoven, A. Bek, R. Turan, Fabrication of Ag Nanoparticles Embedded in Al: ZnO as Potential Light-Trapping Plasmonic Interface for Thin Film Solar Cells, Plasmonics (2013) 8:1485–1492
5. M. Anutgan, T. Aliyeva Anutgan, **E. Ozkol**, İ. Atılgan, B. Katırcıoğlu, Influence of the nitrogen flow rate on the order and structure of PECVD boron nitride thin films, Journal of Non-Crystalline Solids, 355 (2009) 1622–1629
6. Z. M. Saleh, G. Nogay, **E. Özkol**, R. Turan, Atmospheric and light-induced effects in nanostructured silicon deposited by capacitively and inductively-coupled plasma, International Journal of Renewable Energy Research (IJRER), (accepted)

7. H. Nasser, **E. Özkol**, A. Bek, R. Turan, High-haze nature of textured Al:ZnO with Ag nanoparticles for light management in thin film solar cells, Optical Material Express, (accepted)
8. Z. M. Saleh, H. Nasser, **E. Özkol**, M. Günöven, S. Canli, A. Bek, R. Turan, Optimized spacer layer thickness for dramatic enhancement of photocurrent in a-Si:H absorber due to Ag plasmonic interfaces. (Manuscript submitted to Photonics and Nanostructures)
9. M. Karaman, Ö. T. Özmen, S. Habibpur, **E. Özkol**, R. Turan, Poly-Si thin films formed on glass substrate coated by different buffer layer content (Manuscript submitted to Microelectronic Engineering)
10. G. Nogay**,** Z. M. Saleh**, E. Özkol**, R. Turan, Optoelectronic properties of nanostructured Si prepared at low temperature by Inductively Coupled Plasma Chemical Vapor Deposition (ICP-CVD), (Manuscript under preparation).
11. S. Ilday, G. Nogay, **E. Ozkol**, R. Turan. Novel silicon nanostructures from Ballistic deposition: A bottom up approach for nanofabrication. (Manuscript under preparation).
12. H. Nasser, Z. M. Saleh, **E. Ozkol**, A. Bek, R. Turan. Enhanced optical light trapping and spectral photocurrent in a-Si:H by incorporating Ag nanoparticles on the front interface. (Manuscript under preparation)
13. H. Nasser, Z. M. Saleh, **E. Özkol**, A. Bek, R. Turan, Combined Textured ZnO:Al and Silver Nanoparticles for Photon Absorption and Photocurrent Enhancement in a-Si:H Thin Film. (Manuscript under preparation)

REFEERED CONFERENCE PAPERS

1. Hisham Nasser, **Engin Ozkol**, Alpan Bek, Rasit Turan, High Haze Nano-Textured Aluminum doped Zinc Oxide with Plasmonic Silver Nanoparticles for Enhanced Optical Absorption and Photocurrent of a-Si:H thin film. TMS Middle East - Mediterranean Materials Congress on Energy and Infrastructure Systems (MEMA 2015), Doha, Qatar 2015 (best poster award)

2. Hisham Nasser, **Engin Özkol**, Alpan Bek, Rasit Turan, Extreme Spectral Photocurrent Enhancement of a-Si:H Thin Film by Exploiting the Scattering

Potentials of Textured Al:ZnO and Silver Plasmonic Nanoparticles. ***Oral*** presentation, The 29th Şişecam Glass Symposium, Kadir Has University Cibali Campus, Istanbul, November 2014

3. **E. Özkol**, Z. Demircioğlu, S. Kıncal, R. Turan, Effects of Plasma Properties on Defect Density and Doping of a-Si:H in PECVD System. The Turkish-German Conference on Energy Technologies, METU, Ankara, Turkey, 13-15 October, 2014
4. **Engin Özkol**, Gizem Nogay, Zaki M. Saleh, Serkan Kıncal, Raşit Turan, Effects of Process Parameters on Hydrogenated Nanocrystalline Silicon Formation by Inductively Coupled Plasma Chemical Vapor Deposition (ICP-CVD), 29th European PV Solar Energy Conference and Exhibition (EU PVSEC 2014), Amsterdam, Holland, 22-26 Sep 2014.
5. Fırat Es, Emine Hande Çiftpınar, Gülsen Baytemir, **Engin Özkol** ,Olgu Demircioğlu, Mete Günöven, Mustafa Kulakçı, and Raşit Turan, Nano-Hole Texturing of Multi-Crystalline Silicon Solar Cells, 29th European PV Solar Energy Conference and Exhibition (EU PVSEC 2014), Amsterdam, Holland, 22-26 Sep 2014.
6. H. Nasser, **E. Özkol**, A. Bek, R. Turan, Optimized Textured Al:ZnO and Silver Nanoparticles as a Single Front Light Trapping Interface for a-Si:H Solar Cells. The Turkish-German Conference on Energy Technologies, METU, Ankara, Turkey, 13-15 October, 2014
7. Zeynep Demircioğlu, **Engin Ozkol**, Raşit Turan. Optimization of a-Si:H thin film deposited on ITO coated flexible substrate. ***Oral*** Presentation, Nano TR10, Istanbul 2014
8. Mustafa Unal, Hisham Nasser, **Engin Ozkol**, Zeynep Demircioglu, Rasit Turan. Aluminum Induced Nanotexturing of Glass Superstrate for Enhanced Photo-response of a-Si:H Thin Film. ***Oral*** Presentation, Nano TR10, Istanbul 2014
9. **Gizem Nogay**, **Engin Ozkol**, Zaki Saleh, Mehmet Güneş, Rasit Turan, Formation of Nanocrystalline Silicon Thin Film at Low Temperature by Inductively Coupled Plasma (ICP) Assisted CVD Techique and Its Electrical Characterization, ***Oral*** Presentation, The 25th International Conference on

Amorphous and Nano-crystalline Semiconductors, August 18–23, 2013 Toronto, Ontario Canada

10. **Zaki M. Saleh**, Gizem Nogay, **Engin Ozkol**, Gokhan Yilmaz, Mehmet Güneş, Rasit Turan, Atmospheric Aging and Light-induced Degradation of Amorphous and Nanostructured Silicon Using Photoconductivity and Electron Spin Resonance, ***Oral*** Presentation, The 25th International Conference on Amorphous and Nano-crystalline Semiconductors, August 18–23, 2013 Toronto, Ontario Canada
11. **Engin Özkol**, Gizem Nogay, Hisham Nasser, Gökhan Yılmaz, Hamza Cansever, Serkan Kıncal, Mehmet Güneş, Raşit Turan, Effects of Plasma Properties on Doping a-Si in Capacitatively Coupled Plasma System, 28th European PV Solar Energy Conference and Exhibition (EU PVSEC 2013), Paris, France, 30 Sep-04 Oct 2013.
12. Gizem Nogay, **Engin Özkol**, Raşit Turan, Zaki Saleh, Structural and Optical Properties of Silicon Thin Films Deposited by Inductively Coupled Plasma (ICP) Assisted CVD at Room Temperature, 28th European PV Solar Energy Conference and Exhibition (EU PVSEC 2013), Paris, France, 30 Sep-04 Oct 2013.
13. Zaki M. Saleh, Hisham Nasser, Mete Gunoven, **Engin Ozkol**, Burcu Altuntas, Alpan Bek, Rasit Turan. Enhancement of optical absorption in a-SI:H films by silver nanoparticle plasmonic interface. 28th European PV Solar Energy Conference and Exhibition (EU PVSEC) Proceedings (2013) P. 371 - 374
14. H. Nasser, **E. Ozkol**, M. Gunoven, F. Es, R. Turan. Influence of the underlying SiO2 spacer on the properties of silver nanoparticles for potential application in solar cell. 28th European PV Solar Energy Conference and Exhibition (EU PVSEC 2013), Paris, France, 30 Sep-04 Oct 2013 P. 109.
15. **E. Ozkol**, G. Nogay, H. Nasser, G. Yilmaz, H. Cansever, S. Kincal, M. Gunes, R. Turan. Effect of plasma properties on doping a-Si in a capacitively coupled plasma system. 28th European PV Solar Energy Conference and Exhibition (EU PVSEC 2013), Paris, France, 30 Sep-04 Oct 2013 P. 215

16. Z. M. Saleh, H. Nasser, M. Gunoven, **E. Ozkol**, P. Altuntas, A. Bek and R. Turan. Enhacement of optical absorption in a-Si:H films by silver nanoparticle plasmonic interface. 28th European PV Solar Energy Conference and Exhibition (EU PVSEC 2013), Paris, France, 30 Sep-04 Oct 2013 P. 111
17. **Engin Özkol**, Gizem Nogay, Hisham Nasser, Zeynep Demircioğlu, Serkan Kıncal. New Cluster PECVD system at GÜNAM. ***Oral*** Presentation; Solar Electricity Conference and Exhibition (Solar-TR-2), Antalya, Turkey 07-09 November 2012, P. 31
18. **E. Özkol**, G. Nogay, S. Kıncal, R. Turan, 'A Different a-Si Thin Film Sample Preparation Method for ESR Measurements', Solar Electricity Conference and Exhibition (Solar-TR-2), Antalya, Turkey 07-09 November 2012.
19. Z. Demircioğlu, **E. Özkol**, R. Turan, 'Optimisation of Laser Scribing of PET for Thin Film Module Formation', Solar Electricity Conference and Exhibition (Solar-TR-2), Antalya, Turkey 07-09 November 2012.
20. Hisham Nasser, Irem Tanyeli, Firat Es, **Engin Ozkol**, Alpan Bek, Rasit Turan. Plasmonic Light Scattering from Ag Nanoparticles Fabricated on ITO and ZnO Thin Films. Photovoltaic Technical Conference, Aix En Province, France 06-08 June 2012, P. 45